

NATIONAL AERONAUTICS AND SPACE ADMINISTRATION

Space Programs Summary No. 37-35, Volume II

for the period July 1, 1965 to August 31, 1965

The Planetary-Interplanetary Program

(NASA-CR-68959) SPACE PROGRAMS SUMMARY NO.
37-35, VOLUME II FOR THE PERIOD JULY 1, 1965
TO AUGUST 31, 1965. THE
PLANETARY-INTERPLANETARY PROGRAM (Jet
Propulsion Lab.) 62 p

N79-76287

Unclas
11002

FACILITY

(PAGES)

(NASA CR OR TMX OR AD NUMBER)

00/18

(CODE)

(CATEGORY)

JET PROPULSION LABORATORY
CALIFORNIA INSTITUTE OF TECHNOLOGY
PASADENA, CALIFORNIA

September 30, 1965

CLASSIFICATION CHANGE

UNCLASSIFIED

To
By authority of
J. Edgar Hoover
11/26/74
Scientific Document Master Control Section, NASA
Scientific and Technical Information Facility

This document contains information affecting the national
defense of the United States within the meaning of the
Espionage Laws, Title 18, U.S.C. Sec. 793 and 794,
the transmission or revelation of its contents in any manner to
an unauthorized person is prohibited by law.

~~CONFIDENTIAL~~

[REDACTED]

NATIONAL AERONAUTICS AND SPACE ADMINISTRATION

Space Programs Summary No. 37-35, Volume II

for the period July 1, 1965 to August 31, 1965

The Planetary-Interplanetary Program

[REDACTED]

247

Copy No. _____

JET PROPULSION LABORATORY
CALIFORNIA INSTITUTE OF TECHNOLOGY
PASADENA, CALIFORNIA

September 30, 1965

[REDACTED]

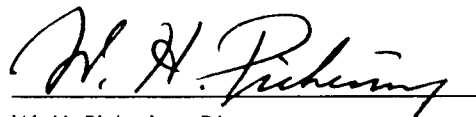
[REDACTED]

Preface

The *Space Programs Summary* is a six-volume, bimonthly publication that documents the current project activities and supporting research and advanced development efforts conducted or managed by JPL for the NASA space exploration programs. The titles of all volumes of the *Space Programs Summary* are:

- Vol. I. The Lunar Program (Confidential)
- Vol. II. The Planetary-Interplanetary Program (Confidential)
- Vol. III. The Deep Space Network (Unclassified)
- Vol. IV. Supporting Research and Advanced Development (Unclassified)
- Vol. V. Supporting Research and Advanced Development (Confidential)
- Vol. VI. Space Exploration Programs and Space Sciences (Unclassified)

The *Space Programs Summary*, Vol. VI consists of an unclassified digest of appropriate material from Vols. I, II, and III; an original presentation of technical supporting activities, including engineering development of environmental-test facilities, and quality assurance and reliability; and a reprint of the space science instrumentation studies of Vols. I and II.



W. H. Pickering, Director
Jet Propulsion Laboratory

Space Programs Summary No. 37-35, Volume II

Copyright © 1965, Jet Propulsion Laboratory, California Institute of Technology

Prepared under Contract No. NAS 7-100, National Aeronautics & Space Administration

This document contains information affecting the national defense of the United States, within the meaning of the Espionage Laws, Title 18, U.S.C., Sections 793 and 794, the transmission or revelation of which in any manner to an unauthorized person is prohibited by law.

Contents

I. <i>Mariner</i> Mars 1964 Project	1
A. Introduction	1
B. Project Engineering	3
C. Systems	8
D. Spacecraft Design	10
E. Guidance and Control	19
F. Telecommunications	28
G. Space Sciences	33
References	44
II. <i>Voyager</i> Project	47
A. Introduction	47
B. Propulsion	48
C. Telecommunications	50
References	60

I. *Mariner* Mars 1964 Project

A. Introduction

The early objective of the NASA/JPL Planetary-Interplanetary Program is the initial probing of the planets Mars and Venus by unmanned spacecraft. The initial probing of Venus was successfully accomplished in 1962 by *Mariner II*. The initial probing of Mars was successfully accomplished by the *Mariner IV* spacecraft during the 1964-1965 flight opportunity.

The primary objective of the *Mariner C* mission (*Mariner Mars 1964* Project) is to conduct close-up flyby scientific observations of the planet Mars during the 1964-1965 flight opportunity and to transmit the results of these observations back to Earth. Planetary observations were performed during the flyby, which provided basic new information about Mars, including television pictures, cosmic dust particle counts, and measurements of magnetic and ionizing radiation fields. In addition, an Earth occultation experiment was carried out during the Type I trajectory flyby to obtain data relating to the scale height and pressure in the atmosphere of Mars.

A secondary objective of the *Mariner C* mission is to provide experience and knowledge about the performance of the basic engineering equipment of an attitude-stabilized flyby spacecraft during a long-duration flight in space farther away from the Sun than the Earth. An

additional secondary objective is to perform certain fields and particle measurements in interplanetary space in addition to those performed in the vicinity of Mars.

The *Atlas/Agena D* launch vehicles used in this project had a capability of injecting a separated spacecraft weight of 570 lb (minimum) into a Mars transfer orbit.

It was planned to conduct two launchings of *Mariner C* missions from two separate launch pads. All activities were planned to exploit the limited launch period to the maximum extent. To accomplish this, the two spacecraft and their launch vehicles were processed in parallel, so that following the launch of the first space vehicle the second vehicle could have been launched without delay, but no earlier than 2 days after the first launch.

The *MC-2* spacecraft was launched on November 5, 1964. The nose cone failed to eject from over the spacecraft, thereby precluding solar panel deployment; and the battery power was depleted 8 hr 43 min after launch.

The *MC-3* spacecraft was successfully launched on November 28, 1964 in a Mars encounter orbit about the Sun. Since launch, the spacecraft and mission have assumed the title *Mariner IV* in accord with NASA policy guidelines governing such flights. The terms *MC-3* and *Mariner IV* may be used interchangeably; *MC-3* is the

actual serial number of the spacecraft, whereas *Mariner IV* is the title assigned to the flying spacecraft and its mission.

The *Mariner IV* flight continues without significant changes in any subsystem performance. The spacecraft is performing as designed and is still being monitored by the worldwide DSIF/SFOF combination on a 24-hr/day, 7-day/wk basis.

The encounter with Mars, which occurred on July 14, 1965 (PDT), was entirely successful. Flight operations were conducted as planned with a series of ground-transmitted commands. Some commands were used to initiate spacecraft actions, with backup being provided by automatic on-board features; other commands were sent to back up the critical automatic operations. Specifically, the encounter sequence was initiated by ground command DC-25 approximately 2 hr earlier than the spacecraft timed CC&S MT-7 in order to allow ample time to accurately pre-position the scan platform. The platform was stopped at an optimum angle for the TV pictures by ground command DC-24, thus pre-empting the automatic platform-positioning functions of the wide-angle and narrow-angle optical acquisition devices. A ground command DC-3 was transmitted to switch the telemetry data mode to an all-science (encounter) mode. This operation would normally have been performed by the wide-angle acquisition system; but because of the pre-positioning, the switch to mode 3 would have occurred too late to be useful. The start of the TV picture recording sequence was initiated by the narrow-angle acquisition system and was backed up by ground command DC-16. The tape recorder was stopped by its own "count to end of tape and stop" logic, and this was backed up by ground command DC-26. The switch to telemetry mode 2 (normal cruise) was initiated by the DAS "count 22 pictures" logic and backed up by ground command DC-2. The spacecraft is mechanized such that DC-26 turns off all science instruments as well as the tape recorder, and DC-2 turns on the cruise science instruments. Therefore, in this sequence the spacecraft is returned to a completely standard cruise mode upon the receipt of the DC-2 command. All remaining functions of TV picture playback were initiated by the CC&S timed commands MT-8 and MT-9.

The TV pictures were played back to Earth twice over a 20-day period without incident. At the end of the second playback, ground commands were sent to once again return the spacecraft to a cruise mode condition. The spacecraft operation has been completely normal during the subsequent cruise period.

Analysis of the TV pictures and the data from the other science experiments is continuing. Preliminary analysis indicates that Mars has a very low (if any) magnetic field; therefore, it has no measurable radiation field (by *Mariner IV* instruments). The TV pictures indicate a Moon-like surface with many craters and no evidence of atmospheric erosion or surface disturbance by volcanic action or crust upheaval. The occultation experiment measurements indicate an atmospheric pressure in the 10-20 millibar region; the lower number, 10 millibars, being the more likely value.

It will be possible to receive telemetry from *Mariner IV* until about October 1, 1965, at which time the spacecraft high-gain antenna pattern main lobe will no longer be pointed back to Earth. This will conclude Phase 1 of the *Mariner Project*. The DSN has determined that if the spacecraft transmitter is returned to the omni or low-gain antenna it will be possible to track the spacecraft as an RF source completely around its orbit of the Sun. This is expected to provide invaluable celestial mechanics data for reducing the present uncertainty in the AU value and the ephemeris of Earth and Mars. This surveillance period has been defined as Phase 2 of the *Mariner Project*. During the latter half of 1967, *Mariner IV* will again be within telemetry reception range of Earth. If the transmitter is then still working and if tracking schedules permit, it may be possible to recover additional cruise science information. This period has been defined as Phase 3 of the *Mariner Project*.

Since the time of encounter, some ground commands have been transmitted to the spacecraft in order to either better understand the TV data or to condition it for the subsequent Phases 2 and 3.

On August 26, a series of commands was sent to condition *Mariner IV* for Phase 2. A DC-13 (midcourse maneuver inhibit) was transmitted to insure against an inadvertent maneuver which could occur if certain specific failures of the CC&S were to occur. Because it is not possible to positively confirm that the DC-13 command was effected, minimum pitch-and-roll turn commands and minimum motor burn commands were also sent to be stored in the CC&S registers. Normally, their post-maneuver state is for maximum turns and burn times.

On August 27, a DC-17 command (Canopus tracker cone angle update) was transmitted to the spacecraft. This was required in order to retain lock on the star Canopus for the remainder of Phase 1.

On August 30, the encounter sequence was rerun by ground command to take pictures of black space in order to provide a further calibration of the TV system. Such a calibration is expected to allow a better understanding of the received Mars pictures and will, therefore, enable a more knowledgeable enhancement of those pictures. This operation required a series of 11 commands.

All of the command operations were without incident and the spacecraft performed perfectly.

The spare spacecraft MC-4 and all its support equipment is still being retained in bonded storage. The PTM has been undergoing continual testing since encounter; however, it too will be committed to bonded storage before October 1, 1965. These spacecraft and supporting equipments are being retained in the event it is decided that MC-4 should be launched at some future time, or in case another project, such as *Voyager*, might require them as useful tools in completing its design or in training procedures.

B. Project Engineering

1. Solar Panel Magnetic Stability Study

a. Introduction. The question of solar panel magnetic field stability arose as a consequence of the relative success in demagnetizing the *Mariner* Mars 1964 solar panels. In order to determine the influence of stray fields upon the solar panels, one demagnetized panel assembly was stored in a controlled magnetic environment. Although interest was centered primarily in the stability of the residual field of the demagnetized panel as an aid in interpreting flight data, information of value to future flight projects was also of concern.

A test program was then developed to answer the following questions: (1) What is the particular vibration axis which results in a minimum solar panel perm? (2) Is there a particular frequency of vibration which results in the perming of a panel in a shaker field? (3) Does the field of a permed panel change with vibration in a shaker field? (4) Does a demagnetized panel, stored for some time in a zero field environment, acquire a remanent field? (5) Does a demagnetized solar panel, oriented parallel to the Earth's field for several weeks, pick up a perm?

(6) Does the field of a permed panel decrease as a function of time in a zero field environment?

b. Instrumentation. In conducting this study, two *Mariner* type-approval solar panels (Substrate Panels 7 and 16) were used. Since Panel 16 had earlier been configured with numerous temperature transducers, it was considered the mechanically weaker panel and so was used solely in the storage tests. Panel 7 was used for the vibration tests during the first month and for storage tests the second month. The specially designed solar panel trailer was used for transporting the solar panels between the various test and storage areas and was utilized for the storage of one panel in the Earth's field for 1 month.

For these tests, it was assumed that the solar panel would be located in the $-Y$ position on the spacecraft, and therefore the solar panel coordinates are based on that position. Although this assumption is arbitrary, it is necessary to define the solar panel axes in terms of the spacecraft coordinates. Both $-X$ and $-Y$ solar panels are slightly closer to the science magnetometer than are the other two panels due to the eccentric location of the low-gain antenna waveguide used to support the magnetometer.

Panels were mapped in the Earth's field at three different positions. To eliminate fields induced by Earth's field, four sets of triaxial readings are obtained by rotating the panel about a horizontal and vertical axis through the magnetometer location. By algebraic combination of these readings, the induced field is eliminated and the field due to residual magnetization of the panel is obtained. Readings were obtained for the relative location of the spacecraft science magnetometer for comparison purposes; however, since demagnetization of the panel reduced the field at this location to < 1 gamma, two other arbitrary locations closer to the panel were also mapped in order to obtain larger field readings. These two positions are in the same $Y-Z$ plane as the magnetometer and 18 in. from the $X-Y$ plane of the solar panel surface rather than the 57.5 in. between the plane of the panels and the magnetometer. One position is 6 in. from the hinge end of the panel toward the center of the panel, the other position is approximately midway between the two ends of the panel.

When using three single-axis flux-gate magnetometers with outputs to three channels of a recorder, adjusted to 1 gamma/mm; accuracy is limited by external disturbances to about ± 1 gamma. The repeatability of readings at high field levels is further limited by the positioning of the solar panel relative to the magnetometer. A 2-in. change normal to the surface of the panel will produce

as much as a 25% change in some readings. Because of this, the two sets of readings obtained for the positions 18 in. from the plane of the panels only indicate trends.

Storage tests of the solar panels were carried out either in a magnetic shield room or in a coil system; both of which had fields less than 100 gamma near the center of the panels. The shield room, with a lower and more stable field over the solar panel, was used whenever available; however, other tests restricted its use for this purpose. Storage of the solar panel in the Earth's field was carried out in a trailer specially designed for transporting the panels.

Magnetization and demagnetization of the solar panels was accomplished in a pair of 7-ft demagnetizing coils separated by 7 ft. The solar panel was supported parallel to the axis of the coils which was oriented in the magnetic east-west direction to minimize Earth's field effects. The solar panels were demagnetized at both a 60-cps AC field and with a 0.05-cps AC field. The 0.05-cps field was also used during those portions of the test where it was desired to magnetize the panel, so that the same general arrangement could be used for both operations. In magnetizing the panel, the 0.05-cps field with constant amplitude was used for 2 to 3 cycles, with the field turned off after one of the half-cycles in the desired direction.

The solar panels were given the vibration testing on a Ling Model 249 vibration exciter or shaker. This shaker had a DC magnetic field in the vicinity of the mounted solar panel that ranged up to 10 gauss for a Y-axis shake (the long axis of the panel) 5 gauss for an X-axis shake (parallel to the panel width), and 1 gauss for the Z-axis shake (normal to the surface of the panel).

In performing these tests, three areas were involved which necessitated transporting the solar panels for some distance in a solar panel trailer. This did have some adverse effect on the measurements. In the case of the panels stored in the low-field environment, they were transported about 3 miles from the point where they were demagnetized to the point of storage. They were mapped at both places for comparison. The vibration exciters were about 0.5 mile from the measurement area.

c. Discussion of results. Several tests were conducted on the solar panel to determine the effects of vibration in an ambient field. In the case of the solar panels with the single magnetic field constituent being in the form of wires and strips which were all aligned in the long axis of the panel, it was expected that this would be the direction

of maximum field. This was borne out by the first vibration tests in which the panel was shaken in each of its coordinate axes individually and mapped. The Y-axis shake, with the panel in the larger ambient field due to the shaker and the field generally parallel to the long dimension of the panel, produced a considerably higher magnetization in the panel. This magnetization appeared to be what one would expect for the average value of ambient field of the shaker.

The panel was then shaken only in the Y-axis direction individually over successively increasing frequency bands of approximately an octave each from 40 to 2000 cps. The difference in magnetization acquired over each octave was very slight with the magnetization being approximately 10% less below 160 cps. When a panel is magnetized, shaken, and then mapped, there appears to be no simple relation between the resultant magnetization and either the magnetizing field level or the magnetization acquired by a demagnetized panel when shaken. The magnetization is considerably altered by the subsequent vibration, but it would be virtually impossible to predict the resultant magnetization. One problem here is that the magnetizing field is considerably more uniform than the field of the vibration exciter so that the field of the vibration exciter, during the shake, does not affect the panel at the outer end of the panel. In the course of these tests, it was also found that the shaker field was not always of the same magnitude at the same point. Because of this and the fact that three-axis vibration tests are not always performed in the same sequence of vibration in the three axes, it is virtually impossible to predict the resultant magnetization following a three-axis shake. So long as magnetic material is to be employed in spacecraft, there is a need for additional study on the effect of vibration in a controllable and uniform ambient field. These results are summarized in Table 1.

Table 1. Magnetic field measurements at flight magnetometer position for a solar panel in the — Y (Bay 7) location

Condition of panel	Field, gamma (10^{-3} Oe)		
	H_x	H_y	H_z
Demagnetized	<1	<1	<1
1 Gauss magnetizing field (approx)	<1	<1	6
5 Gauss magnetizing field	7	0	55
20 Gauss magnetizing field	25	7	165
X-Axis vibration (Ling 249 shaker)	0	1	3
Y-Axis vibration	7	17	53
Z-Axis vibration	0	0	2
Typical panel after FA vibration	2-8	1-3	20-26

The storage tests were somewhat inconclusive because of the fact that the panels stored in the near-zero field environment were of necessity stored alternately in a shielded room and in a coil system. Also, the equipment used to map the panels near the storage area suffered from instability. In spite of this, the demagnetized panel stored for 3 weeks in a low ambient field experienced only a very slight change in field, and this change was only discernible at the position 18 in. from the surface of the panel. This panel was stored in the shield room for 6 days followed by 14 days in a four-coil spherical coil system oriented in the direction of Earth's total field.

When the panel was magnetized by exposure to a 5-gauss field and stored, the residual magnetization showed a definite decrease over the first week of the storage period. This panel was stored 13 days in the shield room followed by 11 days in the coil system. The change in field was approximately a 25% decrease the first week with a negligible change following that.

d. Conclusions. This study has provided an insight into the magnetic behavior of Kovar on solar panels. It appears that the demagnetization of these panels was successful primarily due to the fact that the Kovar was in the shape of long strips and wires and these elements were all aligned in the same direction. Because of this, it was possible to demagnetize the panels by a single demagnetizing field in the direction of this long dimension, and the effects of the Earth's field could be virtually eliminated by orienting this demagnetizing field at right angles to the Earth's magnetic field.

In this study, both 60-cps and 0.05-cps demagnetization was used. The 60-cps demagnetization proved to be slightly better here. It is believed this was due to the manner of generating the 0.05 cps field by means of a programmed DC power supply and a polarity reversing switch. With a power supply capable of 100-amp current, it is difficult to adjust it so that it approaches zero properly with the programming control. As a result, it is believed that the minimum attainable field was too high.

The solar panels are more magnetic than the remainder of the spacecraft, but because of their configuration and the fact that the material is relatively soft, they can be more easily demagnetized. Before it can definitely be stated that solar panels with Kovar bus bars can be accepted with an assurance of stability, some investigation of its stability as a function of shock in low field environments would be needed. In the absence of information on the relationship between magnetization and shock or vi-

bration the only certain way to insure magnetic stability is by continued restriction of the use of magnetic materials in spacecraft where magnetic field control is a requirement.

2. Mariner PTM Demagnetization Study

a. Introduction. In order to achieve a satisfactory spacecraft magnetic environment for the magnetometer, stability of the spacecraft field is required. An effort was made in the development of the *Mariner* systems to minimize the use of magnetic materials. Efforts to shield magnetic components were also made. However, due to time and technology limitations, the spacecraft when assembled still had a large field at the magnetometer. The bus was observed to have a field of +30 gamma in the Z-axis direction of the spacecraft at the magnetometer. The solar panels were observed to contribute a field of approximately -95 gamma. The net field was observed to be about -70 gamma at the magnetometer in the Z-axis direction. In order to reduce the size of this field, a demagnetizing fixture consisting of two 7-ft parallel coils with a 7-ft separation, capable of a 100-gauss field was designed and built. The launch schedule did not permit development of a bus demagnetization program. The solar panels, however, were successfully demagnetized, reducing their field to less than -2 gamma at the magnetometer. In this manner the net field of the flight spacecraft was reduced to approximately 30 gamma at the magnetometer, resulting in an acceptable magnetometer environment.

b. Purpose. In order to further determine the magnetic properties of a whole spacecraft, two series of tests were conducted on the *Mariner* Proof Test Model (PTM). The purpose of these studies was to determine (1) the feasibility of bus demagnetization, (2) the optimum procedure and equipment for demagnetization, (3) the desirability of standardized magnetization and demagnetization procedures for magnetic qualification tests on future spacecraft, and (4) the stability of the spacecraft field in various magnetized and demagnetized states.

c. Test procedure. The first series of tests, which was performed on the PTM from 18 May to 24 May, consisted of demagnetization in the Earth's field at successively higher starting field strengths in alternating pairs of Z and X-Y axis orientations and mapping the PTM field at the magnetometer position following each demagnetization. The demagnetization coils and the mapping technique used for the previous solar panel tests were used in these tests. For magnetization and demagnetization in

the X-Y plane of the PTM, both 7-ft coils were used with a separation of 7 ft, and the PTM was suspended between them by an overhead crane. For demagnetization in the Z-axis, one 7-ft coil in a horizontal position was used. A 0.05-cps rectangular pulsed AC power supply with pulses of 3-sec duration was used to excite the coils. The inductance of the coils eliminated excessively rapid and thus damaging fluctuations in the demagnetizing field. The starting amplitude of the demagnetizing field on the final X-Y and Z-axis demagnetization was 80 gauss, and the exponential decay times of the amplitude were 24 and 18 min, respectively. As shown in Table 2, the minimum permanent field of the PTM was obtained by the 80-gauss X-Y demagnetizing resulting in a +17 gamma Z-field, a +0.5 gamma Y-field, and a -0.5 gamma X-field. The field at the magnetometer position was measured with the PTM in four orientations created by 180-deg rotations about the vertical and horizontal axes at the magnetometer position. This allowed the net permanent PTM field to be determined by taking the difference of the actual field measured in opposite directions on the X, Y, and Z axes. In this way, the effects of fields induced in the PTM by the Earth's field were eliminated. Between each measurement, the PTM was withdrawn to effective infinity for calibration purposes, and two series of four measurements were made for each mapping, giving an accuracy of about 1 gamma. The magnetic tests were then interrupted by other uses of the PTM. Systems checkout test revealed no degradation of the PTM components due to the demagnetization fields. The use of a low-frequency field which allows large field strengths without inducing more than the specified limit of 100 mv in any circuits was thus found satisfactory. A Fourier analysis of the field wave form showed that only the first and third harmonics had significant amplitudes.

Table 2. First demagnetization test series results

Max field strength, gauss	Orientation	Measured field, gamma		
		H_x	H_y	H_z
None	None	+4	+4	+31
5	X-Y-plane	+3	+2	+28
5	Z-axis	-1	+2	+30
10	Z-axis	+2	+2	+29
10	X-Y-plane	-2	-3	+23
20	X-Y-plane	-2	0	+23
25	Z-axis	-1	-1	+21
40	Z-axis	-1	-1	+20
40	X-Y-plane	-5	0	+19
80	X-Y-plane	-1	+1	+17
80	Z-axis	-5	-1	+17

A second series of tests was carried out on the PTM from 3 August to 6 August. Because of the previous inability to demagnetize the bus to a field of less than 17 gamma at the magnetometer, it was decided to attempt to lower the ambient field during demagnetization by using two pairs of large coils to buck out the Earth's field. These bucking coils made use of two pairs of wooden ring forms from a 10-ft three-axis Helmholtz coil set. One pair was lengthened 21 in. to allow enough room for the demagnetizing coils, and both pairs were wound with 50 turns of wire on each coil. The spacing of coils was 5 feet for both pairs, which was the proper Helmholtz spacing. As was expected, the field produced by these coils was not uniform, but an order-of-magnitude improvement within the spacecraft area over the Earth's field was obtained. For the two demagnetizing coil configuration, used for X-Y plane demagnetization of the PTM, both bucking coils were used with the axis of the lengthened pair aligned with the Earth's vertical magnetic component and with the axis of the other pair aligned with the Earth's horizontal component (Fig. 1). This configuration produced a field ranging from -3600 gamma to +3000 gamma within the PTM hexagonal bus area. For the single demagnetization coil configuration, used for Z-axis demagnetization of the PTM, only the lengthened pair of bucking coils was used, and its axis was aligned with that of the Earth's total field (Fig. 2). This configuration was very satisfactory and reduced the field in the area of

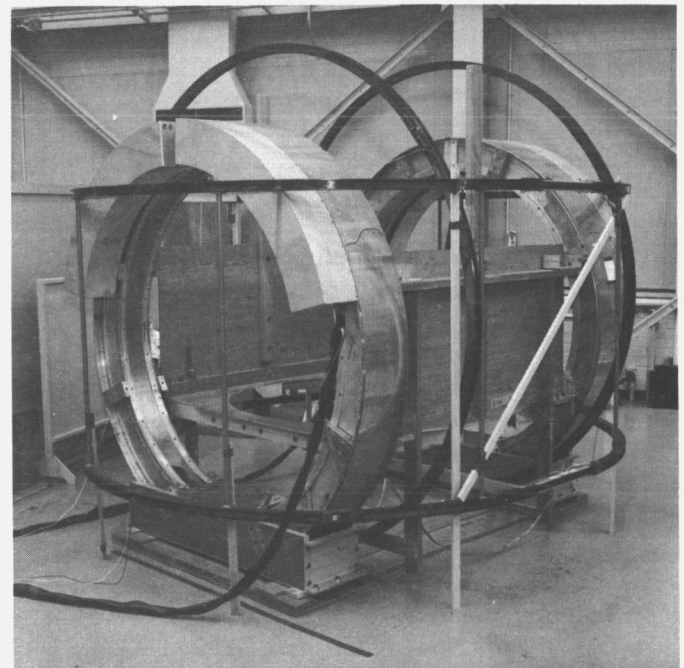


Fig. 1. X-Y plane demagnetization configuration

interest to a range of from -1600 to $+2000$ gamma. An extensive series of both magnetization and demagnetization tests with various PTM orientations was made. Three to five half-cycles of the pulsed power supply were used to drive the main coils for magnetization tests and a decay period of about ten minutes was used for the demagnetization tests.

The field observed after these tests is listed in Table 3.

d. Conclusions. These tests showed that the magnetic field of the PTM could be significantly decreased even in an Earth's ambient field. The lowering of the ambient field during demagnetization allowed the PTM residual field to be lowered significantly further to a value of $+4.3$ gamma in the Z-axis direction, -4 gamma in the X-axis, and 0 gamma in the Y-axis. The magnetization tests showed that the spacecraft was more than twice as susceptible to magnetization in the Z-axis than in the X-Y plane. Magnetization along one axis and demagnetization along another showed that maximum spacecraft demagnetization requires demagnetization along three perpendicular axes in a low ambient field. The negligible change in the PTM field during the 2 months of systems tests and encounter operations showed that this magnetic state of the PTM was relatively stable. Vibration testing had been considered, but the strong magnetic fields of the shakers give this type of test little significance. The maximum possible change in the spacecraft field is shown by the difference in the fields retained after magnetization and demagnetization. This type of test will probably be required of future spacecraft to determine their magnetic properties. Since previous studies of solar panels indicated that the demagnetized state is the most stable, the process of demagnetization for a whole spacecraft worked out during these tests could also be applied to future spacecraft.

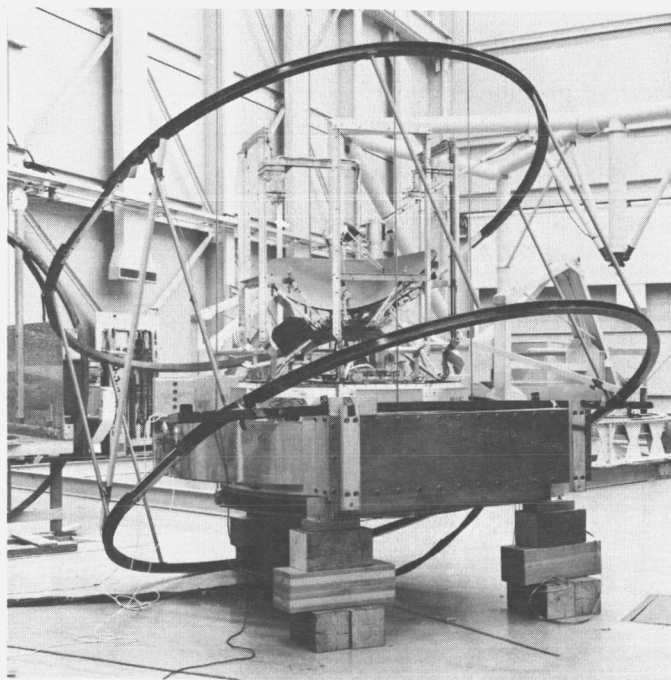


Fig. 2. Z-axis demagnetization configuration

Table 3. Second demagnetization test series results

Max field strength, gauss	Orientation	Mode	Measured field, gamma			Notes ^a
			H_x	H_y	H_z	
None	None	None	-5	-1	$+17$	Two demagnetization with change of 90°
40	X-Y plane	Demagnetization	-6	$+1$	$+8$	
40	Z-axis	Demagnetization	-6	0	$+4$	
25	Z-axis	Magnetization	$+2$	$+27$	$+132$	
40	Z-axis	Demagnetization	-5	0	$+4$	
50	Z-axis	Magnetization	-10	-52	-205	90° to previous demagnetization
80	Z-axis	Demagnetization	-6	0	$+3$	
40	Z-axis	Demagnetization	-6	0	$+4$	
25	X-Y plane	Magnetization	$+43$	-40	$+21$	90° to previous demagnetization
40	X-Y plane	Demagnetization	-6	$+1$	$+3$	
25	X-Y plane	Magnetization	-41	-32	$+12$	
40	X-Y plane	Demagnetization	-6	0	$+4$	90° to previous Magnetization
50	X-Y plane	Magnetization	$+72$	-68	$+29$	
80	X-Y plane	Demagnetization	$+7$	-11	$+10$	
40	X-Y plane	Demagnetization	-4	0	$+4$	90° to previous demagnetization

^aall rotations are about Z-axis

C. Systems

1. Mariner Mars 1964 Space Flight Operations

Mariner Mars 1964 Space Flight Operations (SFO) activities, covering the reporting period July and August 1965, have been directed toward the coordination and participation in encounter tests, encounter, and post-

encounter operations for *Mariner IV* (MC-3), and the generation of documents.

a. SFO encounter tests. A final series of two (2) encounter tests were conducted using the *Mariner* Proof Test Model (PTM), simulated data and the flight spacecraft as the data source. These tests exercised the SFO

Table 4. Encounter events that occurred on July 14 and 15

Command	Event	Transmit, GMT	Spacecraft received, GMT	Verified-in data, GMT
DC-25	Encounter science on; starts platform scan	14:27:55	14:40:32	14:52:31
MT-7	CC&S nominal command to start encounter sequence, now backup to DC-25	—	15:41:49	15:53:49
DC-24	Stop scan platform	17:10:18	17:22:55	17:34:55
DC-3	Transfer to telemetry data Mode 3, all science data	22:10:29	22:23:07	22:35:08
WAA	Wide-angle acquisition scan platform's wide-angle Mars sensor acquires planet, automatic backup to DC-3	—	23:42:41	23:54:42
DC-16	Backup to NAA	00:11:57	00:24:36	00:36:37
NAA	Narrow-angle acquisition scan platform's narrow-angle Mars sensor acquires planet; starts video storage subsystem (VSS or tape recorder)	—	—	00:29:59
DC-26	Backup to automatic S/C tape recorder turnoff	00:31:42	00:44:21	00:56:22
DC-2	Turn on cruise science and telemetry data Mode 2; $\frac{1}{3}$ engineering, $\frac{2}{3}$ science data; series of six commands	00:32:40 00:37:00 00:42:00 00:47:00 00:52:00 00:57:00	00:45:19 00:49:39 00:54:39 00:59:39 01:04:39 01:09:39	00:57:20 01:01:40 01:06:40 01:11:40 01:16:40 01:21:40
—	S/C closest approach to Mars	—	01:00:58	—
—	S/C enters occultation; goes behind Mars and S/C radio (RF) transmission signal to Earth blanked out by planet	—	02:19:11	02:31:12
—	S/C exits occultation and RF signal received on Earth	—	03:13:04	03:25:06
MT-8	CC&S command to turn off encounter science; automatic backup to DC-26	—	05:01:49	05:13:52
MT-9	Cruise science off and switch to data Mode 4/1, VSS recorded data; engineering data; initially Mode 1 only	—	11:41:49	11:53:53
—	S/C VSS start transmission TV picture 1, telemetry data Mode 4	—	12:49:54	13:01:58

System operational and technical personnel in the system and procedures to be used during the Encounter Phase of the mission. These tests were entitled Encounter-Operational Readiness No. 2 and Encounter-Operational Readiness No. 3.

b. Flight operations for Mariner IV (MC-3). During the two most crucial months of the mission (July and August 1965), spacecraft performance was excellent, with the following major events occurring:

Cruise Events; Pre-Encounter.

- (1) Central Computer and Sequencer (CC&S) cyclic Nos. 78 through 82 were observed on schedule, one every 66 $\frac{2}{3}$ hr.
- (2) Disturbances in the roll channel of the attitude control subsystem were observed on July 3, 5, 6 and 12.

Planetary Encounter. Events that occurred on July 14 and 15 are listed in Table 4.

Post-Encounter Events.

- (1) First playback of TV picture No. 1 through the 22nd line of picture No. 22 began on July 15 at 13:01:58 GMT (Mode 4 in data) and ended on July 24 at 19:26:33 GMT (end of Mode 4 in data). The playback sequence included 8 hr, 35 min of TV Science data (Mode 4) and 1 hr, 57 min of engineering data (Mode 1) for each complete picture.
- (2) Second playback of TV picture No. 1 through the 22nd line of picture No. 22 began on July 24 at 21:21:53 GMT (Mode 4 in data) and ended on August 3 at 03:35:40 GMT (end of Mode 4 in data).
- (3) Return of the spacecraft to cruise mode on August 3, 1965 was effected by the sequence of events listed in Table 5.

Table 5. Commands that effected the return of the spacecraft to cruise mode on August 3

Command	Event	Transmit, GMT	Verified-in data, GMT
DC-28	Turn on battery charger	03:08:33	03:36:03
DC-26	Turn off planet science, cruise science, and battery charger	03:14:33	03:42:09
DC-2	Switch to telemetry Mode 2 and turn on cruise science	03:20:33	03:48:03

Cruise Events; Post-Encounter.

- (1) Disturbances in the roll channel of the Attitude Control Subsystem were observed on August 5.
- (2) CC&S cyclic Nos. 90 through 100 were observed on schedule, one every 66 $\frac{2}{3}$ hours.
- (3) The plus-Y solar vane moved in the adaptive mode with a one-DN change.
- (4) A *Mariner IV* Mars TV calibration encounter sequence (second record) was attempted on August 21, 1965, GMT.

The primary objective of the TV calibration sequence was an in-flight calibration (black space) on the performance of the TV/Recording Subsystems in order to maximize the usefulness of the TV data obtained during planetary encounter. Especially valuable was to be the information acquired during the gain-stepping sequence of the TV Subsystem. It was planned to perform an encounter via ground command with the scan platform oriented toward the black space. The four or five pictures representing the different TV gain settings were to be played back in order to provide a map of the vidicon target surface for a black background at the various gains.

A secondary objective was to take TV pictures of *Altair*, a first-magnitude star in the constellation Aquila, which was within the *Mariner IV* Television Subsystem cone angle of view on August 21, 1965, GMT.

This sequence was canceled because of technical difficulties with the command transmitter. Commands that were sent to the spacecraft on August 21 are listed in Table 6.

c. SFO documents. Mariner IV Progress Reports. The purpose of the *Mariner IV* Progress Report is to present information on the performance of the *Mariner IV* (MC-3) spacecraft and to report, in general terms, the performance of the SFO System. Progress Report No. 4 covered the period of May 1, 1965 to May 31, 1965 (Launch + 155 days to Launch + 185 days) and was published on July 5, 1965.

Mariner Mars 1964 Technical Bulletins. The *Mariner Mars* 1964 Technical Bulletins are issued daily and report the daily status of the *Mariner Mars* 1964 Mission. Technical Bulletins 215 through 276 were issued during July and August 1965.

Table 6. TV calibration commands that were sent to the spacecraft on August 21

Command	Transmit, GMT	Spacecraft received, GMT	Verified-in data, GMT
DC-25	22:22:00	22:37:21	22:52:04
DC-28	23:20:00	23:35:21	23:50:05
DC-28	23:22:00	23:37:21	23:52:05
DC-26	23:28:13	23:43:34	23:58:05
DC-26	23:30:13	23:45:34	00:00:05
DC-2	23:32:13	23:47:34	00:02:05
DC-2	23:34:13	23:49:34	00:04:05
DC-2	23:39:00	23:54:21	00:09:05
DC-2	23:44:00	23:59:21	00:14:05
DC-2	23:49:00	00:04:21	00:19:05
DC-2	23:54:00	00:09:21	00:24:05
DC-2	23:59:00	00:14:21	00:29:05

Space Flight Operations Plan (EPD-122, Addendum I). This addendum describes the plan for the Encounter and Post-Encounter period of the *Mariner Mars 1964 Mission*. This addendum was published on July 5, 1965.

Mission Events Flow Diagram. The purpose of this diagram is to display all events, in flow diagram form, that occur during the mission. Daily updating of this diagram continues.

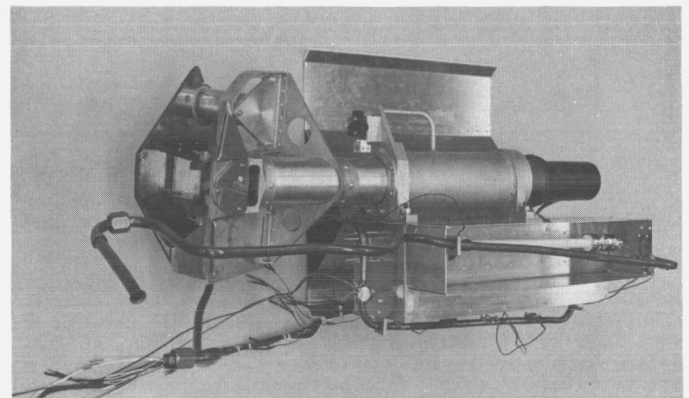
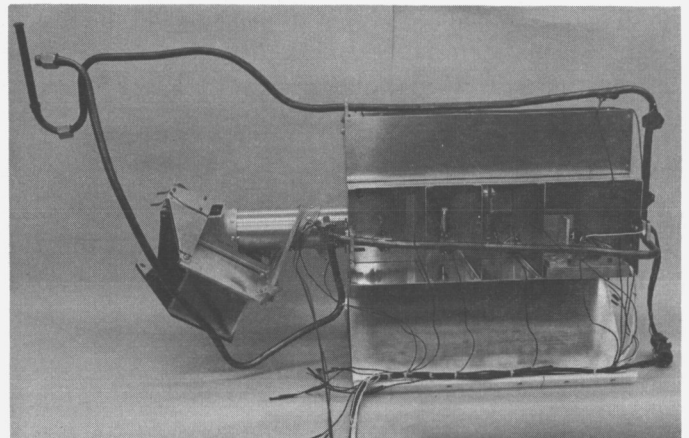


Fig. 3. Mechanical components life test, side and top views

D. Spacecraft Design

1. Introduction

Mariner IV flight data indicated that the structure, electronic cabling, mechanical devices, and the electronic packaging performed as designed. Flight telemetry was obtained which verified the proper operation of various mechanical devices. Life tests were completed on a number of mechanical components (Fig. 3); no significant degradation was observed.

Monitored temperatures remained within allowable limits throughout flight (Table 7). These temperatures were generally lower than prelaunch predictions, but other flight thermal performance was essentially as expected. The absorptivity standard (Fig. 4) provided good information regarding the degradation of thermal control surfaces in space, and a better appreciation of the limitations of space simulator testing was obtained.

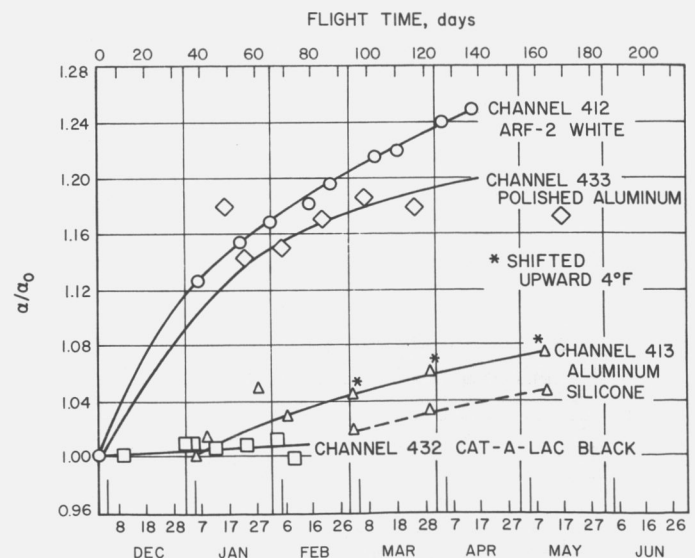


Fig. 4. Mariner IV absorptivity standard ratio versus time

Table 7. Mariner IV flight temperature evaluation

Channel	Temperature measurement	Earth cruise		Mars cruise		12-5-65 Midcourse maximum, °F	8-2-65 Playback ^a minimum, °F	Operating temperature limits, °F
		11-30-64 °F	Predicted °F	7-13-65 °F	Predicted °F			
401	Bay 1	76	89	60	62	88	54	14 to 167
421	Bay 2	71	85	41	46	94	33	35 to 125
402	Bay 3	70	74	51	55	73	34	14 to 122
423	Bay 4	72	80	54	57	75	47	14 to 167
404	Bay 5	66	69	60	60	73	59	14 to 149
424	Crystal oscillator	72	77	69	69	74	68	14 to 167
405	Bay 6	71	75	70	73	73	69	14 to 167
426	Bay 7	63	68	58	57	70	57	30 to 131
407	Power regulator	95	106	83	87	114	77	14 to 167
408	Midcourse N ₂	70	83	47	51	136	38	35 to 125
428	Battery	75	85	60	64	81	57	40 to 140
409	SP 4A1	136	150	9	20	135	8	10 to 175
429	SP 4A5	136	150	11	20	134	9	10 to 175
410	Canopus sensor	60	62	52	51	68	49	0 to 100
430	Lower ring	63	69	55	56	72	53	-300 to 300
411	Scan actuator	71	82	50	53	77	44	-30 to 200
431	Upper ring	87	104	46	52	109	37	-300 to 300
434	Upper shield	223	268	82	110	221	80	-200 to 300
435	Lower shield	-126	-95	-131	-105	-126	-131	-200 to 300
436	Tape recorder	68	71	58	60	70	58	14 to 149
437	Spits	37	46	14	26	39	9	-20 to 122
418	TV	38	46	13	26	39	9	-4 to 104
438	TRD	81	97	49	55	84	39	14 to 122
419	Ion chamber	70	100	-19	10	95	-28 ^b	-22 to 158
439	Magnetometer	34	54	-35	-19	102	-68	-40 to 131
217	Midcourse fuel	72	80	49	52	84	39	35 to 125
218	A/C X/-Y N ₂	70	78	54	54	77	50	40 to 140
219	A/C -X/Y N ₂	71	76	51	53	76	45	40 to 140

^aCruise science off. ^bEstimated.

2. Spacecraft Structure and Mechanisms

a. Flight results. Because the function of all the structural and many of the mechanical items is passive after launch, little telemetry is transmitted about the performance of these items. As a result, the in-flight performance of these components can only be deduced from other flight information. This is also true in the case of the electronic packaging design and the electronic cable harnessing. All information gained during the flight indicates that the structure, electronic cabling, mechanical devices, and the electronic packaging design performed as designed. Telemetry was recovered in flight on the performance of the following mechanical devices:

Separation Initiated Timer and Pyrotechnic Arming Switch. Telemetry event indications verified that either

the pyrotechnics arming switch (PAS) or the separation-initiated timer (SIT) energized the pyrotechnics control assembly (PCA). The PAS closure arming the PCA was designed to occur at spacecraft/*Agena* separation; the SIT switch closure was a backup designed to occur about 40 sec after separation. It was not determined whether the PAS or the SIT energized the PCA, because telemetry data covering spacecraft separation were not available during that time.

The first available data encoder event counter indications were received about 3 min after separation. The telemetry indicated a normal SIT-actuated solar panel deployment and unlatch of the planetary scan platform.

Solar Panel Deployment. Telemetry indications from the solar panel deploy switches through the data encoder

event counters indicated that each of the four panels had released by the pyrotechnic pin-pullers and had been deployed by the panel deployment springs to within 20 deg of the full-open position. Temperature and power measurements later confirmed panel deployment.

Cruise Damper and Latch. Based on the successful midcourse maneuver, it is deduced that the panels did deploy and latch in the fully-open position and that any panel excursions during the motor firing were adequately damped. Had the dampers and latches failed to perform as designed, the center-of-gravity shifts caused by misaligned or excessively vibrating panels would have degraded the accuracy of the maneuver.

Scan Actuator. The scan actuator was operated during the science cover drop exercise for approximately 11 scan cycles. During the scanning period of 127 min, in which the actuator functioned normally, the average scan cycle was 11 min 52.9 sec.

At Mars encounter, the actuator again operated within the design limits. During the 108 min of operation, the average scan cycle time was 11 min 53.2 sec. An analysis of the scan reversal points verified that the actuator reversed at the first set of limit switches.

The scan actuator was pressurized to 30 psia when it was assembled. At launch the pressure was 29.5 psia. During the science cover drop and at encounter, the pressure was 28.8 psi and 26.6 psi respectively. This decrease in pressure is attributed to seal leakage and porosity in the magnesium actuator cover.

Scan Inhibit Switch. The data encoder event register indicated that the scan inhibit switch functioned as designed when the pin-puller latching the science platform was fired at spacecraft injection. The subsequent successful operation of the scan actuator verified this conclusion.

Science Platform Cover. On the 75th day of the flight, the single-shot science cover solenoid, initiated from the PCA, successfully unlatched the science cover. The proper deployment of the cover was verified by a change in the DN of the spacecraft identity channel (414) and by a decrease in the platform temperature.

b. Mechanical devices life test. To ascertain the long-term effects of the space environment on the science scan system mechanical components and oil-filled devices, a life test was performed on the (1) science scan actuator, (2) science cover actuator, (3) separation initiated timer, and (4) solar panel boost and cruise dampers. The com-

ponents were placed in the 30- × 50-in. horizontal vacuum chamber in such a way that they were completely baffled from the other components to minimize the cross-contamination of one unit by another. Fig. 3 shows the setup used, with the scan system on one side and the individual compartments for the components on the other side. Condensing mirrors were placed at the entrance of each compartment to trap any outgassing products. The condensing mirrors were held at -50°F , and the vacuum chamber walls were maintained at 130°F . The pressure was 10^{-4} torr or lower for the duration of the test. In addition to the condensing mirrors, the weights of the components both before and after the life test were recorded as an additional measure of oil leakage.

The science scan actuator was operated for 14 hr each day for the first 50 days, and the science cover actuator solenoid once each day during the same period. The separation timer and the dampers soaked in the thermal-vacuum environment during the test time (6 months) to determine the amount of oil leakage and the possible effect on spacecraft performance. The scan actuator was restarted in the final week and operated for 14 hr/day.

Several problems were uncovered during the test, but in every case they were traced to a problem in the support equipment and not to the spacecraft hardware itself. One problem was that the liquid nitrogen line to the chamber cold trap was inadvertently interrupted allowing previously outgassed products to migrate into the chamber and condense on the mirrors. This heavy coating of oil on the mirrors prevented the optical detection of silicone oils as used in the spacecraft hardware. Chemical analysis of the oil coating, however, showed no traces of silicone base oils. The weights of the test items after the test indicated that a very small amount of something had outgassed but the amount was so small that effects on the spacecraft would be unnoticed.

The scan actuator was operated a total of 1220 hr, and the science cover actuator a total of 90 times. This length of operation had no detrimental effects on these units. The dampers and separation initiated timers also functional as designed after the test.

3. Temperature Control

a. Flight results summary. Table 7 lists flight temperatures for thermally critical event times and compares these data with pre-launch predictions and prescribed limits. Monitored temperatures remained within allowable limits throughout flight. Flight temperatures were

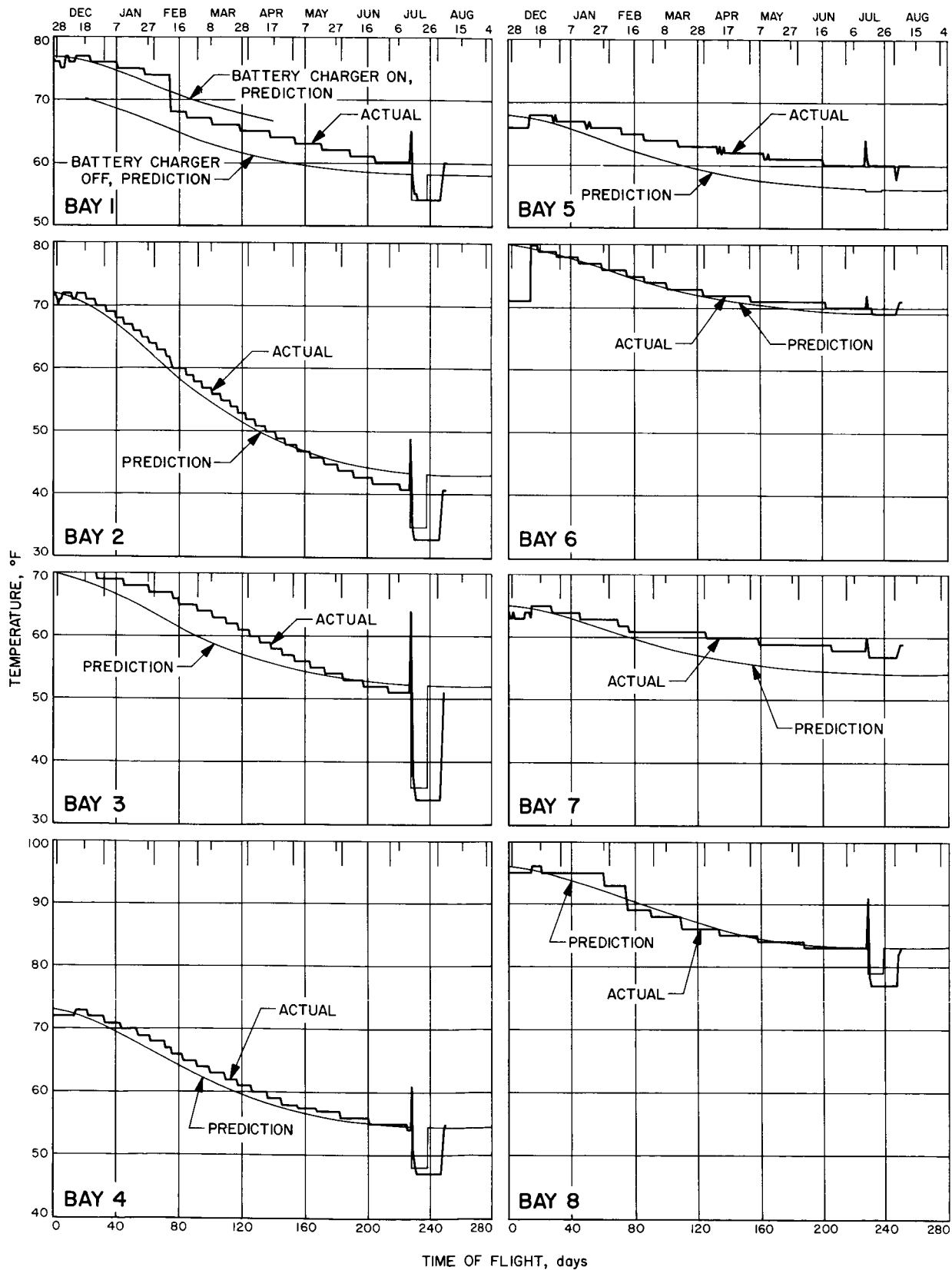


Fig. 5. Mariner IV flight temperatures of Bays 1 through 8

generally lower than pre-launch predictions because simulator tests were conducted at higher solar intensities than those seen in flight.

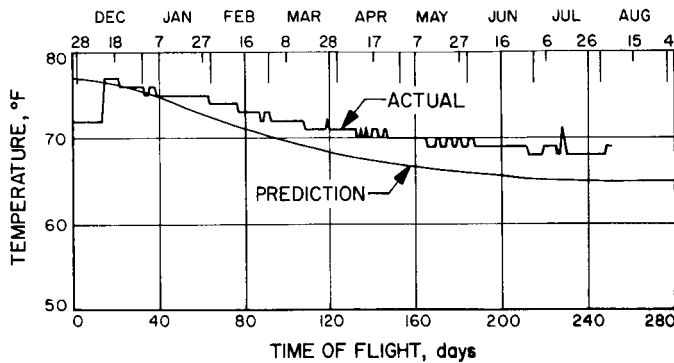


Fig. 6. Mariner IV crystal oscillator flight temperatures

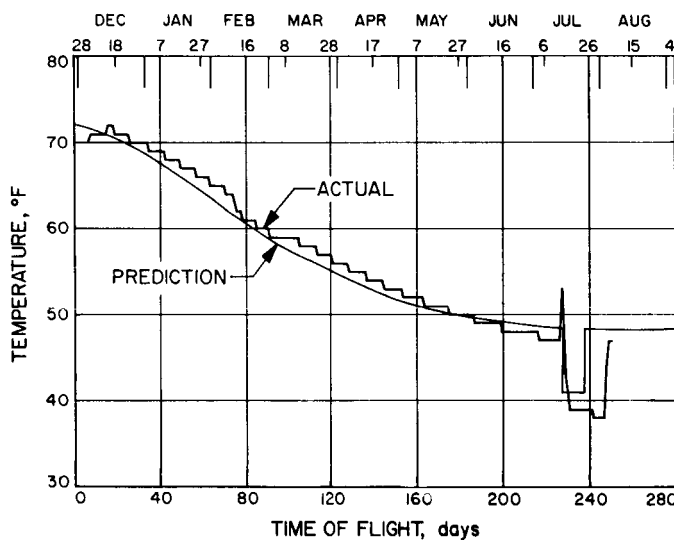


Fig. 7. Mariner IV midcourse nitrogen flight temperatures

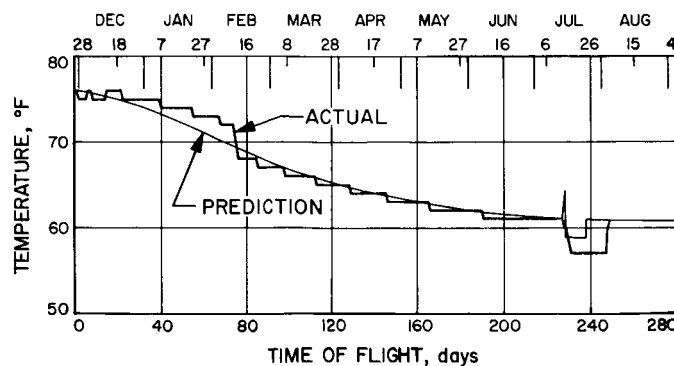


Fig. 8. Mariner IV battery temperature prediction

Figs. 5 through 22 show flight temperature-time histories. Also plotted for comparison are predicted performance curves based on initial flight temperatures and space simulator test results. Agreement is seen to be generally good.

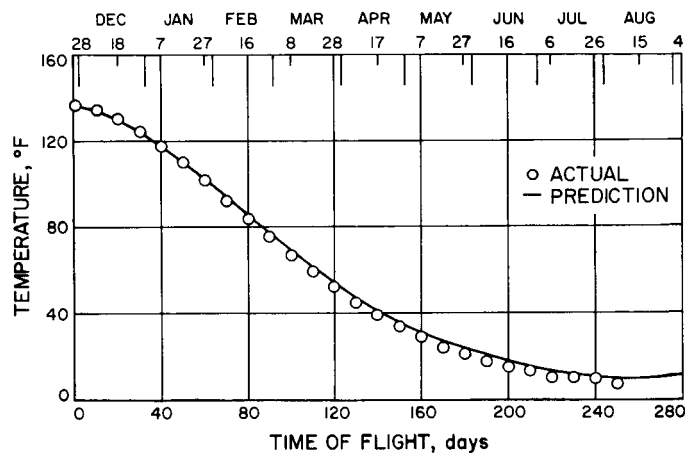


Fig. 9. Mariner IV solar panel flight temperatures

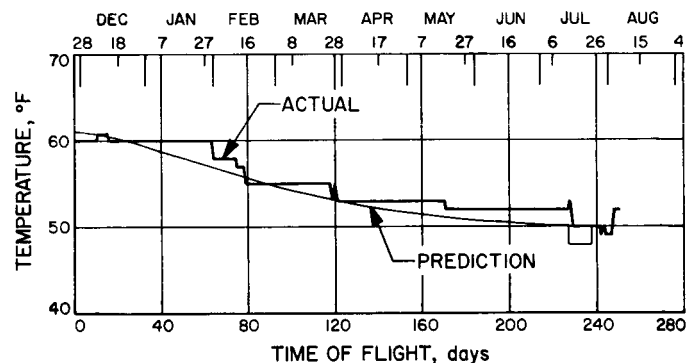


Fig. 10. Mariner IV Canopus sensor flight temperatures

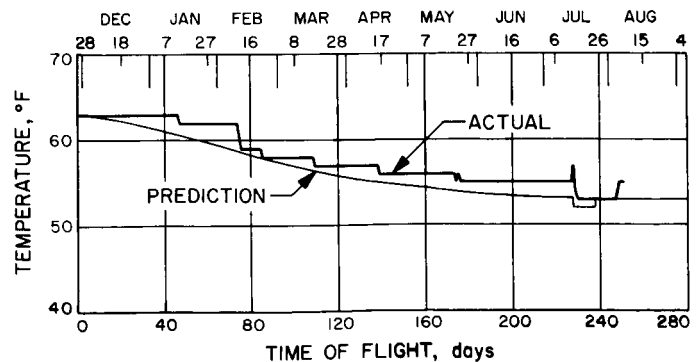


Fig. 11. Mariner IV lower ring flight temperatures

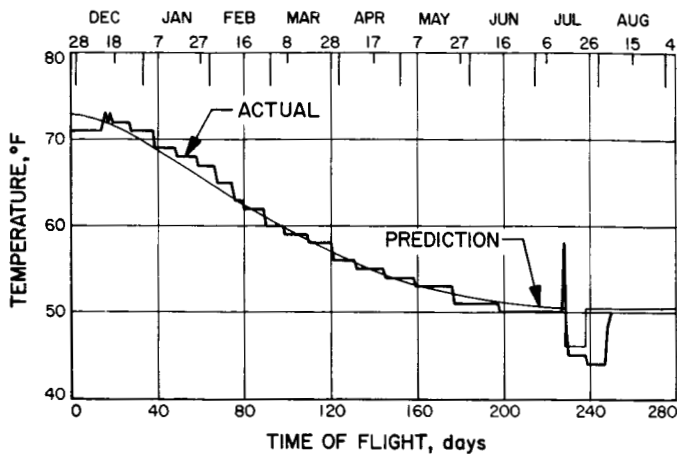


Fig. 12. Mariner IV scan actuator flight temperatures

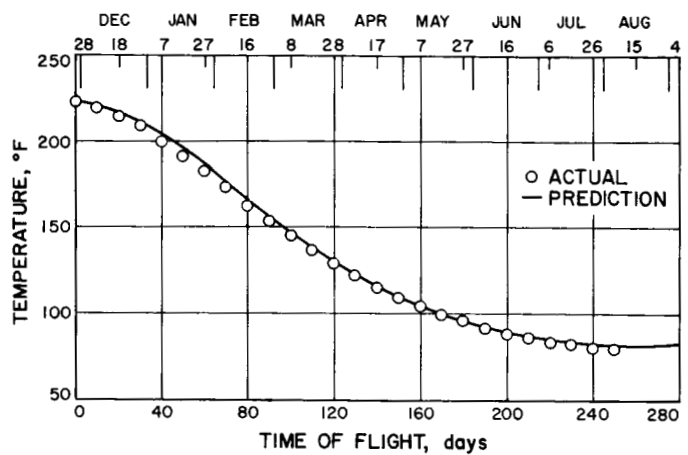


Fig. 14. Mariner IV upper thermal shield flight temperatures

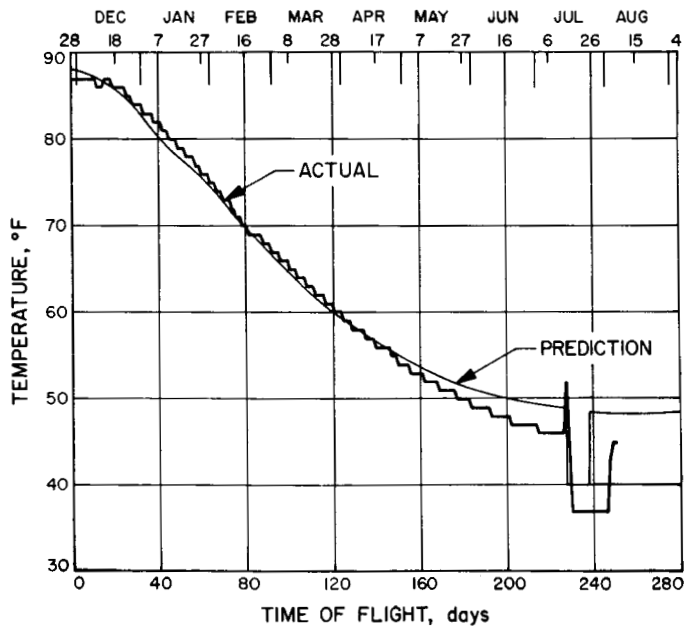


Fig. 13. Mariner IV upper ring flight temperatures

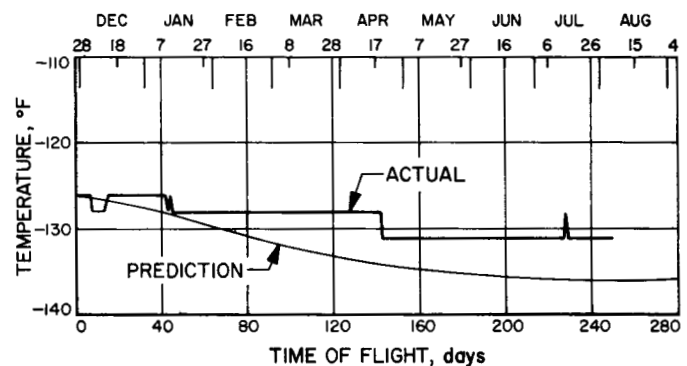


Fig. 15. Mariner IV lower shield flight temperatures

Fig. 23 shows transient data of interest. The transient behavior of the spacecraft in flight was similar to that exhibited during pre-flight tests.

b. Discussion. Cruise Temperatures. As shown in Table 7, initial cruise temperatures were considerably lower than predicted on the basis of space simulator testing. Those items most sensitive to the solar input had the largest discrepancies. The ion chamber and associated electronics was 30°F cooler than predicted; the magnetometer sensor was 20°F cooler, and the solar panels were 15°F low.

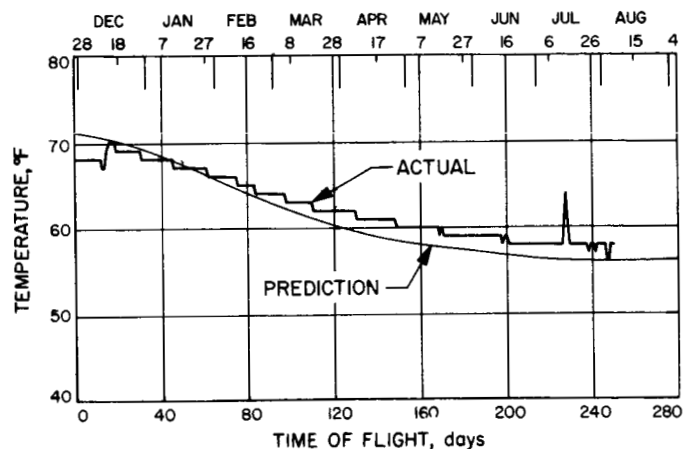


Fig. 16. Mariner IV tape recorder flight temperatures

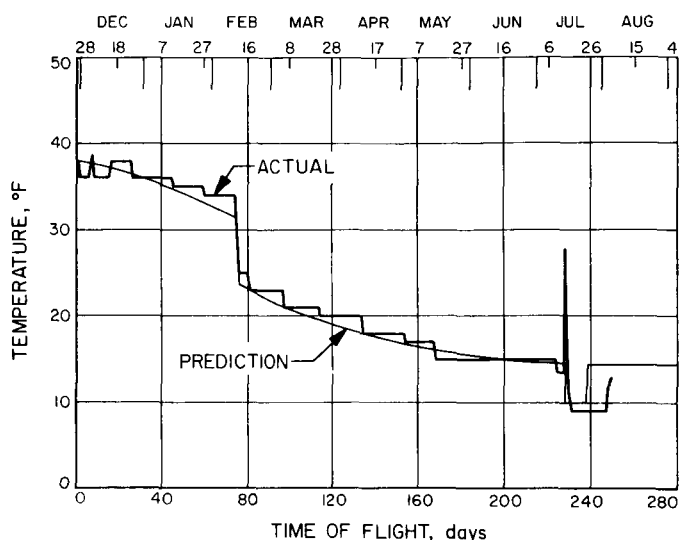


Fig. 17. Mariner IV vidicon flight temperatures

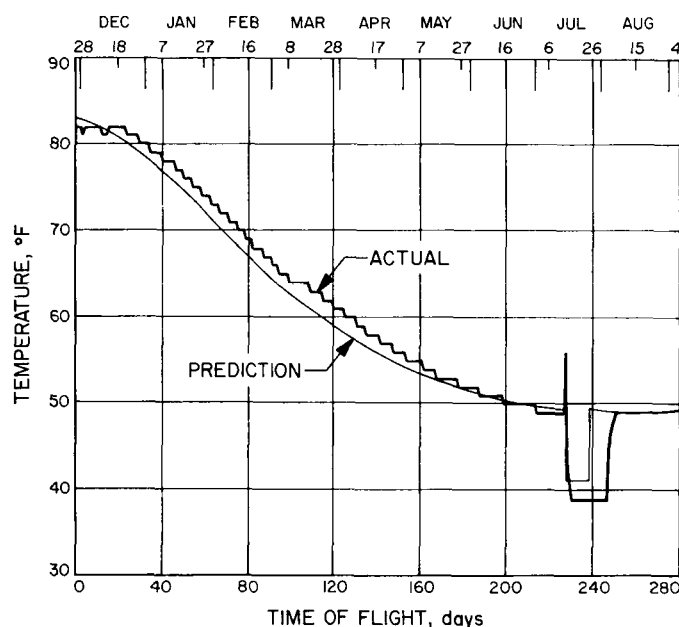


Fig. 18. Mariner IV trapped radiation detector flight temperatures

Post-launch checks in the JPL 25-ft Space Simulator indicate that the spacecraft was probably tested at a solar intensity that was 11% high at Earth cruise and 17% high at Mars cruise. The Absorptivity Standard black and gray samples agree with these findings, as do the solar panel temperatures. The problem appears to have been caused by improper calibration or interpretation of the reference thermopile, but no significant source of thermopile error has yet been discovered.

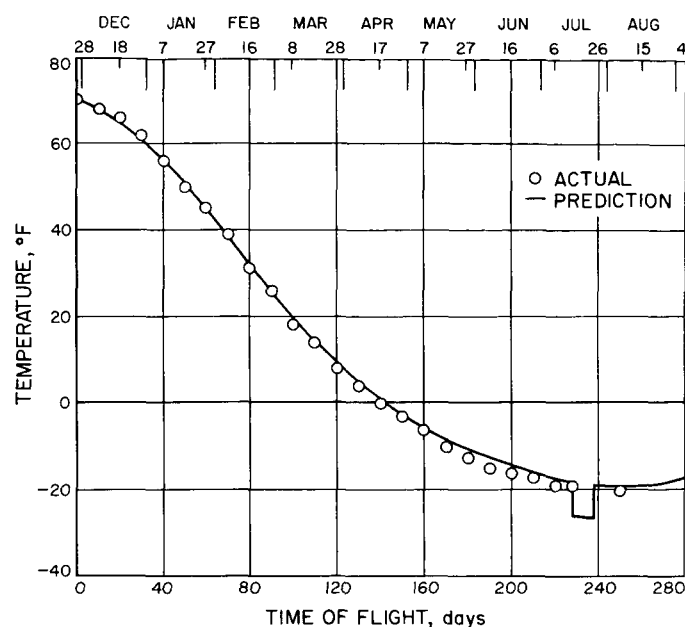


Fig. 19. Mariner IV ion chamber flight temperatures

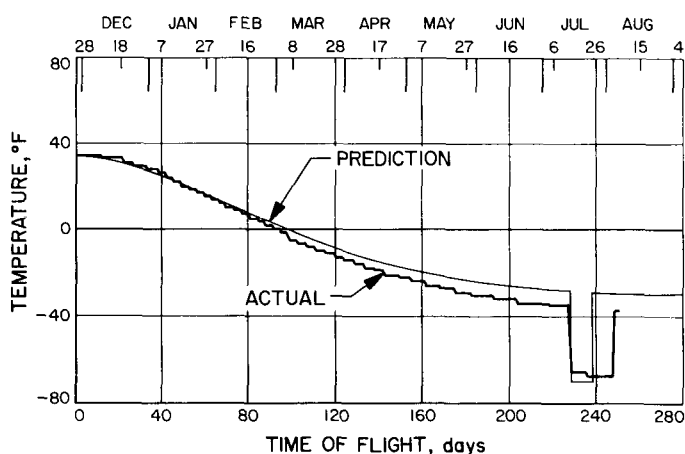


Fig. 20. Mariner IV magnetometer flight temperatures

The above discrepancy does not provide the whole answer to incorrect flight temperature prediction, however, since different components indicated different amounts of intensity mismatch. For example, the solar panels, bus, and ion chamber results require 10, 20, and 30% reductions, respectively, to explain the flight results. After correcting for the solar intensity, however, flight temperatures are within the expected prediction accuracy. The remaining errors are associated with the failure to correct for inherent space simulator limitations, such as decollimation of the solar beam and extraneous inputs of thermal radiation. The *Mariner IV* flight data has resulted in an improved understanding of these error sources.

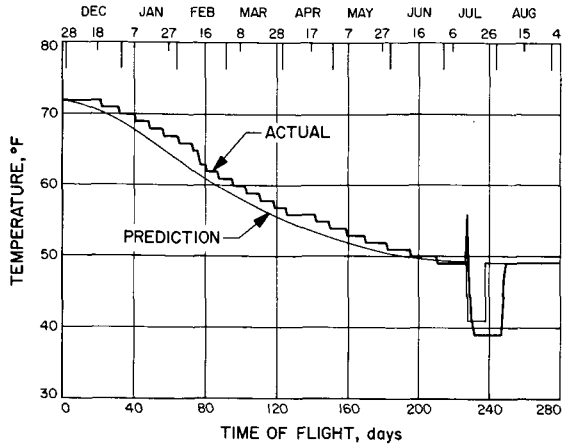


Fig. 21. Mariner IV midcourse fuel flight temperatures

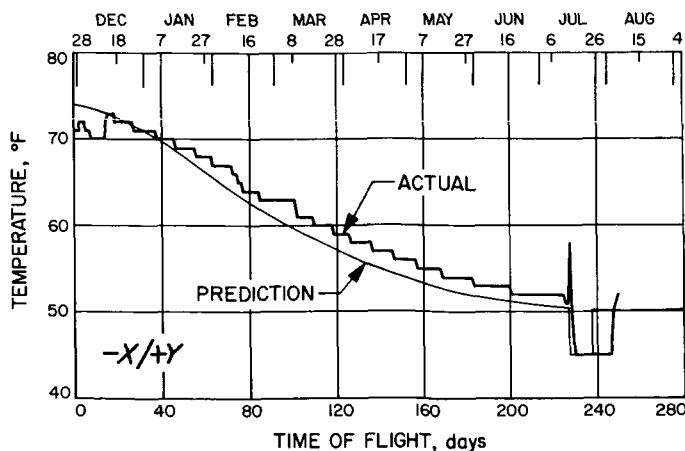
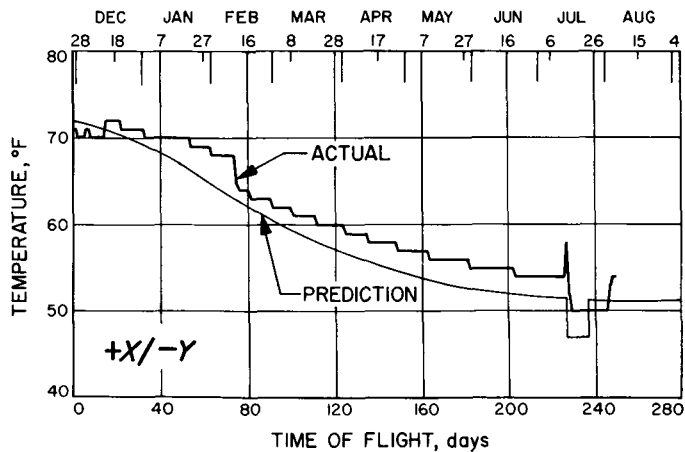


Fig. 22. Attitude control nitrogen (+X/-Y) and (-X/+Y) flight temperatures

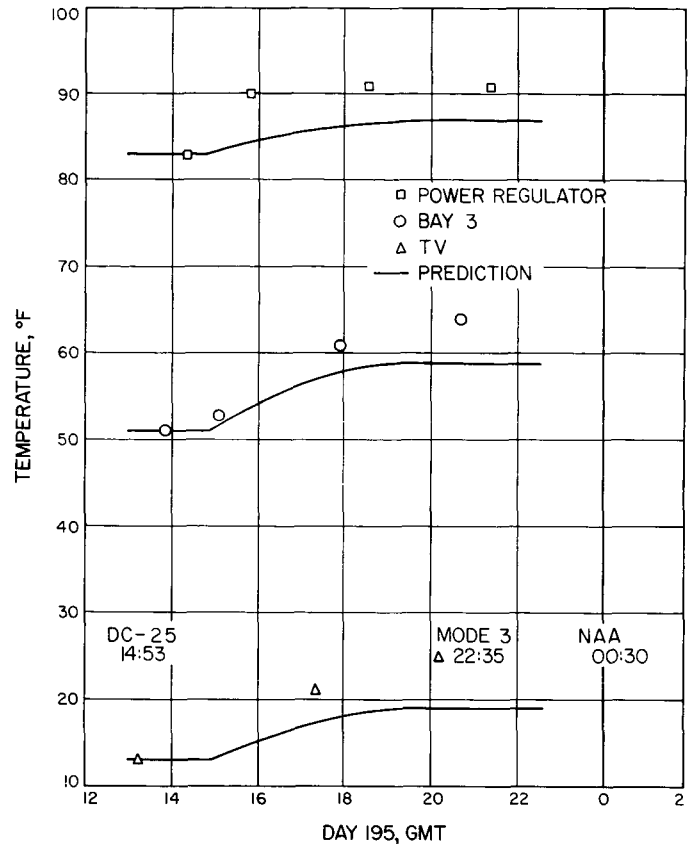


Fig. 23. Encounter transient temperature data

Departures From Post-Launch Predictions. Temperature-time predictions, based on initial flight data and simulator test results, are shown in Figs. 5 to 22. Correlation with actual temperatures is generally good, subject to the following considerations.

A flight anomaly, apparent on inspection of predicted versus actual flight data, was that induced by incorrect solar panel temperatures during simulator tests. The dummy panels were forced to 150°F and 0°F at Earth and Mars, respectively. Corresponding flight temperatures are 135°F and 10°F. On the basis of these tests, the Earth-to-Mars temperature drop was overestimated for bays which have radiative inputs from the panels (primarily odd-numbered bays). The resultant error is small and conservative, but the requirement for careful test interpretation is clear.

The magnetometer temperature gradually departed from the predictions, as shown in Fig. 20. By Mars encounter, the magnetometer was 6°F below the anticipated temperature. This instrument had significant heat inputs from both the Sun and internal power dissipation, and a

deficiency in either input could cause such a drop. The playback mode turn-off of the magnetometer produced a smaller temperature drop than experienced during simulator tests, however; and this result gives a firm indication of below-normal power dissipation in the unit.

The lower thermal shield temperature was somewhat below that observed during simulator tests, and the temperature drop during flight was slightly less than expected. These data indicate that a small heat input (about 2% of a solar constant) to the bottom of the bus existed during the simulator tests.

Launch and Maneuver Transients. Launch temperatures were sufficiently low to prevent overheating during ascent, parking orbit, and Sun acquisition. The launch azimuth resulted in a moderate thermal environment. The spacecraft separation occurred in the shadow of the Earth, and the Sun acquisition time was relatively short. At Sun acquisition, the temperature of the Canopus tracker (100°F upper limit) was 74°F. A shroud-off verification was obtained during the parking orbit by comparing the temperatures of two solar panels.

No constraint was placed on the midcourse maneuver for thermal reasons. The -40 deg pitch selected did not cause extreme solar inputs. A mild heating transient was caused by the increased solar heating, increased power dissipation, and motor burn. All temperatures remained within acceptable limits. The magnetometer sensor heated more rapidly than expected; the discrepancy stemmed from an oversimplified transient thermal analysis. Many of the maneuver events were verified by observation of changes in spacecraft temperature distribution. A qualitative confirmation by temperature measurements was obtained for changes in power distribution, extent and direction of pitch and roll turns, and motor firing.

Thermal Effects of Internal Power Changes. Gyro turns during the early days of flight caused some variation in bus temperatures, particularly in Bay 7. Long-term gyro operation caused a 10°F rise in temperature in this bay.

Fifteen days after launch, the power amplifiers were switched in the radio transmitter in Bay 6. The resulting increase in power dissipation resulted in a 9°F increase in the temperature of Bay 6 and a general increase of 1°F in the bus temperature. These changes were very nearly the same as experienced in preflight space simulator tests.

The cover drop and battery charger turn-off on the 75th day of flight combined to lower bus and scan platform temperatures. Bay 1 dropped 5°F and cooled adjacent bays slightly. The scan platform temperature dropped 8°F due to the increase in unblocked radiation area and decreased heat input from the bus. Since the Mars cruise temperature predictions were based implicitly on a "charger-off" condition, the bus temperatures after the turn-off were nearer the nominal values.

The slight rise in TV temperature at the beginning of the scan sequence coupled with the temperature drop after TV turn-off provided confirmation of normal TV power dissipation and of a normal science cover drop. These data are in good agreement with corresponding space simulator results.

Encounter and Playback Results. Encounter warming transients were similar to those experienced during the cover drop exercise. Fig. 23 compares flight data with MC-2 space simulator results. The battery charger turn-off earlier in flight resulted in more pronounced temperature rises at encounter than occurred during corresponding simulator tests (i.e., the net power increase was greater in flight than in tests).

Bus temperatures (particularly Bay 3) showed a sizable temperature drop during the playback sequence due to the turn-off of cruise science. This drop averaged about 1°F more than experienced in pre-flight tests, probably because louvers were more nearly closed (and therefore less effective) in flight. The magnetometer temperature drop was 12°F less than expected, which indicates that the power dissipation in this sensor was less than had been assumed. A gradual decrease in power consumption during the flight seems likely. The ion chamber temperature transducer dropped off-scale during playback which prevented an estimation of this unit's power consumption. Such an estimate would have been very helpful in failure mode analysis.

Bus temperatures returned to their pre-playback levels at the end of playback. This repeatability rules out louver hysteresis caused by bearing friction.

Overall System Performance. The flight results indicate that the thermal design succeeded and that all thermal control hardware functioned as designed. Discrepancies between predictions and flight data are attributable to an imperfect understanding of test data and spacecraft characteristics, not to hardware degradation or malfunctions. Specifically, louvers, thermal shields, and surface coatings used on *Mariner IV* reliably fulfilled mission

requirements. Louver position indicators showed only fair correlation with corresponding bay temperatures.

c. Absorptivity standard flight results. The Absorptivity Standard has provided good information regarding the degradation of surfaces in space and the problems arising from the testing in the JPL space simulator. The determination of α_s in space has not been successful because the radiation and conduction losses are too large. The ratio of α_s at any given step to the α_s at the initial step is plotted in Fig. 4.

One of the first results noticed was that the ARF-2 paint was yellowing or degrading at a rate much greater than expected due to ultraviolet (UV) exposure. This has continued at a pace about ten times as rapidly as measured during the development of this coating. Subsequent UV exposure tests on ARF-2 samples prepared at the same time as the flight surfaces show rapid degradation, raising the question of the validity of predicting a paint's performance without additional tests of samples prepared and applied by the user.

It was found that the wiring was reversed between the Cat-a-lac black and aluminum silicone sample sensors (P/FR 10112). The sensor idiosyncrasies made this deduction concrete by mid-January 1965. This embarrassing problem probably is due to the cable harness being fabricated to an obsolete drawing. Once this error was discovered, the data for the Cat-a-lac black paint was very consistent and predictable, showing negligible degradation. On February 13, 1965, another interesting event occurred (P/FR 10156) when the black sample switched a month prematurely. This is attributed to a design oversight. The thermometers are insensitive to 100-g accelerations when the mercury meniscus is within the capillary; but, when the meniscus extends into the gas chamber, the thermometer is vulnerable to shocks. During midcourse maneuver the sample temperature was such that the mercury of the number-4 thermometer was probably advanced into the gas chamber and the accelerations of the squibs and midcourse motor shook some mercury loose, changing the calibration.

The aluminum silicone paint had degraded more than expected, but the degree is uncertain due to sensor calibration shifts.

The polished aluminum sample has shown an early degradation greater than that due to the ARF-2 stripe alone. After the first two steps, the data paralleled the degradation due to the stripe alone. This would say that

perhaps the metallic surface was vacuum cleaned early in the flight and then does not further degrade. Two P/FR's were written against the sample. The third (final) step of the number-3 thermometer never occurred (P/FR 10179), and the first step of the number-4 thermometer occurred early (P/FR 10180). The missing step is attributed to a broken thermometer, and the early step is due to the same design oversight mentioned for the black sample.

The Absorptivity Standard showed that the space simulator has solar simulation intensity problems as well as spectral mismatch problems. Comparison of the simulator test and flight data of the black and aluminum silicone samples reveals that the simulator intensity was 10% higher than the simulator instrumentation said. The α of the ARF-2 and polished aluminum for the JPL solar simulation are, respectively, 37% and 9% greater than for sunlight.

E. Guidance and Control

1. Mariner IV Attitude Control Performance From Launch Through Mission Completion

The Mariner IV Attitude Control System has successfully performed all required functions from launch through the post-encounter phase. Anomalies were discovered in the star-sensor roll-control system, the cold-gas thrusters, and in the solar vanes. The star-sensor problem was the only one requiring corrective action, this being accomplished by ground command. The following report is a discussion of these problems as they are viewed from the perspective of the successfully completed mission.

a. Pitch and yaw control. The pitch and yaw control systems have performed in a very satisfactory manner throughout the entire flight. One outstanding anomaly is the fact that the minimum rate increment is twice what it should be, but this is a system problem that is also observed in the roll channel, and is discussed at length in the gas system section. The position deadband is ± 8.6 mr, and the limit cycle rate increment is ± 18.4 μ r/sec. The design value rate increment was ± 9.0 μ r/sec.

b. Roll control. The roll control system, like pitch and yaw, exhibits an excessive rate increment (50% too large).

The deadband is ± 4.5 mr, and rate increment is ± 14.0 μ r/sec; the design value rate was ± 9.0 μ r/sec.

Roll Transients. The most significant problem in roll control is the roll transient problem. The perspective obtained from the long cruise period has clarified the previous theorizing about cause and effect. That is to say, the preponderance of evidence leaves little doubt that roll transients are caused by bright flashes, external to the spacecraft, detected by the star sensor. In the early days of the flight, extensive PTM tests gave no indication that the cause could be an internal, electrical problem. In addition, analysis seemed to rule out cosmic rays, or gamma rays interacting with the star sensor as a cause. The only reasonable theory left was the external flash hypothesis. In the early part of the flight, at a higher data transmission rate (12.6 sec between samples), there were several instances of excessive brightness samples coincident with roll transients. If the transients are caused by the bright flashes, the magnitude of the transients indicated that they must be of very short duration; in the order of <0.5 sec. This would explain why a flash is seldom detected at the time of a transient.

The foregoing evidence suggested the use of a radio ground command (DC-15), to de-activate the brightness gate logic to prevent loss of acquisition. The unqualified success of that decision is proved by the fact that, from that time, there was never a loss of acquisition in spite of about 40 transients that were observed. During this period, the low data rate of 50.4 sec between samples seemed to preclude the possibility of observing any flashes. But, if more corroboration were needed, a fortuitous event occurred on June 9 when a 25-times Canopus brightness sample was obtained coincident with a roll transient.

The question still remains, what is the source of the bright flashes? The most suggestive evidence is the fact that out of the four times that the spacecraft was mechanically disturbed by ground command, at two of these times, there were vigorous roll transients. The first time was at the initial midcourse attempt and the second was at the time of the science cover drop exercise. The mechanical disturbances themselves could not possibly explain the transients, but it is very reasonable to suppose that particles were shaken from the spacecraft such that they floated by the star sensor, causing flashes. Before the flight, it was recognized that the extreme sensitivity of the star tracker made it possible to detect particles 0.005 in. in diameter at 2500 ft from the sensor. However, it was not contemplated that the spacecraft itself could be a serious problem as a source of particles.

An explanation was sought for the source of the continuing roll transients taking place during the long cruise period. The hypothesis was advanced that "undetectable micrometeorites" striking the solar panels could detach surface particles which float by the tracker. Preliminary analysis indicated the possibility of some physical evidence for the micrometeorite impact hypothesis. This was based upon the observation of very small rate impulses in the pitch or yaw channels, correlated with roll transients. It was suggested that a micrometeorite struck a solar panel, imparting a pitch or yaw impulse, and dislodging a particle to cause a roll transient. Subsequent analysis has cast much doubt upon this interpretation with regard to the pitch and yaw impulses. These pitch and yaw impulses can easily be explained as cross coupling effects from the roll axis, due to gas jet and moment arm misalignment. The magnitude of the impulses is about 15% of the roll impulse, about the same observed in normal limit cycle operation. It is interesting that the polarity of the pitch and yaw impulses are always the same, independent of the roll polarity. This could be explained by the positive and negative roll jets having the same misalignment components about the pitch (or yaw) axes.

In addition to the previous discussion, it must be noted that there has never been a correlation of a roll transient with a space science micrometeorite detector event. However, this fact, along with the foregoing discussion, does not rule out micrometeorites as a cause for spacecraft particle generation. This hypothesis postulates micrometeorites below the detectable level. What is now apparent is that there is no proof for this hypothesis, even though it stands as the most reasonable explanation for continuing roll transients.

Recommendations. One obvious solution to the roll transient problem is to provide logic circuitry to tie in the high brightness gate with the gyro shut-down signal. Whenever the gyros are off for cruise operation, the high gate would be removed, hence a bright flash would not start a roll search.

c. Solar vane control system. Thermal Actuators. An attempt was made, on *Mariner IV*, to provide a method of damping that would cause the pitch and yaw limit cycle motion to come to rest within the deadband. The solar vanes were mounted on the solar panels by means of bimetal fittings, exposed to the sunlight through a slotted grid. Limit cycle motion would vary the amount of light falling upon the bimetal fittings, causing them to vary the vane angle according to the angular error of the spacecraft. The direction of the vane angle change was phased properly to slightly reduce the spacecraft

restoring torque (due to solar pressure). The net effect was to reduce the limit cycle velocity, hence, the bimetal fittings would provide "thermal actuator" damping.

The design of the solar vanes was critically affected by area limitations imposed by interference with fields of view of some spacecraft systems. Therefore, at best, the operation would be marginal. In addition, the initial vane deployment mechanism was affected by friction during ground testing that was not present in the space environment. The vanes were deployed completely beyond the nominal position of 35 deg from the plane of the solar panels, out to angles averaging 15 deg. The vane gains were thus considerably degraded.

Early in the flight, it was discovered that there were small changes in the disturbance torques affecting the control system. Some torque changes were directly associated with the gas system valve actuations. At some valve actuations, the disturbance torque was observed to change by 5 dyne-cm. Subsequent analysis showed that the allowable leakage from one valve could create 16 dyne-cm of torque. It is possible that the leakage could vary slightly from one valve actuation to the next, causing variable torques.

The problems associated with vane design and deployment were such that in the presence of the "torque noise" produced by the valves, it was quite impossible to damp out the limit cycle motion within the gas system dead-band. There was not enough gain and speed of response in the thermal actuator system to follow and cancel out the disturbance torques. On the other hand, it is reasonable that some effect upon the control limit cycles should be observed. To this date, no analysis has been able to show any effect. Even when the limit cycle rates are virtually zero and the unbalanced torques are very low, no effect was observed.

In the presence of an unbalanced disturbance torque, which causes constant acceleration, a plot of limit cycle position versus time produces parabolas when there is no control damping. The parabola is a second-order curve, while damping, causing deceleration, produces a higher-order curve. Flight data have been analysed, where the rates and disturbance torques are very low, by using curve fitting techniques. Second- and third-order curves were fitted to the data, and the second-order curves fit the data very closely. The third-order curves did not produce any discernible improvement in the curve fitting. This would indicate that the data, in actual fact, produces second-order curves (parabolas) and there is no damping present.

More analysis would be required to definitely say that the thermal actuator mode is inoperative, especially in view of the faulty deployment. But it appears very strange that no damping effect has ever been observed, and if it exists, it must be much smaller than expected. There are two main areas of uncertainty that could cause poor damping. These are as follows:

- (1) The torque gain of the system is not known from any empirical measurements. The only information is based upon theoretical analysis, which may be modified by important unknowns. One can only make a reasonable guess as to reflectivity (diffuse? specular? magnitude?) and there is practically nothing known about re-emission from rear surfaces.
- (2) The thermal actuator gain (vane angle to spacecraft angle) is only about 0.10. For the allowable limit cycle excursion of 0.5 deg from null, the vane will travel only 0.05 deg with a 3000-sec time lag. In other words, the deflection of the bimetal fitting is so small that it was never actually detected during test operations. If the strip were only slightly bowed longitudinally, the required output might be too small to overcome the initial force.

The important point is that no meaningful test of the system was ever devised because of the great difficulties imposed by the very minute forces and deflections involved. Theoretical analysis may not have been good enough to ensure success.

Further analysis is contemplated to try to arrive at some definitive answer about the damping mode operation. But since it must be based upon theoretical predictions of solar vane performance, it may remain inconclusive as to cause and effect.

Recommendations. From the beginning of the flight, it has been noted that the damping mode has not functioned properly for spacecraft control. But the adaptive mode has proved to be quite adequate for its purpose, and unbalanced torques have been significantly reduced. If the damping mode is discarded, the step size for the adaptive mode could be increased to perhaps 1 deg per step (from the present 0.01 deg) and the offset torques would be quickly rebalanced for efficient operation.

d. Control gas actuator system. The gas usage rate continues to be 3.38×10^{-3} lb/day, indicating a lifetime of about 3.5 yr from encounter. But it should be expected that the usage rate will increase slightly as the spacecraft moves closer to the Sun (increased solar torque) and also

because the roll error signal will be noisier than usual when Canopus is lost and some faint star is acquired. There will *not* be a significant increase in usage, and it should at most, only remove 0.5 yr from the lifetime. The gas usage rate is illustrated in Fig. 24.

As has been previously noted, the minimum rate increments that establish limit cycle performance are about 100% too large in pitch and yaw and 50% too large in roll. Analysis has indicated that the transient operation of the valve, during the 20 msec "minimum on time" valve operation, caused unexpected impulses to be delivered. The transient valve flow was found to be about 30 times the steady-state flow, and when taken into account, accurately explained the observed rate increments for all three axes. This effect was not observed on previous JPL spacecraft because shorter moment arms dictated larger gas nozzles, hence, a larger steady-state flow compared to the transient. The much longer *Mariner IV* moment arms (by a factor of 4) required very small nozzles, and the effect of the transient flow was greatly magnified. The rate increment was established upon the basis of steady-state flow, resulting in a large error from the additional transient flow.

Recommendations. No reliable method has been developed at JPL to measure the minimum impulses required from the gas jets, hence, the transient effect went unobserved until the flight. An effort should be made to develop this capability as a regular flight test operation.

One simple way to solve the transient effect in the valve design would be to restrict the poppet valve exhaust orifice such that it approaches the thruster nozzle in area.

This would diminish the transient flow to steady-state level. Decreasing the "minimum on time" is not practical since the transient flow takes place in the first few milliseconds.

e. Encounter operation. During the encounter period, the only discernible attitude control activity was the observable effect of the scan platform on the limit cycle motion. This was expected and was used to verify proper scan operation. As far as actual planetary effects from Mars on the control system were concerned, none were observed. No gravity gradient torques, atmospheric torques, stray light reflections, or radiation effects were detected.

2. Star Identification Problem

The attitude of the *Mariner IV* spacecraft about the probe-Sun line is stabilized using a celestial tracker designed to acquire and track Canopus, a star in the general direction of the Ecliptic South Pole. Because of uncertainties in the response of the tracker to celestial objects, acquisition is allowed over a preset range of responses to insure that Canopus is always acquirable. The range is wide enough so that other objects are also acquirable. This creates the problem of identifying which object the tracker has acquired after any acquisition.

It is necessary to obtain a solution to the problem since the directions of the midcourse maneuver, the spacecraft high-gain antenna beam, and the scientific instruments for scanning Mars all depend upon acquiring the correct attitude reference star. For the latter two, it is necessary to acquire Canopus; however, the midcourse maneuver can be performed correctly using other stars if the identity of the acquired star is known.

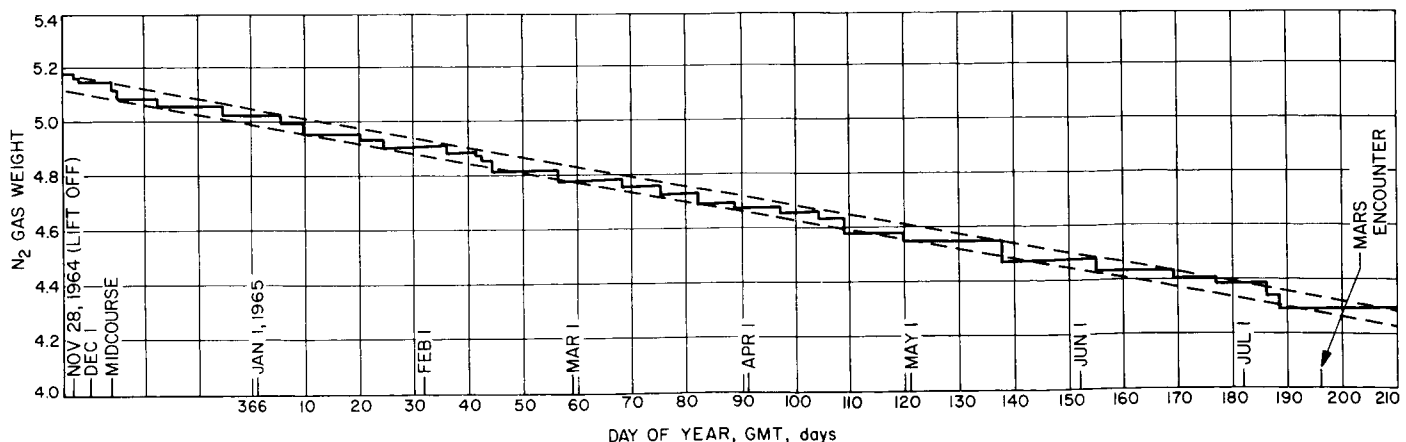


Fig. 24. *Mariner IV* gas usage from telemetry data

To aid in the identification, a procedure was developed using basic statistical decision theory (Ref. 1). The procedure was incorporated into a 7094 computer program entitled The Star Identification Program (SIP) and included in the Space Flight Operations Facility library for the *Mariner IV* operations. This report describes the basic decision theory used and how it was applied to this particular problem. The detailed technical analysis required to apply the theory, details of the computer program, and the actual results obtained during the flight will be presented in subsequent reports.

a. Description of star tracker. As background material, a brief description is presented of the basic coordinate system used, the nominal star acquisition sequence of events, and the star tracker operation.

Cone and Clock Angles. The cone angle (β) of a celestial object, depicted in Fig. 25, is defined as the angle from the probe-Sun line to the probe-object line. The angle between a plane containing the Sun, probe and Canopus and a plane containing the Sun, probe and the object is defined as the clock angle (α) of the object. It is measured from the Sun-probe-Canopus plane and defined as positive in the clockwise direction, when looking towards the Sun from the probe.

Star Acquisition Sequence of Events. The sequence of events for initial star acquisition begins at the completion of Sun acquisition, a few minutes after injection. First, the spacecraft undergoes a controlled roll turn about the probe-Sun line. This turn is in the positive clock angle

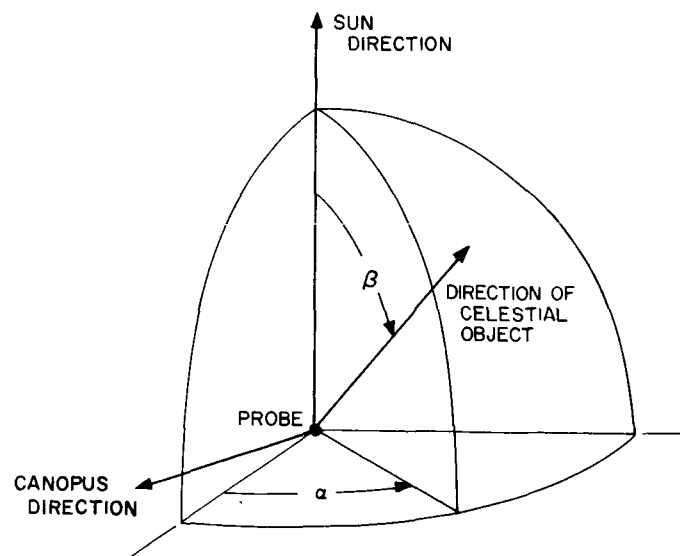


Fig. 25. Cone-clock angle coordinate system

direction at a rate of 3.55 mr/sec and lasts about 16 hr. During this time, telemetered data from the spacecraft magnetometer is obtained for calibration purposes. The tracker is then turned on, and the star search maneuver is initiated. The rate is reduced to 2.02 mr/sec, and the spacecraft rolls until the tracker acquires an object.

In subsequent acquisitions (e.g., after a midcourse maneuver) there is no controlled roll turn, i.e., the star search maneuver automatically begins immediately after Sun acquisition.

Star Tracker Operation. The star tracker has a field of view of approximately 4 deg in clock angle by 11 deg in cone angle. In order to compensate for the changing cone angle of Canopus during the flight, the center of the field of view is preset to 100.3 deg and is periodically decreased in steps of 4.6 deg. The changes in the cone angle insure that Canopus is always in the roll window and acquirable. The roll window (Fig. 26) is the zone of the celestial sphere that the tracker would view during a 360 deg roll turn.

The brightness output of the tracker is a voltage that is a function of the incident light. During the star search

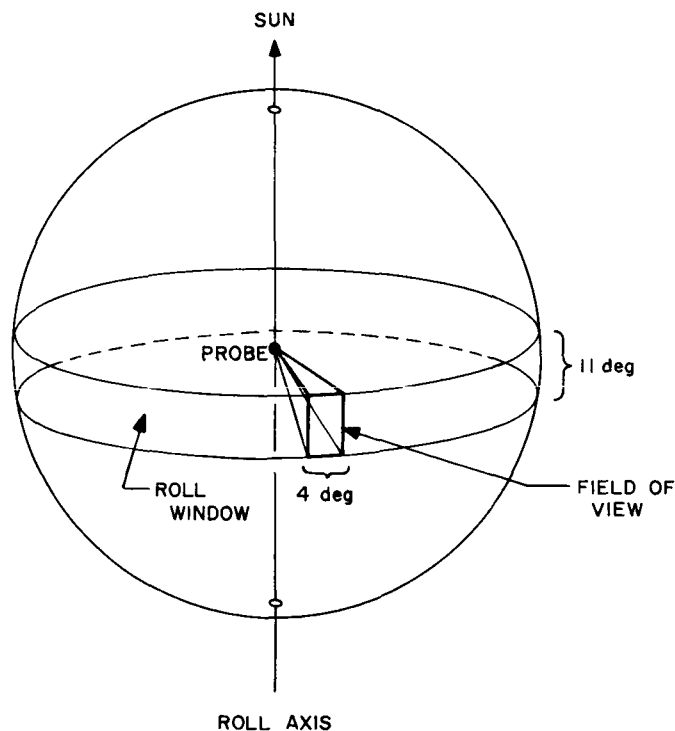


Fig. 26. Star tracker field of view and roll window

maneuver, this voltage is telemetered every 12.6 sec. A mathematical model of the tracker brightness response has been developed based on laboratory tests. For single objects at the center of the field of view, the model is

$$V = C_1 \ln R + C_2; \quad 0 \leq V \leq 3 \quad (1)$$

where V is the voltage, C_1 and C_2 are constants, and R is the Canopus ratio of the object. The Canopus ratio is defined as the ratio of the object's flux in the S-11 spectrum to that of Canopus (the tracker's photocathode has an S-11 spectral response). In the generalized model, R is replaced by a weighted root-sum-square of the Canopus ratios of the stars, planets, and portions of the Milky Way and Zodiacal Light in the field of view. A detailed description of the generalized model and its development will be given in a subsequent report.

The tracker is designed to acquire objects with brightnesses that cause the voltage to be within certain limits and also provide sufficiently large roll error signals of the correct polarity entering the field of view. No model of the roll error signal was developed for the SIP; thus, if an object satisfies only the voltage requirement, it is considered acquirable. The voltage limits were set so that objects having Canopus ratios between approximately 0.25 and 8.0 were acquirable.

b. Basic decision theory. From the decision theory point of view, results of an experiment are used as an aid in deciding to take one of several possible actions. In this application, an action would be to identify a particular celestial object as the one acquired by the tracker. The experiment is the acquisition maneuver; and information obtained from it, which can aid in the identification, comprises the relevant results.

States of Nature, Action Space, and Sample Space. For the moment, assume that there are k objects which may be acquired and denote them by O_1, O_2, \dots, O_k . The latter are called the possible *states of nature*. Further, assume that the acquisition maneuver must end with the acquisition of one of these objects. Let the action a_i be to say that O_i is the true state of nature, i.e., that O_i is the object acquired. The set $A = \{a_1, a_2, \dots, a_k\}$ is the set of possible actions and is called the *action space*. The set S of all possible results obtainable from the experiment is called the *sample space*. The composition of S for this application will be explained below. An element of S (set of results) will be denoted by s , and the random variable which takes on the values in S will be denoted by \bar{s} . The probability density function of \bar{s} will be denoted by $f(s)$, and the conditional probability density function of \bar{s} given

that O_i is the true state of nature will be denoted by $f(s|O_i)$.

Decision Rule and Loss Function. A decision rule d is a function whose domain is S and whose range is A , i.e., to each possible s in S , d associates a certain action a_i in A . The problem in decision theory is to select a decision rule d that is "best" in some sense. To aid in developing the criteria for a "best" decision rule, the concept of a loss function L is considered. For each possible state of nature, this function specifies the loss incurred for every action in A . For the *Mariner* flight path, the geometry is such that the acquirable objects are sufficiently separated so that any erroneous identification would result in serious loss, while no loss occurs for the correct identification. Consequently, the SIP was designed to use a loss function stating that no loss occurs for the correct identification, and that a fixed value L of loss occurs for any incorrect identification. Using the notation $L(a_i|O_j)$ to denote the loss incurred by taking action a_i when object O_j is actually acquired, the loss function used is

$$\begin{aligned} L(a_i|O_j) &= L & \text{if } i \neq j \\ &= 0 & \text{if } i = j \end{aligned} \quad (2)$$

Fortunately, the use of this loss function allowed an easily understood analysis and simple results.

Risk and Selection of a Decision Rule. For a set of results s , a decision rule d specifies that action $d(s)$ is to be taken. If O_i is the true state of nature, the loss incurred is $L[d(s)|O_i]$. In the SIP, if $d(s) = a_i$ the loss is zero, and if $d(s) \neq a_i$ the loss is L .

The risk, $r(d|O_i)$, of using d when O_i is the object acquired is defined as the average loss over the sample space, i.e.,

$$r(d|O_i) = \int_{s \in S} L[d(s)|O_i] f(s|O_i) ds \quad (3)$$

where $s \in S$ denotes that the integral is to be taken over all s in S . In more rigorous terms, $r(d|O_i)$ is the *expected* loss when O_i is the true state of nature.

The average risk, $r(d)$, of using d is the average of the risk over all objects, i.e.,

$$r(d) = \sum_{i=1}^k r(d|O_i) P(O_i) \quad (4)$$

where $P(O_i)$ is the a-priori probability that O_i will be acquired.

In this application, it was decided that the "best" decision rule to use would be that one which minimizes the average risk. The principle of using such a decision rule is called Bayes' principle. This principle was used since it yields the decision which minimizes the risk for any set of results, i.e., it minimizes the a-posteriori risk as explained below. Because of this fact, it is commonly used in problems dealing with nature, i.e., only natural physical forces come into play. Other principles such as minimizing the maximum risk (commonly called the minimax principle) are usually used when dealing with antagonistic forces, i.e., one expects the worst to occur and consequently prepares primarily for the worst. In this application, such a pessimistic approach seemed unwarranted.

The a-posteriori risk, $r(d|s)$, is defined as the expected loss over all objects of using d given a sample point s , i.e.,

$$r(d|s) = \sum_{i=1}^k L[d(s)|O_i] P(O_i|s) \quad (5)$$

where

$$P(O_i|s) = \frac{f(s|O_i) P(O_i)}{f(s)} \quad (6)$$

is the a-posteriori probability that O_i has been acquired. It will now be shown that Bayes' principle is equivalent to selecting a rule which minimizes the a-posteriori risk.

The formula for $r(d|O_i)$ in Eq. (3) can be substituted into Eq. (4) to get

$$r(d) = \int_{s \in S} \sum_{i=1}^k L[d(s)|O_i] f(s|O_i) P(O_i) ds \quad (7)$$

Using Eq. (6), this reduces to

$$r(d) = \int_{s \in S} \left\{ \sum_{i=1}^k L[d(s)|O_i] P(O_i|s) \right\} f(s) ds \quad (8)$$

According to Bayes' principle, d should be chosen to minimize $r(d)$. This requires that for all values of $s \in S$, $d(s)$ be selected to minimize the expression in brackets in Eq. (8). However, this expression is simply the a-posteriori risk given in Eq. (5).

As has been mentioned, the selection of the loss function specified in Eq. (2) led to simple results. Accordingly, it will now be shown that the use of Bayes' principle with this loss function is equivalent to identifying as the object acquired, the one whose a-posteriori probability, $P(O_i|s)$, is a maximum.

It has been shown that Bayes' principle reduces to selecting d so as to minimize the a-posteriori risk, $r(d|s)$, given by Eq. (5). That is, $d(s)$ must equal the action a_j which minimizes

$$r(a_j|O_i) = \sum_{i=1}^k L[a_j|O_i] P(O_i|s) \quad (9)$$

Eq. (2) can be substituted into this formula to obtain

$$r(a_j|O_i) = \left[\sum_{i=1}^k L \cdot P(O_i|s) \right] - L \cdot P(O_j|s) \quad (10)$$

Since the first term is a constant, selecting the a_j which minimizes $r(a_j|O_i)$ is equivalent to selecting the a_j which maximizes the a-posteriori probability, $P(O_j|s)$.

To complete the solution, a computable form of the a-posteriori probabilities must be derived. A form of $P(O_j|s)$ is given in Eq. (6). Since the assumption is made that one and only one object will be acquired, the probability density function $f(s)$ can be written as

$$f(s) = \sum_{i=1}^k f(s|O_i) P(O_i) \quad (11)$$

Eq. (6) can therefore be rewritten as

$$P(O_j|s) = \frac{f(s|O_j) P(O_j)}{\sum_{i=1}^k f(s|O_i) P(O_i)} \quad (12)$$

Consequently, to estimate $P(O_j|s)$, it is sufficient to obtain estimates of $P(O_j)$ and $f(s|O_j)$.

c. Estimation of a-posteriori probabilities. The formulas used to estimate $P(O_j)$ and $f(s|O_j)$ are explained below. However, before explaining the formula for $f(s|O_j)$, the composition of S must be described. In this application, S is the product of three spaces. The primary space is that of the values of equivalent Canopus ratio derived (as shown later) from the tracker voltage telemetered during search, v_1, v_2, \dots, v_n . The second space is that of the telemetered output of the on-board Earth detector, and the last space is of an estimate of the tracker clock

angle at initial acquisition based on the behavior of the on-board magnetometer and omni-antenna. Consequently, s has $n + 2$ components.

A-Priori Probabilities. In order to calculate the a-priori probabilities, the acquirable objects must be determined. This is done utilizing position and brightness information on the brightest 423 stars, the planets, the Milky Way and Zodiacal Light. The 423 stars comprise all stars of the 4th magnitude or greater which might cause a significant response in the tracker. This information is used in conjunction with the mathematical model of the tracker response to estimate what the tracker voltage would be at the clock angle of each star and planet in the roll window. If the resulting voltage is within the outer 3σ values of the gate limits, it is deemed acquirable. Also, the output voltage at each integral clock angle where there is no star or planet is checked to see if the voltage due to the Milky Way and Zodiacal Light lies within the 3σ gate limits. If so, it is also considered as an acquirable "object."

Let α_i and v_i denote the clock angle and voltage output at object O_i . Let p_i be the probability of acquiring O_i if it comes within the tracker's field of view. Let v_l and v_u be the design values of the lower and upper gates. Let σ_v be the standard deviation of a gate (assumed to be the same for each gate).

The formula used to estimate p_i is

$$\begin{aligned}
 p_i &= 1 && \text{if } v_l + 3\sigma_v \leq v_i \leq v_u - 3\sigma_v \\
 &= \frac{v_i - v_l + 3\sigma_v}{6\sigma_v} && \text{if } v_l - 3\sigma_v < v_i < v_l + 3\sigma_v \\
 &= \frac{v_u + 3\sigma_v - v_i}{6\sigma_v} && \text{if } v_u - 3\sigma_v < v_i < v_u + 3\sigma_v \\
 &= 0 && \text{otherwise.}
 \end{aligned} \tag{13}$$

By design, the probability of acquiring Canopus if it enters within the field of view is always unity.

Fig. 27 indicates that the probability of acquiring O_i is the probability of starting search in the "pie segment" prior to O_i and acquiring O_i , plus the probability of starting in the segment prior to O_{i-1} , missing O_{i-1} and then acquiring O_i , etc.

Assume that the acquirable objects are ordered by increasing clock angle, and that the tracker is equally

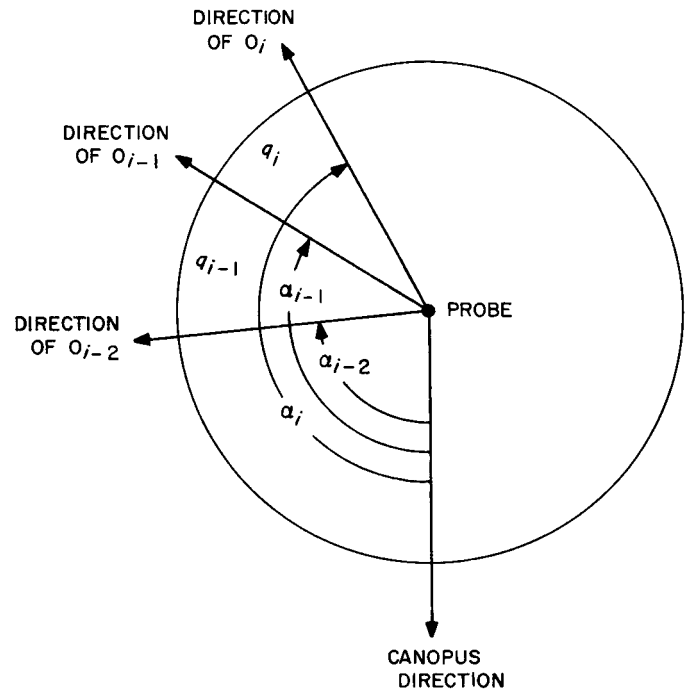


Fig. 27. Geometry of a-priori probabilities

likely to start search at any clock angle (actually, the latter is true only for initial acquisition). The probability q_i of starting in the segment prior to O_i is then

$$\begin{aligned}
 q_i &= \frac{\alpha_i - \alpha_{i-1}}{360} && i = 2, 3, \dots, k \\
 q_1 &= \frac{\alpha_1 + 360 - \alpha_k}{360}
 \end{aligned} \tag{14}$$

The a-priori probability is therefore given by

$$P(O_i) = p_i q_i + p_i \sum_{j=1}^{k-1} q_{i-j} \prod_{m=1}^j (1 - p_{i-m}) \tag{15}$$

where $i - j$ is replaced by $k + i - j$ if $i \leq j$ and $i - m$ is replaced by $k + i - m$ if $i \leq m$.

Earth Detector. The Earth detector field of view covers the region from approximately 72.5 deg to 98.5 deg in clock angle and 34 deg to 117 deg in cone angle. It was designed so that the Earth would be detected at initial acquisition if Canopus were acquired. A mathematical model for the detector's response has been developed and will be explained in detail in a future report. For each acquirable object, this model is used in conjunction with position and brightness information of the Earth and Moon to estimate what the Earth detector output would be if the star tracker were locked on the object. Denote

the output by e_i and the telemetered output by e . Assume for the moment that this is the only information known, i.e., $s = e$. Then, the form assumed for $f(s|O_i)$ is

$$f(e|O_i) = \frac{1}{(2\pi)^{1/2}\sigma_e} \exp \left\{ -\frac{1}{2} \left(\frac{e - e_i}{\sigma_e} \right)^2 \right\} \quad (16)$$

where σ_e is the standard deviation of e . The latter procedure provides an estimate of the a-posteriori probability based *only* on Earth detector information, i.e.,

$$P(O_i|e) = \frac{f(e|O_i)P(O_i)}{\sum_{j=1}^k f(e|O_j)P(O_j)} \quad (17)$$

Magnetometer—Antenna Position Estimates. During the first part of the controlled roll turn prior to initial acquisition, the spacecraft is in the Earth's magnetic field. By relating the telemetered output of the on-board magnetometer to the Earth's field at the spacecraft, an estimate of the spacecraft roll position during this time is obtained.

The roll rate for the rest of the turn is estimated from observations of signal strength maxima and minima at the receiver stations due to the four-lobed pattern of the low-gain antenna. Using the initial fix based on the magnetometer, and integrating the rate deduced from the observations at the receiver stations, an estimate of the tracker clock angle at search start is obtained. The angle at acquisition is obtained by further integrating the telemetered roll rate. The preceding procedure will be described in more detail in a future report.

Let α_m be the estimated tracker clock angle at acquisition. In a manner similar to the Earth detector, assume $s = \alpha_m$. Then, the a-posteriori probability based only on the magnetometer-antenna estimate is computed by replacing $f(s|O_i)$ with

$$f(\alpha_m|O_i) = \frac{1}{(2\pi)^{1/2}\sigma_m} \exp \left\{ -\frac{1}{2} \left(\frac{\alpha_m - \alpha_i}{\sigma_m} \right)^2 \right\} \quad (18)$$

where σ_m is the standard deviation of α_m and $(\alpha_m - \alpha_i)$ is computed modulo 180 deg.

Tracker Voltage. From tracker tests, it appeared that errors in the tracker output were log-normally distributed. Consequently, instead of using the telemetered voltages directly, they were transformed into "effective Canopus

ratios." Effective Canopus ratio is defined as the inverse of Eq. (1), i.e.,

$$R = \exp \left\{ \frac{V - C_2}{C_1} \right\} \quad (19)$$

Thus, assume for the moment $s = R = (R_1, R_2, \dots, R_n)$ where

$$R_j = \exp \left\{ \frac{v_j - C_2}{C_1} \right\}, \quad j = 1, 2, \dots, n \quad (20)$$

In this case, $f(R|O_i)$ was assumed to be multivariate normal, i.e., using matrix notation

$$f(R|O_i) = \frac{|\Lambda^{-1}|^{1/2}}{(2\pi)^{n/2}} \exp \left\{ -\frac{1}{2} (R - \mu_i) \Lambda^{-1} (R - \mu_i)^t \right\} \quad (21)$$

where Λ is the covariance matrix

$$\Lambda = \begin{bmatrix} \sigma_R^2 + \sigma_B^2 & \sigma_B^2 & \dots & \sigma_B^2 \\ \sigma_B^2 & \sigma_R^2 + \sigma_B^2 & \dots & \sigma_B^2 \\ \vdots & \vdots & \ddots & \vdots \\ \sigma_B^2 & \sigma_B^2 & \dots & \sigma_R^2 + \sigma_B^2 \end{bmatrix}_{n \times n} \quad (22)$$

and σ_R and σ_B are the standard deviations of the noise and bias in R_i . The vector of means is

$$\mu_i = (\mu_{i1}, \mu_{i2}, \dots, \mu_{in}) \quad (23)$$

where μ_{ij} is the expected value of the j th telemetered effective Canopus ratio assuming O_i is acquired. The value of μ_{in} can be estimated by computing the effective Canopus ratio at the clock angle α_i using the mathematical model of the tracker response and position and brightness information of the celestial objects. Similarly, μ_{ij} can be estimated at a clock angle α_{ij} given by

$$\alpha_{ij} = \alpha_i - \bar{r}(T_n - T_j) \quad (24)$$

where \bar{r} is the average telemetered roll rate, T_n and T_j are the times that v_n and v_j were telemetered.

Composite Probabilities. In order to compute the a-posteriori probabilities, a form is needed for $f(s|O_i)$ when $s = (e, \alpha_m, R)$. It was assumed that these quantities were *conditionally* independent, i.e., having acquired an object, the error of one was independent of what the errors of the others were. Thus

$$f(e, \alpha_m, R|O_i) = f(e|O_i) f(\alpha_m|O_i) f(R|O_i) \quad (25)$$

With these forms, the a-posteriori probabilities can be computed and the object with the largest value identified as the object acquired. The SIP operations which perform the computations will be described in a future report.

d. Maximum likelihood and least squares solutions. In conclusion, two other proposed solutions to the Star Identification Problem will be discussed. It will be shown that they can also be considered as decision theory solutions with restrictions added to the actual solution used.

For simplicity, consider only the tracker output. The maximum likelihood solution is to identify as the acquired object the one with the maximum value of $f(R|O_i)$. The least squares solution is to select the one with the smallest value of

$$SSQ = \sum_{j=1}^n (R_j - \mu_{ij})^2 \quad (26)$$

Maximum Likelihood. Suppose that for the a-priori probabilities it was decided to assume each object was equally likely, i.e.,

$$P(O_i) = \frac{1}{k} \quad (27)$$

The formula for $P(O_i|R)$ is then

$$P(O_i|R) = \frac{f(R|O_i)}{kf(R)} \quad (28)$$

Thus, the maximum value of $P(O_i|R)$ corresponds to the maximum value of $f(R|O_i)$. That is, the decision theory solution would reduce to a maximum likelihood solution if, a-priori, the objects were assumed equally likely to be acquired.

Least Squares. Assume further that the value of σ_B is set to zero. The formula for $f(R|O_i)$ becomes

$$f(R|O_i) = \left(\frac{1}{(2\pi)^{1/2}\sigma_R} \right)^n \exp \left\{ -\frac{1}{2\sigma_R^2} \sum_{j=1}^n (R_j - \mu_{ij})^2 \right\} \quad (29)$$

It can readily be seen that selecting the maximum value of $f(R|O_i)$ is equivalent to selecting the minimum SSQ as defined in Eq. (26). That is, the maximum likelihood solution reduces to the least squares solution if it is assumed that there is no bias.

3. Spacecraft Power System

a. Mariner IV flight analysis. Operation of the power system was completely normal throughout the encounter sequence; no anomalies were noted. During the cruise portion of the flight preceding encounter, power readings were constant with a power demand from the solar panels of 164 watts. Initiation of the encounter sequence with a DC-25 command increased the power demand to 197 watts as expected. Stopping of the scan system platform with a DC-24 was verified by the power system when the main regulator output current decreased 1 data number.

At approximately 20:23 GMT during the encounter sequence, the battery voltage decreased 1 data number, 0.13 v DC, to 36.71 v DC due to increased battery temperature. The battery temperature increased 3°F as a result of increased power dissipation in the adjacent cases after turn-on of encounter science.

Operation of the power system was also normal after DC-26 and DC-2 commands were sent. As expected, power levels exceeded those of normal cruise only by an amount equal to the 2.4 Kc/s power to the tape recorder electronics. At 07:25 GMT, the battery voltage increased 1 data number, returning to its pre-encounter value of 36.84 v DC. This increase was a normal result of the 1°F decrease in battery temperature that occurred at encounter science turn-off. Mode 1 power data following MT-9 was completely normal with a power demand from the solar panels of 147 watts.

After playback of the TV pictures was completed, the spacecraft was returned to cruise mode operation. Power demand returned to its pre-encounter value of 164 watts, and all power measurements were normal. At the present time, the spacecraft is in a cruise mode and all elements of the power system, with the possible exception of the battery with its higher-than-expected voltage (see SPS 37-33), are operating normally.

F. Telecommunications

1. Ground Command Subsystem Description

a. Introduction. The primary function of the ground command read write verify (RWV) subsystem (Fig. 28) in the *Mariner C* program is to modulate a subcarrier

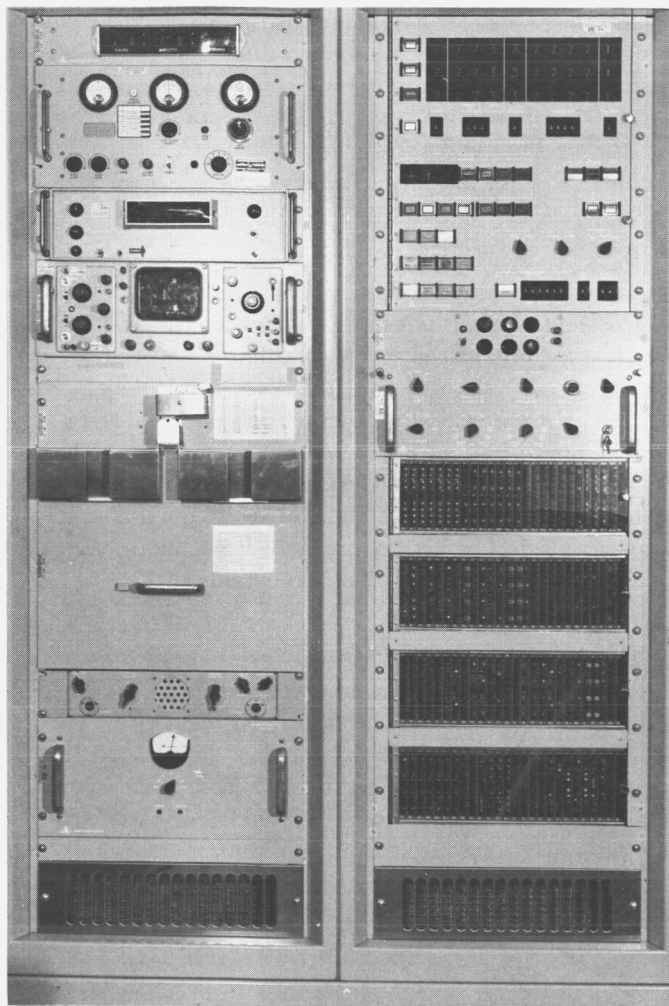


Fig. 28. Ground command subsystem

with a binary word which is received and decoded by the spacecraft flight command subsystem. The command word in the *Mariner C* program is a 26-bit binary word, which may fall into one of two general categories, the discrete command (DC) and the quantitative command (QC). There are 29 DC and 3 QC commands. Each DC command instructs the spacecraft to perform a specific function. The three QC commands are used for midcourse correction only and program the spacecraft to roll, pitch, or burn the thrust motor.

The intermediate link between ground command and flight command is the radio subsystem. The ground radio subsystem, located at DSIF stations, phase modulates the S-band carrier with the information received from the ground command subsystem.

During normal operation, the ground command subsystem continually monitors the signal transmitted by

the radio subsystem. The signal is detected in the same manner as that used by the spacecraft. The detected command bits are then compared with the command bits transmitted by the ground command system. If any discrepancy is noted between the two signals the ground command system inhibits transmission of the command signal to the radio transmitter. The resultant loss of command modulation causes the spacecraft flight command subsystem to lose lock, which in turn inhibits the processing of any commands.

b. Modes of operation. The ground command subsystem is capable of operating in three modes. One of these modes was mentioned above, being able to send a command word to the spacecraft. The system may also operate in a verify mode, in which it is able to simulate transmission of a command word. During this mode of operation, the system performs exactly the same functions as it does during transmission, except that the command word is not sent to the radio subsystem. In the third mode of operation the RWV checks the paper tape received via teletype lines, which contains the command word.

During a typical operation, QC command information is sent from the SFOF over teletype lines to the DSIF station, and the information is then relayed to the spacecraft. In order to detect errors prior to transmission the same command word is sent over the teletype lines three times and punched on paper tape at the DSIF station. The RWV checks the paper tape to verify the word format and insures that each of the three words is identical. Once this process is completed the RWV punches the command word on paper tape. If the command is valid, it is then processed by the RWV, which goes through a verify cycle to check its own operation before finally transmitting the word to the spacecraft.

c. System description. The RWV operation may be subdivided into three general functions: the control and verify function, the modulator function, and the detector function. All RWV functions are derived from a solid state negative true logic system, which, when integrated, forms a system that continually tests for errors during operation.

All system functions are sequenced by the program control counter, an 8-position shift register that is enabled by any one of eight separate AND gates. The position of the bit in the shift register determines the operation to be performed. As soon as the system completes an operation, the bit is clocked to the next position in the shift

register by enabling the proper AND gate. This operation is repeated until the RWV has completed its cycle, which takes approximately 56 sec.

To insure reliability, the RWV employs error detection circuitry to verify many of its functions. It also has the capability of insuring proper operation of its error detection circuitry. Any one of six error detection circuits may be checked by selecting the desired circuit on the RWV console and reading a predetermined program tape. Several of the important checks performed are: verifying that operations are sequenced in the prescribed manner; insuring that the RWV modulator and detector are in sync; and making a bit-for-bit check of the information sent to the spacecraft during transmission.

During normal operation, the signal sent to the RF transmitter is inhibited if an error is detected; however, in case of an emergency the system is capable of operating by manually over-riding the error circuitry or by operating in the emergency mode. When in the emergency mode, no checks are performed and the word is transmitted by circuitry not employed during normal operation. It suffices to say that this mode would be used only in case of extreme emergency.

The purpose of the RWV modulator is to bi-phase modulate a subcarrier with the 26-bit binary command word (Fig. 29). This is accomplished by employing a

phase shift keyer which maintains the phase of a coherent sine wave for a binary zero but shifts its phase by 180 deg for a binary one. The modulator basically consists of four units: the phase shift keyer (PSK); pseudonoise (PN) generator; a binary counter which produces a frequency defined as 2FS; and a modulo-two adder.

In order to employ PSK techniques, it is necessary to establish phase coherence or sync between modulator and detector. Sync is established by employing two PN generators, one at the RWV modulator and the other at the spacecraft flight command detector. When the two PN generators emanate the exact code permutation, they are in phase with respect to each other, and phase coherence is established. At this point the spacecraft PN generator is in lock with the RWV PN generator and is capable of following the ground PN generator within reasonable frequency and phase deviation.

The ground command PN generator consists of a shift register, employing modulo-two feed-back to create a pseudonoise code which repeats itself once every second. The PN generator clock frequency, defined as 2FS, is derived from a variable oscillator and a binary counter, which acts as a divider. Initial lock acquisition is achieved by decreasing the oscillator frequency and thereby decreasing the 2FS frequency. Since 2FS is the clock for the PN generator, the 2FS offset causes the RWV PN

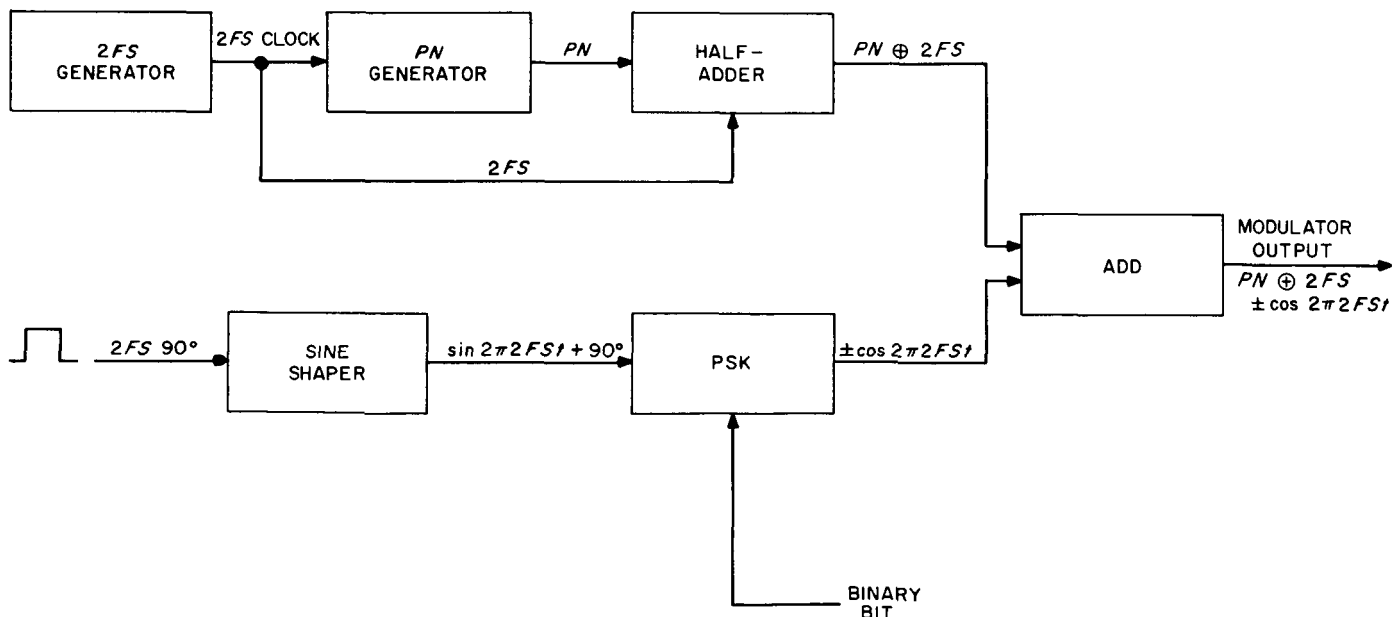


Fig. 29. Ground command modulator

generator to drift with respect to the spacecraft generator. The $2FS$ offset chosen is slow enough to allow lock when correlation exists between the two PN generators and at the same time to insure that lock occurs within a reasonable length of time.

The block diagram of the RWV modulator (Fig. 29) shows how sync and data are processed through the RWV modulator. The PN code and $2FS$ are half added to produce $PN \oplus 2FS$ which is used by the spacecraft to establish sync. The data portion of the word is phase modulated by forming from a square wave a sine wave whose equation is

$$\sin 2\pi 2F_s t \text{ } 190 \text{ deg}$$

The sine wave is then sent to the PSK which is keyed by the word bit. With zero volts (binary zero) applied, the PSK maintains the phase of the input sine wave. With -6 v (binary one) applied, the PSK shifts the sine wave by 180 deg . Hence, the equation of the waveform of the PSK output is $\pm \sin(2\pi 2F_s t + 90)$ or $\pm \cos 2\pi 2F_s t$. The

data portion and sync portion of the word are then added to produce the output of the modulator

$$PN \oplus 2FS \pm \cos 2\pi 2F_s t$$

The RWV detector is employed to demodulate the command word transmitted by the radio system and to insure that the information sent by the RWV is the same as that transmitted by radio. It may also be said that the RWV detector simulates the flight command detector, thereby providing a means to check system operation before sending a word to the spacecraft.

The RWV employs an S-band phase lock loop receiver to demodulate the RF signal. After the RF carrier signal is removed, the submodulated portion of the signal is received by the RWV detection circuitry. This circuitry employs the same concepts found in the modulator: a PSK, a $2FS$ generator, a PN generator, and a modulo-two or half adder (Fig. 30). The incoming signal passes through a PSK, a sine wave shaper, and a band pass

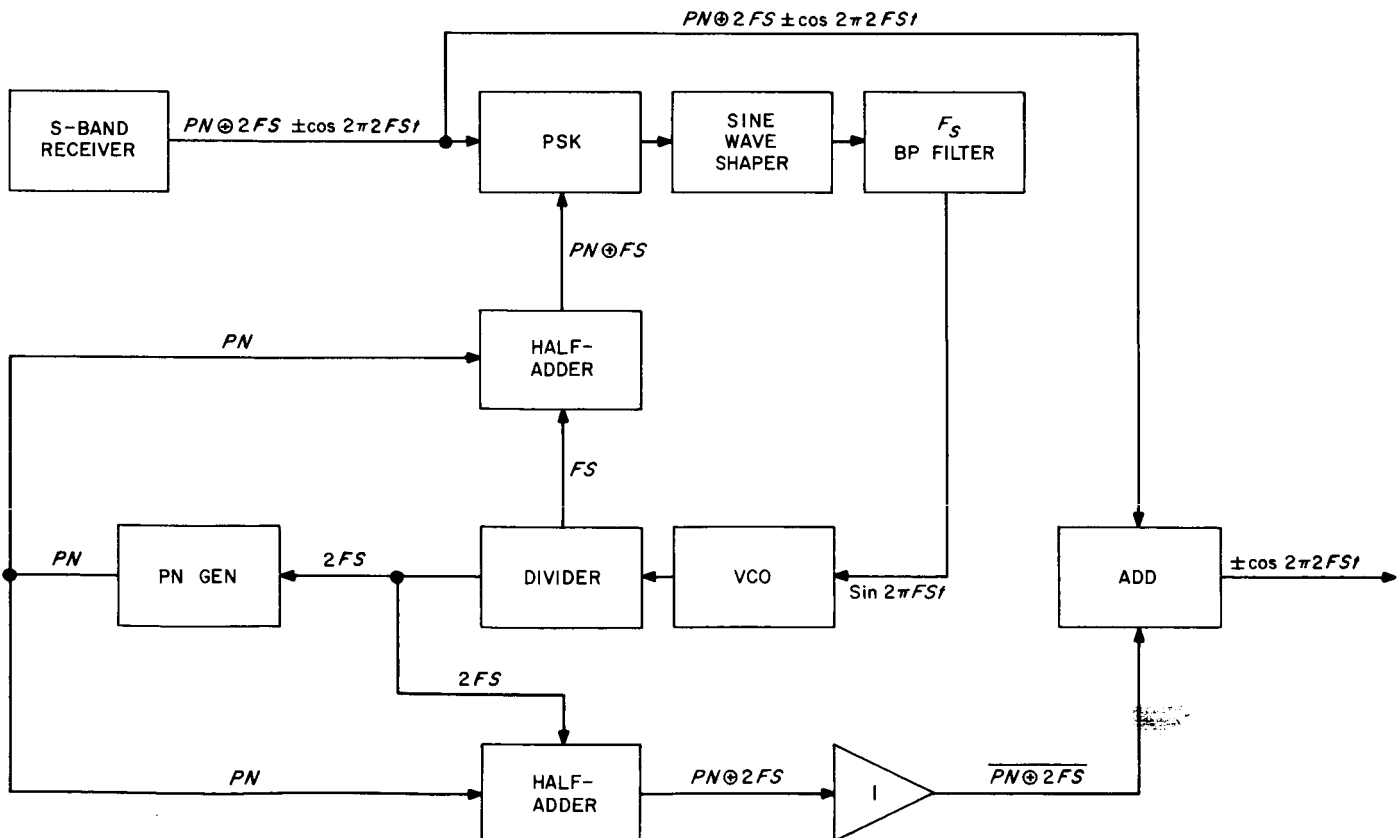


Fig. 30. Ground command detector

filter, that produces a coherent sine wave whose equation is $\sin 2\pi FSt$. Once established, this frequency is used as one of the voltage controls to a VCO. This oscillator provides the input to a divider which produces $2FS$, the clock for the detector PN generator. After sync is established between the modulator and detector PN generators, the original command word may be reconstructed. The detector PN code and detector $2FS$ are half added and put through an inverter to produce $\overline{PN' \oplus 2FS'}$; where prime denotes that the signal is derived from the detector. $\overline{PN' \oplus 2FS'}$ is then linearly added to the modulator signal $PN \oplus 2FS \pm \cos 2\pi 2FS t$ whose sum is equal to $\pm \cos 2\pi 2FS t$. Since the phase of the cosine wave is determined by the binary bit transmitted by the RWV, a comparison may readily be made between the RWV modulator output and the RWV detector output.

d. Displays. The RWV display console is shown in Fig. 31. Since many of the displays are self-explanatory, only several of the more important will be mentioned.

The time of day display in the upper left corner is internally wired to the control logic. By selecting the automatic operating mode, the RWV will automatically send a command word which will be initiated when time of day is equal to the timed start thumbwheel setting. The remaining displays on the left side of the console are: the input and output signal strength of the S-band receiver; a counter which displays multiples of the FS frequency; and an oscilloscope.

In the upper right corner, the 26-bit command is displayed in octal form. The word is displayed three times, and each display corresponds to the particular register which is used at different intervals during operation. The vehicle subcarrier displays indicate whether the telemetry received from the spacecraft is good, questionable, or bad. It also tells whether or not the spacecraft and RWV are in sync and displays the offset from the $2FS$ frequency. The remaining displays are self-evident and relate to functions such as: power on, mode of operation, and word in process.

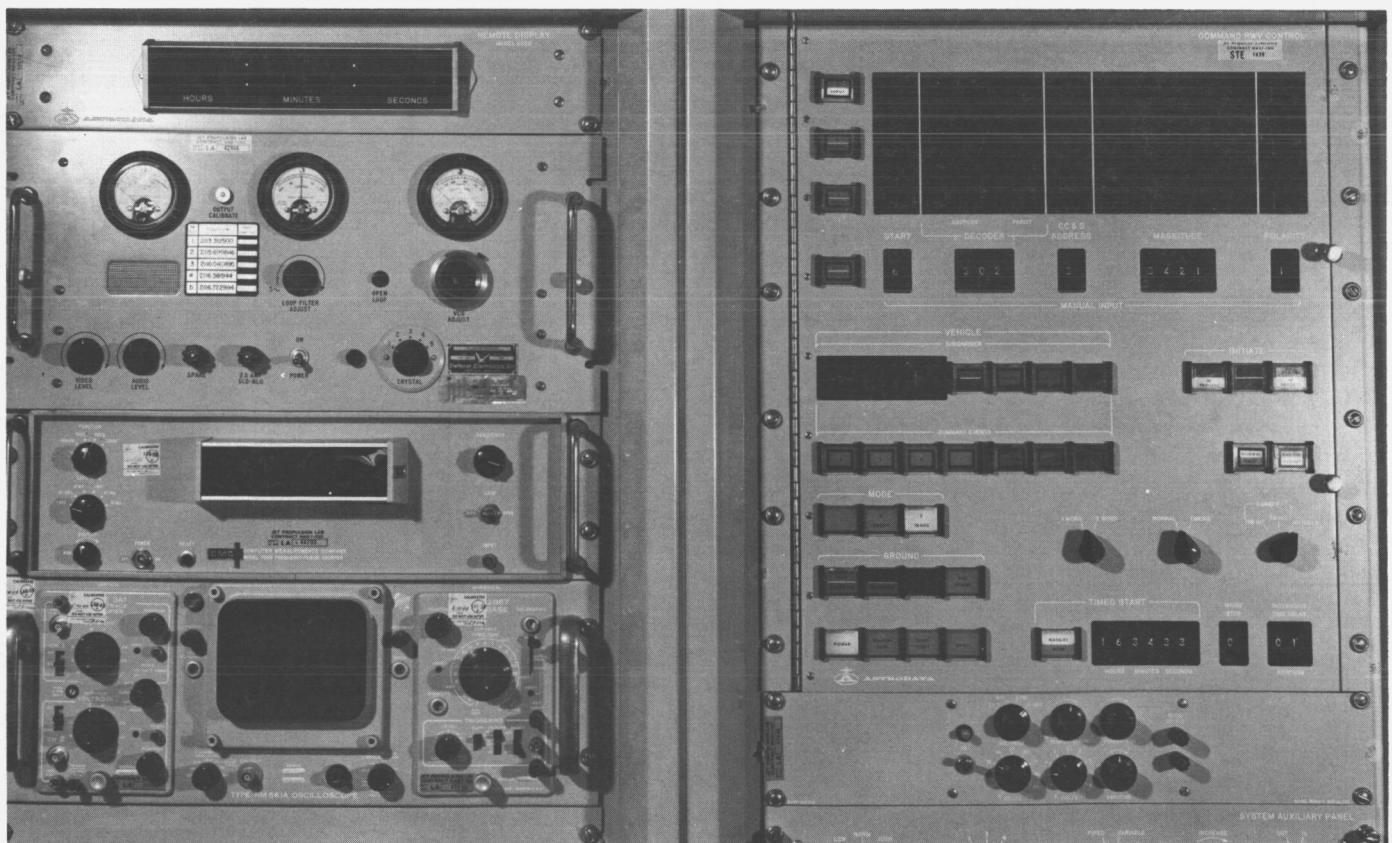


Fig. 31. Ground command display console

G. Space Sciences

1. Interplanetary Color Photography

a. Introduction. Observation indicates that a high proportion of planet reflectance is white light. Vivid sensations of color from objects illuminated by sunlight is essentially a close range phenomenon. As range increases, coloring becomes diluted. Hence interest for exploratory, long range (50 to 5000 mi) planetary photography is directed at the reproduction of diluted color tones, i.e., tones that enter the white region or the grey region.

The reproduction of color requires a technology that involves the superposition of three primaries. With adequate spectral separation and accurate quantitative adjustment, any color in nature, including white, may be satisfactorily matched with three selected components. Only in special cases can a match be obtained when any one of the selected components is absent. For example, in the reproduction of fully saturated colors occupying a narrow band two primaries may suffice.

Adequate spectral separation of the three primaries is secured by a selection from the red, green, and blue regions. A mixture of red and green light produces yellow. With the addition of a correctly proportioned quantity of blue light, a colorless sensation arises and is designated white. This phenomenon is demonstrated every day with the reception of compatible television color broadcasting.

b. Color in planetary photography. As with all other photography, planetary photography may be related to the Munsell system for defining color. In this system, color has three attributes: hue, saturation, and brightness. Saturation represents the intensity of the coloring or the extent to which the color is diluted with white.

The relationship of white to colors is illustrated in the CIE chromaticity diagram of Fig. 32. The curve represents the locus of fully saturated pure spectral colors. Nonspectral colors, or purples that are a mixture of red and blue, form the base of the color curve. Generally, the y ordinate is associated with luminance, and the x ordinate is associated with chromaticity. Greens tend to have high luminance, while reds and blues have progressively lower luminance. Inserted into this diagram is illuminant C which represents north-sky daylight with coordinates $x = 0.3101$ and $y = 0.3163$. Illuminant C will be defined as white, i.e., when observed by the eye, no color sensation will be evoked.

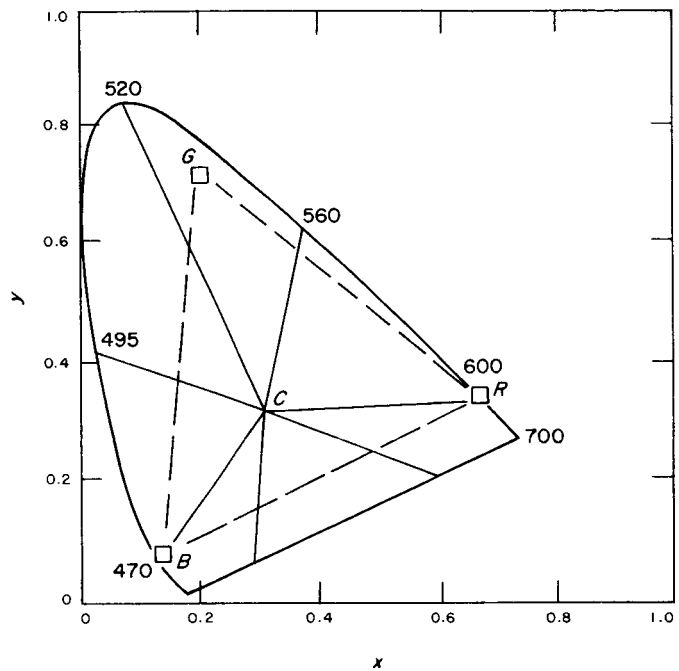


Fig. 32. The NTSC color triangle in CIE coordinates

The lines connecting C with the perimeter represent the degree of saturation for any particular color. The closer the chromatic coordinates are to C the less intense is the saturation or the fainter is the hue. Colors of low saturation cannot be simulated unless all three primaries are present. Thus, although blue, for example, may not be observed as a distinctive shade, it is one of the three selected primaries that must be employed to produce a white contribution.

Because surfaces in nature tend to reflect a high proportion of the incident sunlight, planetary photography will naturally be concerned with colors of low saturation. The contribution of the white light to the hue thus becomes the predominating factor in spectral evaluations of planetary images taken from orbiting or fly-by space vehicles.

c. NTSC compatible color TV system. The problems that have arisen in television color broadcasting with compatibility and bandwidth compression are of particular interest for planetary photography. The need to generate black and white luminance signals when broadcasting in color has stressed the property of luminance in electronic color reproduction.

Insofar as planetary photography is accomplished by electronic processes, advantage may be taken of the techniques that have been developed for color TV. A constant-

luminance, trichromatic system is specified for TV color broadcasting by the National Television Systems Committee (NTSC). The video spectrum is divided into three channels of decreasing bandwidth that carry monochromatic, trichromatic, and bichromatic information. The final image is presented on a tricolor dot-mosaic picture tube. For the purposes of planetary photography, a chemical dye process must be added to produce the final color photograph.

NTSC defines three primaries in CIE coordinates as red $x = 0.67$, $y = 0.33$; green $x = 0.21$, $y = 0.71$; and blue $x = 0.14$, $y = 0.08$. From these three primaries, a luminance signal is specified $E_Y = 0.30E_R + 0.59E_G + 0.11E_B$. The assumption is made that when reproducing standard illumination source C, $E_Y = E_R = E_G = E_B$.

The NTSC primaries, as defined above, may be inserted into the CIE diagram to form a color triangle, as depicted in Fig. 32. The NTSC system reproduces all colors that are contained within the triangle. The color reproduction so obtained claims a wider chromatic range than the better commercial printing processes.

If the output signals from a color camera, i.e., three camera tubes having suitable color filters, is proportioned as indicated for E_Y , the signal may be reproduced monochromatically. When appropriate gamma corrections are made to linearize system parameters the photometric functions, as opposed to chroma values, that are observed by the camera will be correctly evaluated. In this way the equation for E_Y forms the basis of a compatible television system where the output from a color camera can be reproduced as a monochromatic picture on a black-and-white picture tube. This is illustrated in the simplified diagram of Fig. 33. The reverse process is also true where a monochrome camera produces a monochromatic picture on a tricolor picture tube.

d. Data reduction. A further interesting property of electronic color reproduction uncovered by NTSC re-

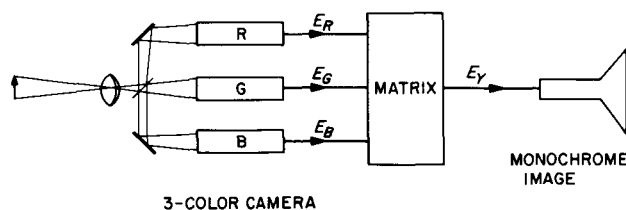


Fig. 33. Monochrome reproduction from three-color stimulus

search is that chromatic information can be inserted at greatly reduced resolution and that fine detail need be carried on a monochrome basis only. This is based on the property of the eye which has a limited resolution for chromatic detail. Thus, NTSC specifies a maximum video frequency of 4.2 Mc for monochrome information, while the trichromatic and bichromatic signals are limited to 1.3 Mc and 400 kc, respectively. The NTSC findings indicate that the data requirement for interplanetary color photography need not greatly exceed the monochrome requirement.

The NTSC chromatic information is transmitted as two additional signals designated I and Q . These are derived from the red-green-blue primaries

$$I = 0.59R - 0.27G - 0.32B \text{ and}$$

$$Q = 0.21R - 0.52G + 0.31B$$

At the receiver, by appropriate matrixing, three primary color signals R , G , B are derived from the Y and I , Q signals:

$$R = 0.96I + Y + 0.62Q$$

$$G = -0.27I + Y - 0.65Q$$

$$B = -1.11I + Y + 1.70Q$$

These represent three signals that are applied to the tricolor picture tube and form the basis of the compatible color and black and white reproduction.

Although there is no compatibility requirement for planetary photography, the ability to reproduce accurate monochrome information from only one of three sets of transmitted data could prove to be a valuable redundancy asset in space technology.

e. Camera filters. The spectral characteristics of the color filters required for the camera requires a conversion from the CIE diagram into the RGB color triangle. The filter characteristics so obtained are

$$R, G, B = \frac{\alpha_{1,2,3}}{\alpha_1 + \beta_1 + \gamma_1} \bar{x} + \frac{\beta_{1,2,3}}{\alpha_1 + \beta_1 + \gamma_1} \bar{y} + \frac{\gamma_{1,2,3}}{\alpha_1 + \beta_1 + \gamma_1} \bar{z}$$

\bar{x} , \bar{y} and \bar{z} are CIE tristimulus values, and α , β , γ are functions of the x , y coordinates of the primaries. Typical camera-taking characteristics are shown in Fig. 34.

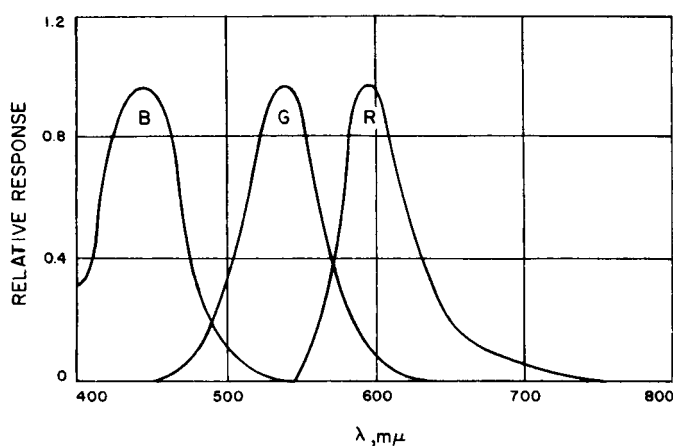


Fig. 34. Color filters employed in the NTSC camera system

Real-time transmission is not a requirement in exploratory planetary photography, and the chromaticity coordinates of each picture element, as derived from the transmitted camera signals, may be computer evaluated. This being the case, color signals may be sequentially generated instead of simultaneously generated as in broadcast TV. Thus, the need for three camera tubes is less apparent and depends more on the effective ground velocity of the planetary imaging device than on simultaneity.

f. Two-color system. When only two-color filters are employed with a single camera, as in the *Mariner*-Mars TV system, a need arises for the insertion of a third primary if any attempt is to be made to reproduce tonal values throughout the visible spectrum. Photography of Mars was accomplished with alternate green and red filters, with some degree of overlap in certain of the reproductions. In this case, a blue primary is required to permit presentation of a sufficiently wide range of tonal values at low saturation. One solution would be to include as part of the chromatic information direct observation from Earth. Although the direct observation is at lower resolution, as discussed above, high resolution is not necessarily a requirement for chromaticity insertion. A possibility thus arises of adding a synthetic blue primary in a quantity which will attempt to match tonal values with Earth observations.

g. Summary. Irrespective of apparent coloring, planetary color photography requires consideration of the entire visible spectrum. Because of compatibility and band-width compression, the NTSC system of color TV broadcasting is of particular interest. Components, such as the tricolor picture tube, may prove invaluable in the mechanization of ground systems.

2. Total Radiation Dose to Mariner IV Measured by the Ion Chamber Experiment

The ion chamber experiment was performed to measure the spatial and temporal variations of galactic cosmic rays and to observe trapped particles and solar cosmic rays when these were encountered. It was designed and built jointly at JPL and CIT by:

Principal investigator — Professor H. V. Neher, CIT

Coexperimenter — H. R. Anderson, JPL

Cognizant engineer — L. G. Despain, JPL

The instrument employs an integrating ion chamber and a single GM counter to measure the rate of ionization and the GM tube counting rate (average omnidirectional flux of penetrating charged particles) produced by all radiation behind 0.010 in. of steel. This shielding has a mass thickness of 0.2 g/cm², which is the range of 10 Mev protons. From the data provided by this instrument the total radiation experienced by the spacecraft was estimated.

The spacecraft is exposed to radiation of three types:

- (1) Galactic cosmic rays
- (2) Solar protons (from solar flares)
- (3) Trapped particles at Earth

The dose from these behind 0.2 g/cm² shielding in the first 230 days after launch is summarized in Table 8.

Table 8. Dose to Mariner IV in first 230 days of operation^a

Type of radiation	Total number of particles, omnidirectional particles/cm ²	Dose, r
Galactic cosmic rays	7.9×10^7	9.5
Solar protons	1.3×10^7	4.2
Trapped particles at Earth	1.4×10^6	10.1

^aBehind 0.2 g/cm² shielding.

Each category is now discussed in detail.

(1) The galactic cosmic rays consist of protons, alpha particles, and heavier nuclei, mostly with energies exceeding 200 Mev. Outside the Earth's atmosphere their flux is constant within 10% for the first 230 days of the mission. The ion chamber experiment measured

4 particles/cm² sec

1.7 mr, hr \simeq 1000 ion pairs/[sec cm³ of standard temperature and pressure (STP) air]

In 230 days this amounts to

$$7.9 \times 10^7 \text{ particles, cm}^2$$

$$9.5 \text{ r}$$

Fig. 35 shows 6-hr averages of these quantities for the first portion of the mission. Preliminary data were used, and we have not computed averages for all intervals.

Because the radiation is penetrating, these doses are uniform within 20% throughout the volume of the spacecraft. The average specific ionization (or LET) is about 5.5 Mev (g/cm²), i.e., about three times minimum ionizing. There are large local fluctuations about this figure due to nuclear stars produced in the material of the spacecraft.

As solar activity increases toward the maximum predicted in 1968-69, the flux and ionization rate of galactic cosmic rays will gradually decline by about a factor of 2.

(2) Almost all the solar protons encountered by *Mariner IV* through March 17 occurred in the two days following a solar flare at 1800 UT on February 5, 1965. Fig. 36 shows the ionization and counting rate measured by the ion chamber experiment during this event. The units in Fig. 36 may be converted as follows:

$$579 \frac{\text{ion pairs}}{\text{sec cm}^3 \text{ STP air}} = 1 \text{ mr/hr}$$

$$6.69 \text{ counts/sec} = 1 \text{ particle/cm}^2 \text{ sec}$$

The total dose from this event behind 0.2 g/cm² was

$$4.2 \text{ r}$$

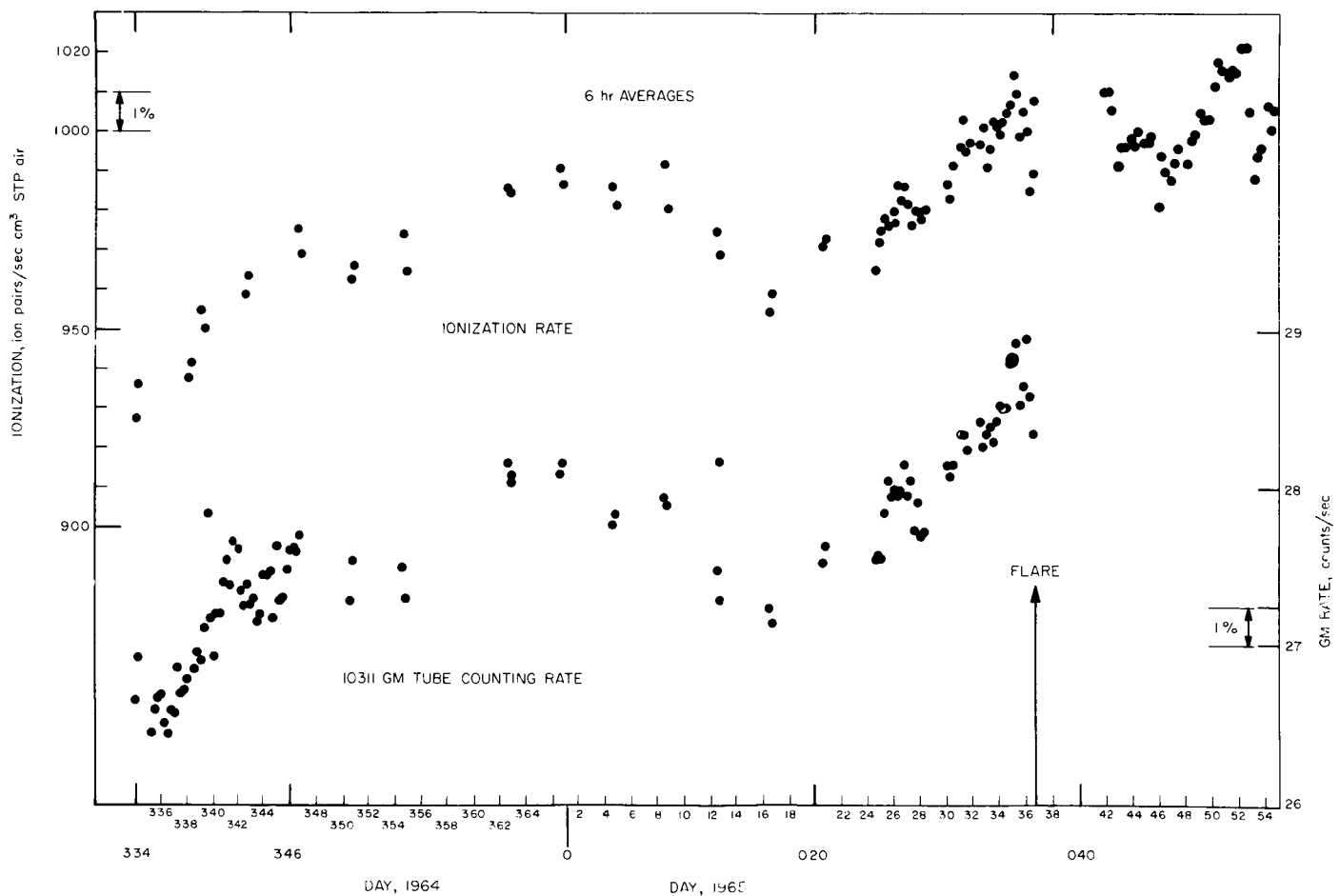


Fig. 35. Six-hour averages of ionization rate and GM tube counting rate measured by the ion chamber experiment on *Mariner IV*. Omnidirectional geometric factor of the GM tube is 6.69 cm²

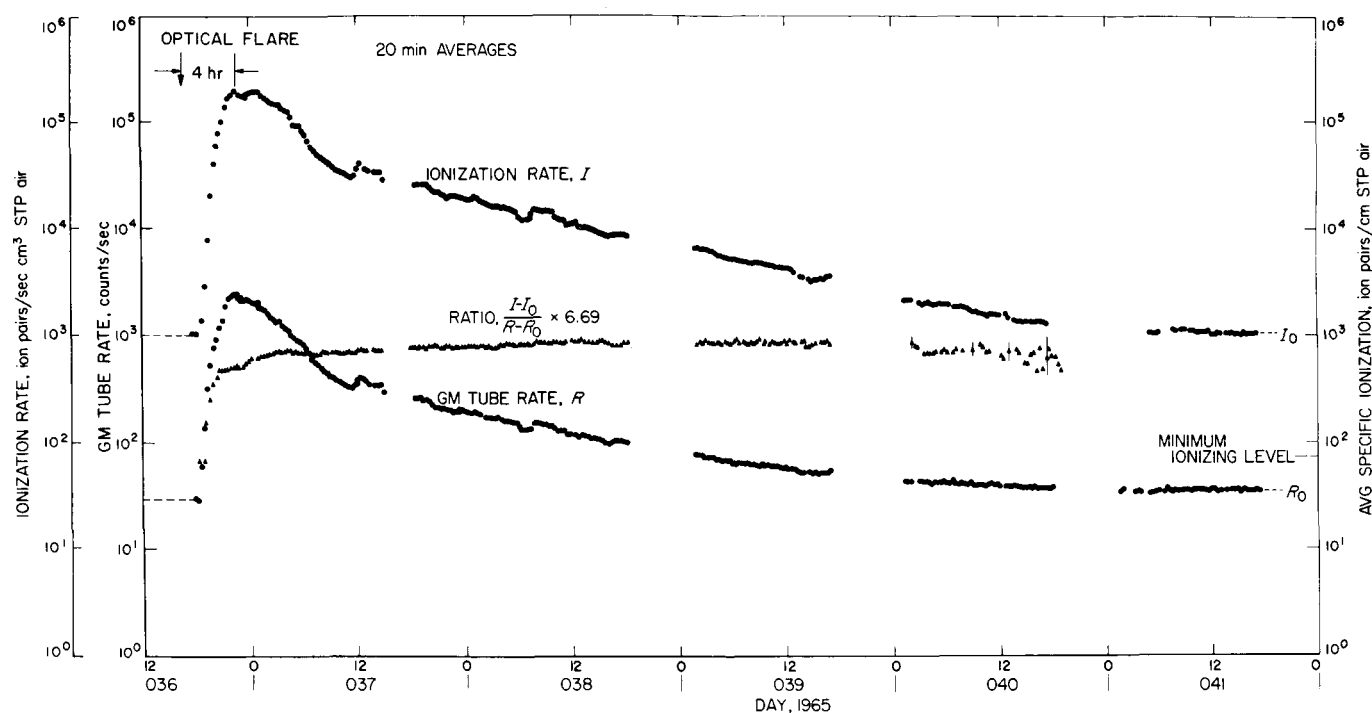


Fig. 36. Twenty-minute averages of ionization rate, true GM tube counting rate, and average specific ionization measured by Mariner IV following a Class 2 flare on February 5, day 036

and

$$1.3 \times 10^7 \text{ particles/cm}^2.$$

Unlike the galactic cosmic rays, the average energy of these particles (mostly protons according to data from the CRT) is 30–40 Mev. Other measurements made near Earth suggest that there are 3% as many particles above 80 Mev as there are above 10 Mev. That is, the integral energy spectrum in that energy range is approximately $4\pi j(>E) \propto 1/E^{1.6}$. Hence the dose diminished by a factor of ~ 30 in going from 0.2 to 7 g/cm² depth in the spacecraft. The number of protons with ranges between 0.001 and 0.2 g/cm² (0.5 to 10 Mev) was on the order of $10^8/\text{cm}^2$, judging from preliminary trapped radiation detector data reported by Van Allen et al. (AGU annual meeting, Washington, April 1965).

The ion chamber has not functioned since March 17, 1965. The other radiation detectors aboard have observed small fluxes of low energy protons and electrons on several occasions. No significant flux of solar particles with ranges exceeding 0.2 g/cm² was encountered between March 17 and the beginning of picture playback July 15.

(3) Fig. 37 shows the ionization rate and the GM tube counting rate measured by the ion chamber experiment in the Earth's Van Allen belts. The total dose measured behind 0.2 g/cm² shielding was

Inner belt (mostly protons of energy 10–100 Mev)	Outer belt (mostly electrons of $E > 1$ Mev)	Total
1.9 r	8.2 r	10.1 r
3.6×10^6 particles/cm ²	1.34×10^8 particles/cm ²	$1.38 \times 10^8/\text{cm}^2$

The particles trapped in the Earth's radiation belts are mostly of low energy. Thus, the numbers having ranges between 0.001 and 0.2 g/cm² was the order of 100 times greater than the numbers given, while the number of particles reaching 3 g/cm² or greater must have been the order of 100 times less. No trapped particles were observed in the vicinity of Mars.

In assessing the effects of radiation upon the spacecraft it must be remembered that by far the largest amount of energy absorbed by the surfaces facing the Sun is carried by

- (1) The solar photon flux
- (2) The solar wind consisting of 10^8 protons/cm² sec with an average energy of 1 kev.

Their energy is absorbed by the first few microns of the sunward surfaces.

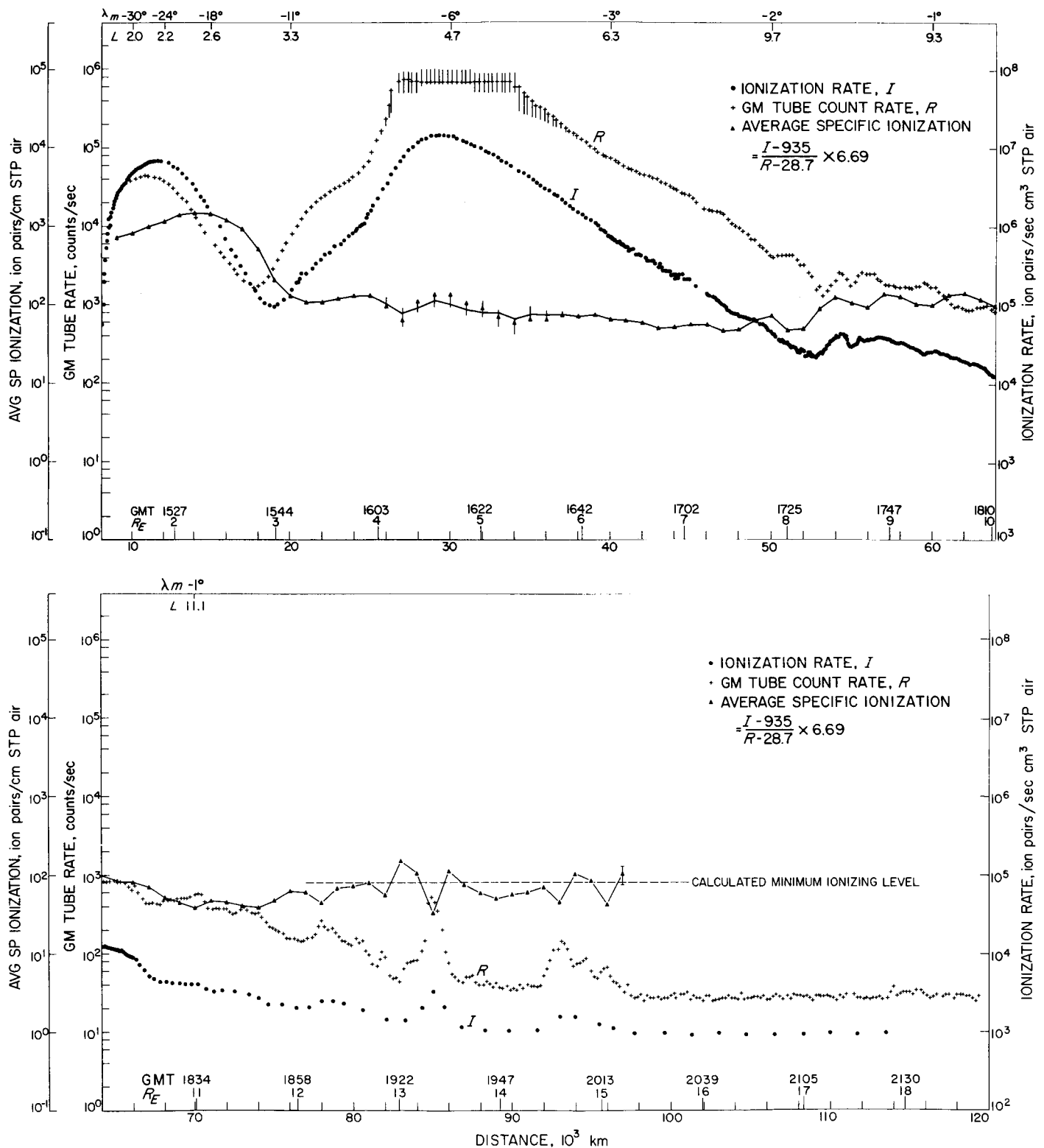


Fig. 37. Ionization rate, true GM tube counting rate and average specific ionization measured in the Earth's Van Allen belts by the ion chamber experiment on Mariner IV. Individual data points are shown. The uncertainty in R is not statistical but is caused by the GM tube being nearly saturated

3. *Mariner IV Magnetic Measurements Inside the Earth's Magnetosphere, Magnetic Tail, and Magnetosheath*

a. Introduction. The following is a report of preliminary scientific results based on analysis of the magnetometer data obtained as *Mariner IV* passed outward through the Earth's magnetosphere and crossed the transition region and the hydromagnetic bow shock. This material was excerpted from a longer paper presented at the Sixth International Space Science (COSPAR) Symposium held at Mar del Plata, Argentina in May of 1965 (Ref. 2).

b. The Low Field-Vector Helium Magnetometer. The *Mariner IV* magnetometer is a new instrument of a type that has not been flown on any other spacecraft. It was developed for use on missions that require a wide range of operating temperature, an extended dynamic range (a necessity if a substantial planetary field may be encountered), good absolute accuracy, and high sensitivity (a necessity to the study of interplanetary magnetic fields during the flight to the planet and to the search for small perturbations of the interplanetary field, if the planetary field is weak).

The *Mariner IV* instrument measures fields as large as 625γ ($\pm 360 \gamma$ referred to any of the three components, $1 \gamma = 10^{-5}$ gauss) with a limiting noise threshold equivalent to an rms field of 0.1γ . The instrument sensitivity (16.7 mv output for 1.0γ of applied field) is linear to within 0.1% over the full range. This is one aspect of the absolute accuracy which is insured by stability of both the linear characteristic and the null point (the output voltage in the absence of an ambient field) over both an extended temperature range (-25 to $+65^\circ\text{C}$) and long periods of time. High absolute accuracy is an important requirement for an instrument flown on an attitude-stabilized spacecraft, whereas on a spinning spacecraft, the spin permits an in-flight determination of the zero-field outputs of instruments, measuring field components transverse to the spin axis.

When the *Mariner* program was initiated, the above specifications equaled or exceeded those of the more conventional fluxgate or second harmonic type of magnetometer (such as was utilized on the *Mariner II* mission) (Ref. 3). Furthermore, the weight and power requirements of the two kinds of instruments were comparable and there was no reason to suppose that the stringent reliability requirements of the planetary mission could not be satisfied by the newer instrument.

The *Mariner IV* instrument is a low-field, vector, helium magnetometer not to be confused with either the rubidium magnetometer (Ref. 4) or the high-field, scalar, helium magnetometer (Ref. 5). Like the latter two it is a resonance magnetometer in which a specimen gas is examined spectroscopically using optical pumping to detect changes in state caused by the presence of weak magnetic fields. However, the vector helium magnetometer is not an absolute instrument like the others which produce tones, the frequencies of which are proportional to the field magnitude. Instead, it generates three steady or dc voltages each proportional to a component of the ambient field.

The basic operating principles of the *Mariner* instrument can be understood with the aid of Fig. 38. The pumping light, 1.08μ radiation obtained from an electrodeless discharge helium lamp, is circularly polarized and focused on an absorption cell where it is partially absorbed by metastable helium atoms. Absorption and pumping are observed by an infrared lead sulfide detector. Since simple Zeeman absorption depends on both the polarization of the resonant radiation and its direction of incidence with regard to the magnetic field, the pumped condition can be destroyed by changing the direction of the magnetic field. When a rotating field is applied to the cell, it causes a periodic variation in the transparency of the gas. A sweep oscillator produces two sinusoidal currents 90° out of phase in two mutually perpendicular sets of Helmholtz coils (represented in the figure by a circle) placed around the absorption cell. This generates a 100γ field rotating at a rate of 50 rps. Empirically it is found that the absorption is proportional to the square of the cosine of the angle between the light beam (optical axis) and the magnetic field. Thus, in the absence of an ambient field, the detector output is a second harmonic of the sweep frequency. If the dc field is present, the detector output contains a component at the sweep frequency whose phase depends on the angle between the optical axis of the sensor and the dc field. The ac amplifier passes a signal containing only the fundamental frequency component which is used to generate, by phase coherent detection, a dc current that is applied to the Helmholtz coils to null the external field. Thus, the magnetometer functions as a closed loop, or feedback system with a resulting improvement in output linearity and stability.

The simplified schematic shows the electronics for a two axis system. The triaxial *Mariner* instrument utilizes a time-sharing technique to switch the plane of the sweep vector on alternate rotations from the plane of the diagram to a plane perpendicular to the diagram through the

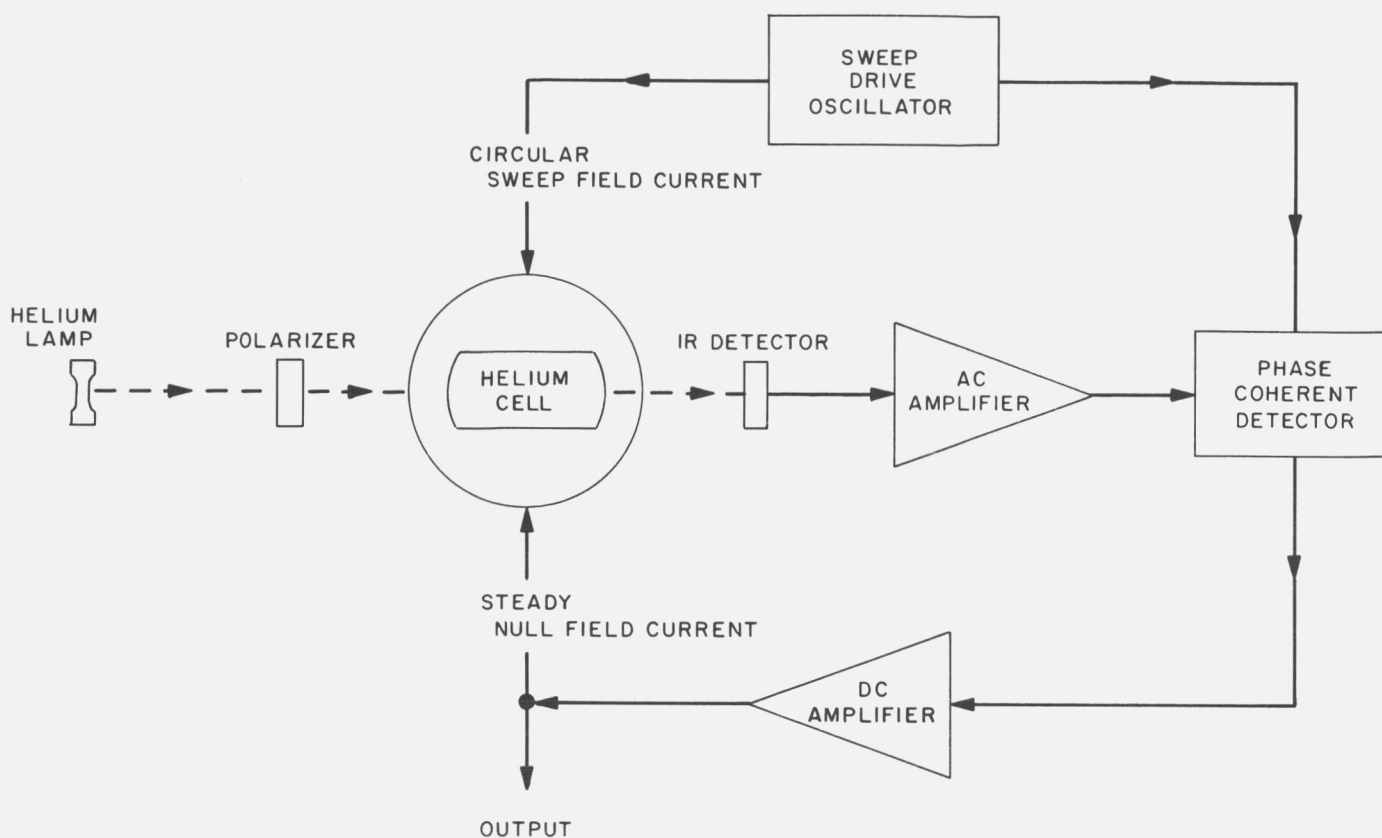


Fig. 38. Simplified schematic diagram of the *Mariner IV* magnetometer

optical axis. This commutation provides essentially simultaneous triaxial measurements when the outputs are sampled at the *Mariner IV* data rates.

A photograph of the *Mariner IV* magnetometer is shown in Fig. 39. The one-pound sensor is on the right. The triaxial helmholtz coils lie on a 4-in. diameter sphere with the helium lamp and igniter at one end and the detector and a preamplifier at the other. The two modules containing the rest of the electronics weigh 4.5 lb.

c. The Near-Earth data. Fig. 40 contains 10-min averages of the total field magnitude $|B|$ and the magnitude of the solar-radial component $|B_r|$, as a function of universal time (UT) or, alternatively, geocentric distance. During this time interval, which began shortly after the magnetometer came on scale and ended just prior to complete attitude stabilization, *Mariner IV* rotated slowly (~ 2 revolutions per hr) about an axis oriented toward the Sun. The changing orientation, relative to the ambient field, of the two sensor axes transverse to the Sun-oriented axis, allowed the corresponding components of the spacecraft field to be derived. The value of $|B_r|$ was adjusted to agree with the radial component of the unperturbed

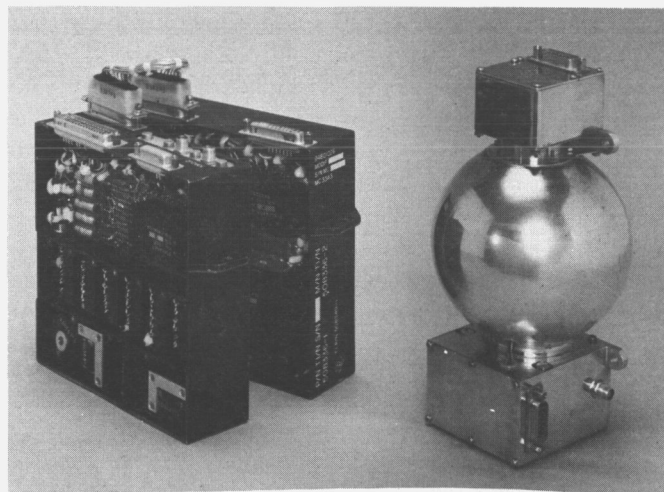


Fig. 39. The *Mariner IV* magnetometer. The sensor is shown on the right, and the electronics units are on the left

geomagnetic field near the Earth. The three spacecraft field components, which total 28γ at the sensor, were subtracted from the data before $|B|$ was computed.

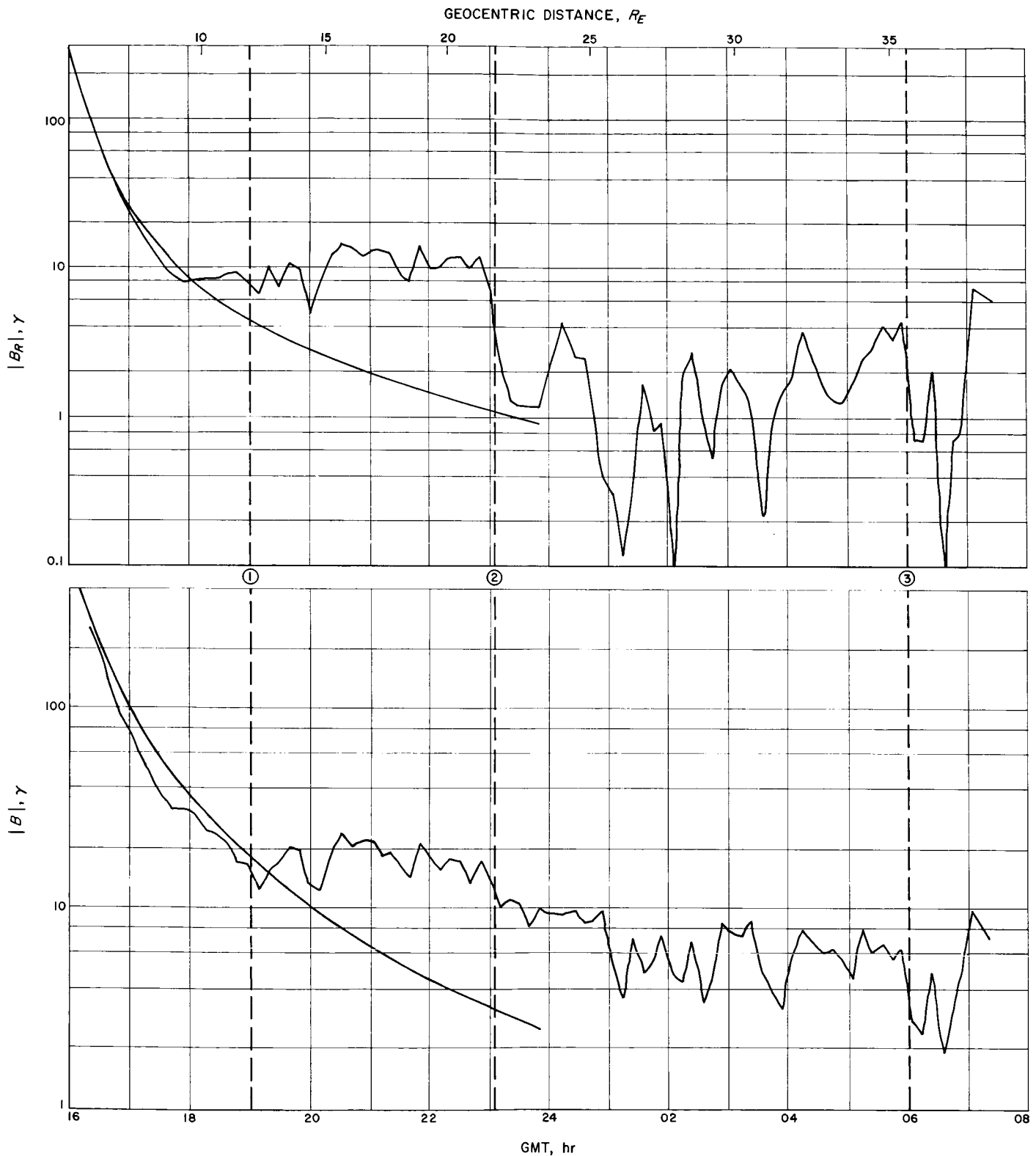


Fig. 40. Mariner IV magnetometer data acquired near Earth. Each datum is a 10-min average, centered on the time at which it is plotted. The dashed vertical lines labeled 1, 2, and 3 mark transitions separating the observed data into four different field regimes

The data show four distinctly different magnetic regimes separated by transitions designated simply as 1, 2, and 3. The data from nearest the Earth to the first transition (at $\sim 11 R_e$, Earth radii) show the same general dependence on geocentric distance as the unperturbed geomagnetic field. The average field from transition 1 to transition 2 ($\sim 21 R_e$) is essentially constant in magnitude with an enhanced radial component that points away from the Sun (no directional information is shown in the figure). The smaller ($5\text{--}10 \gamma$) average field in the region between transitions 2 and 3 is irregular in magnitude and direction. The third transition at $\sim 35 R_e$ is not completely obvious in the 10-min averages but marks the edge of a zone in which regions of rapidly fluctuating fields alternate with regions of relatively stable fields, as discussed below.

The locations of the three major transitions along the *Mariner* trajectory are shown in Fig. 41. This figure also contains a sketch showing the asymmetric magnetosphere, consisting of a torus formed by field lines that corotate with the Earth and an elongated magnetic tail pointing away from the Sun (Ref. 6), and the detached hydro-magnetic bow shock (Ref. 7). We identify transition 1 with the boundary between the corotating magnetosphere and the tail, transition 2 with the boundary between the tail and the turbulent magnetosheath, and transition 3 with the so-called standing shock front.

These boundary locations agree reasonably well with corresponding transitions in the *Mariner IV* plasma and energetic particle data as well as with previous field and particle measurements on other spacecraft. The dashed curves in Fig. 41 show the average location of the magnetopause and shock front derived from IMP-1 magnetometer data (Ref. 8). Transition 3 occurs near the extension of the outer contour. Transition 2 lies beyond the inner contour but is generally consistent with the spread in individual boundary penetrations by *Explorer 14* (Ref. 9), *IMP-1* (Ref. 8), and *Explorer 10* (Ref. 10) at approximately the same Sun-Earth-spacecraft angle. The innermost transition detected by the *Mariner* magnetometer appears to be associated with the general feature in the distribution of trapped electrons with energies greater than 40 keV. Omnidirectional flux contours obtained by *Explorer 14* instruments (Ref. 11) show a bifurcation behind the dawn line at an average geocentric distance of $\sim 9 R_e$ that is quite likely associated with the change from the magnetosphere proper to the magnetic tail. Detailed comparisons now in progress suggest that the large scale characteristics of the fields observed by *Mariner IV* in the different regions also agree with earlier measurements by *Explorers 10, 14*, and *IMP-1*.

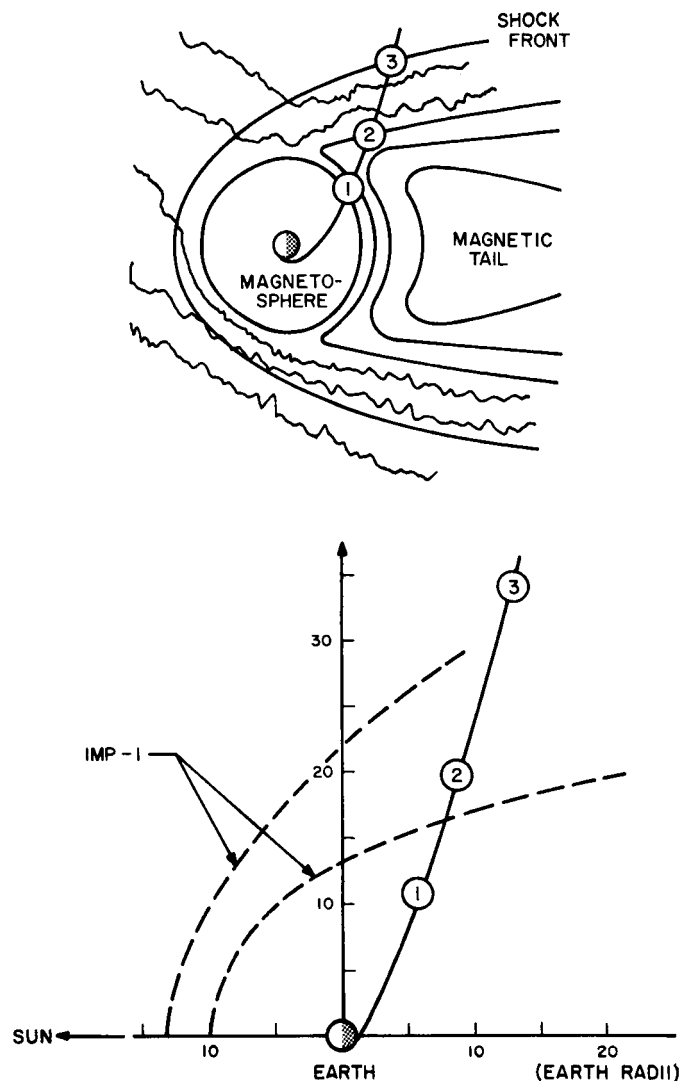


Fig. 41. *Mariner IV* near-earth trajectory. The bottom figure is essentially a polar plot of geocentric distance and the corresponding Sun-Earth-Mariner angle. Thus, this view of the trajectory is not a simple projection into a fixed plane such as the ecliptic. The circled numbers identify the positions, along the trajectory, of the 3 transitions shown in Fig. 40. The dashed IMP-1 contours indicate the average positions of the shock front and magnetopause. The schematic in the top figure relates the transitions observed by *Mariner* to the different regions of interaction between the solar wind and the magnetosphere

The data acquired beyond transition 3 merit special attention because the important features are associated with the fine structure of the field, which is obscured by averaging. Fig. 42 is a plot of all the magnetic measurements made during a one hour interval corresponding to

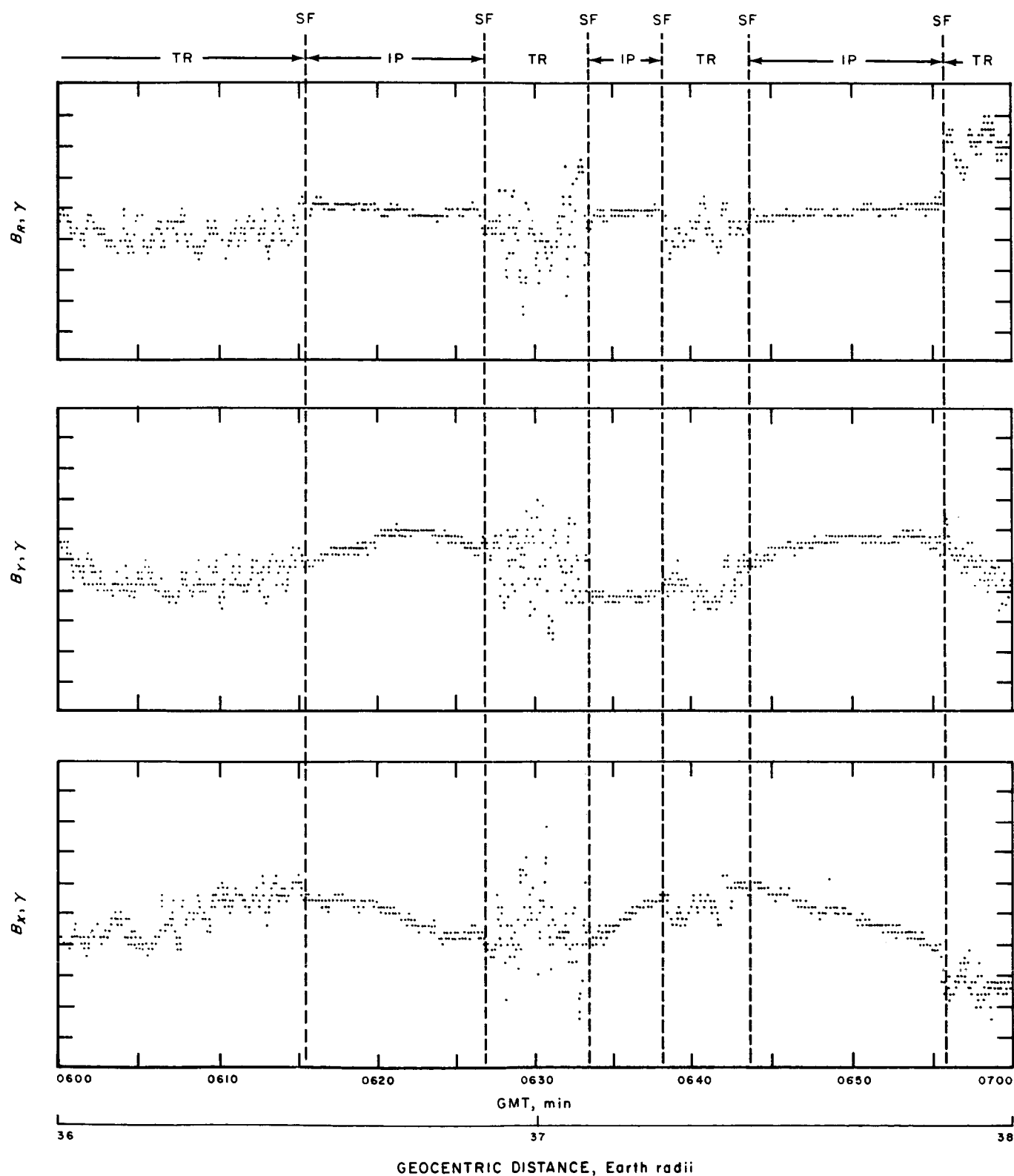


Fig. 42. Mariner data showing multiple passages of the shock front. Vertical lines corresponding to the instantaneous shock front (SF) position divide the data into intervals when Mariner was inside the transition region (TR) and outside the shock in the interplanetary (IP) medium

the range of geocentric distances between 36 to 38 R_E . No attempt was made to remove the effect of the spacecraft roll, which causes sinusoidal variations with periods of ~ 30 min in the transverse components B_x and B_y . The four triaxial measurements, each 12.6 sec, reveal regions of higher noise levels that alternate with regions of relative quiet. The last such observation came at 0718 and is not shown.

We identify the abrupt changes from the transition region to interplanetary space with successive passages through the shock front. This interpretation is supported by the *Mariner* plasma measurements which show penetrations into the free-streaming solar wind coincident with several of the shock front transitions in the magnetometer data (Ref. 12). The multiple passages through the shock front suggest that it is not stationary but surges back and forth over distances of several Earth radii with typical periods of 5 to 20 min, at least for this time and location. These results seem quite reasonable as it has been suggested that hydromagnetic shocks resemble hydraulic phenomena in which irregular and fluctuating fronts with considerable structure and precursors ahead of the main shock are typical. The sharp nature of most of the observed transitions suggests that the shock front makes a large angle with the trajectory and moves considerably, rather than that the trajectory lies nearly tangent to the front. Presumably it is the unknown velocity of motion of the front, not the known velocity of the spacecraft, that determines the apparent duration of the crossing from one region to the other. The average interval between suc-

cessive observations of the shock is comparable to the time required for the solar wind to slide around the magnetosphere, so it is not clear whether the local variations in the position of the front are caused by fine structure in the solar wind or by some form of instability.

The outstanding feature of the magnetic data is the occurrence of irregular fields behind the shock with or without an accompanying change in average field magnitude. The same feature was used to identify the *IMP-1* shock front locations (Ref. 8) and is also obvious in the *OGO-1* search coil magnetometer data (Ref. 13). The fluctuations are very roughly five times as great as outside. Preliminary inspection of tabulated data indicates that periods of 10 sec or more are prominent in the fluctuations in the transition region but that periods of 2 to 4 sec or shorter are much less important. Since the field must be convected with the solar wind velocity, the length scale of the irregularities should be of the order of $10^{2.5}$ km times the period in seconds. There is also a noticeable oscillation (not shown) with a period of 2 or 3 min (which corresponds to a length of the order of the radius of curvature of the magnetopause) and an amplitude of several gamma.

Acknowledgement. The efforts of many individuals on the *Mariner* project contributed to this experiment, in particular, J. Lawrence and D. Norris who served as cognizant engineers. The instrument was developed and fabricated at Texas Instruments, Inc., under the direction of F. N. Reilly.

References

1. Brunk, H. D., *An Introduction to Mathematical Statistics*, Chapter 11, Ginn and Company, 1960.
2. Coleman, P. J., Jr., Smith, E. J., Davis, L., Jr., and Jones, D. E., "Measurements of Magnetic Fields in the Vicinity of the Magnetosphere and in Interplanetary Space: Preliminary Results from *Mariner IV*," submitted for publication in the *Space Research*, VI.
3. Smith, E. J., Davis, L., Jr., Coleman, P. J., Jr., and Sonett, C. P., "Magnetic Measurements Near Venus," *J. Geophysical Research*, 70, 1571, 1965.
4. Ruddock, D. A., "Optically Pumped Rubidium Vapor Magnetometer for Space Experiments," *Space Research*, 2, 692, 1961.

References (Cont'd)

5. Keyser, A. R., Rice, J. A., and Schearer, D. L., "Metastable Helium Magnetometer for Observing Small Magnetic Fluctuations," *J. Geophysical Research* 66, 4163, 1961.
6. Axford, W. I., Petschek, H. E., and Siscoe, G. L., "Tail of the Magnetosphere," *J. Geophysical Research*, 70, 1231, 1965.
7. Spreiter, J. R., and Jones, W. P., "On the Effect of a Weak Interplanetary Magnetic Field," *J. Geophysical Research*, 68, 3555, 1963.
8. Ness, N. F., Searce, C. S., and Seek, J. B., "Initial Results of the IMP-1 Magnetic Field Experiment," *J. Geophysical Research*, 69, 3531, 1964.
9. Cahill, L., "Preliminary Results of the Magnetic Field Measurements in the Tail of Geomagnetic Cavity," *Transactions of the American Geophysical Union*, 45, 231, 1964.
10. Heppner, J. P., Ness, N. F., Skillman, T. L., and Searce, C. S., "Explorer X Magnetic Field Measurements," *J. Geophysical Research*, 68, 1, 1963.
11. Frank, L. A., Van Allen, J. A., and Macagno, E., "Charged Particle Observations in the Earth's Outer Magnetosphere," *J. Geophysical Research*, 68, 3543, 1963.
12. Snyder, C. W., Jet Propulsion Laboratory, Pasadena, California, Private Communications, 1965.
13. McLeod, M., Holzer, R. E., and Smith, E. J., "Preliminary OGO-1 Search Coil Magnetometer Results," in press, 1965.

II. *Voyager* Project

A. Introduction

The primary objective of the *Voyager* Project is the performance of unmanned experiments on the surface of, and in orbit about, the planet Mars in order to obtain information concerning the existence and nature of extraterrestrial life, the atmospheric and the surface characteristics of the planet, and the planetary environment. The secondary objective is the acquisition of scientific information concerning the interplanetary media.

All *Voyager* missions will be conducted as events of an integrated program in which each individual flight forms a part of a logical sequence in an over-all technical plan of both lander and orbital operations. The *Voyager* design will provide for the carrying of large scientific payloads to the planet, the telemetering of a high volume of data back to Earth, and long and useful lifetimes in orbit about the planet and/or on the planetary surface. Hardware will be designed to accommodate a variety of spacecraft and/or capsule science payloads, mission profiles, and trajectories. Particular emphasis will be given to simple design, feasible redundancy, and a comprehensive program of component, subsystem, and system testing.

Over-all direction and evaluation of the *Voyager* Program is the responsibility of the Office of Space Science and Applications (OSSA) of the National Aeronautics

and Space Administration (NASA). Management of the *Voyager* Project and implementation of selected systems is the responsibility of the Jet Propulsion Laboratory of the California Institute of Technology.

Two *Voyager* space vehicles are to be designed, constructed, and tested for launch during the 1971 Mars opportunity. Attention is also being given to requirements imposed on such vehicles by launches subsequent to 1971, such as missions planned for 1973 and 1975. The over-all flight spacecraft is to consist of a flight spacecraft and a flight capsule. The flight spacecraft, which will have a dry weight of approximately 2,000 lb and will carry several hundred pounds of scientific instruments, will be a fully attitude-stabilized device utilizing celestial references for the cruise phase and will be capable of providing velocity increments for midcourse trajectory correction and for Mars orbit attainment; onboard sequencing and logic will be provided, as will a ground command capability. The spacecraft will supply its own power from solar energy or from internal sources and will be capable of maintaining radio communications with Earth. In addition, the spacecraft will be thermally integrated and stabilized and will monitor various scientific phenomena near Mars and during transit, and telemeter this information back to Earth. It will also monitor and telemeter data pertaining to spacecraft operation. The flight spacecraft will also provide the flight capsule with services such as power,

timing and sequencing, telemetry, and command during the transit portion of the missions and may also serve as a communications relay. The flight capsule will be designed for entry into the Mars atmosphere, descent to the surface, impact survival, and surface lifetimes of as much as six months and will contain the power, guidance, control, communications, and data-handling systems necessary to complete its mission.

Appropriate deep-space flight tests of elements of the flight spacecraft are planned approximately two years earlier than the 1971 missions, and preferably in the 1969 Mars opportunity, in order to permit evaluation of *Voyager* components and subsystems during long life in space and to demonstrate operations procedures. The test program for the flight capsule, which includes Earth-entry flight tests, will investigate entry, descent, impact, communications technology, and sterilization. The launch vehicle for the 1971 and immediately subsequent *Voyager* operations will be the *Saturn 1B*, with a *Centaur* as the third stage. The 1969 test flights will use either the *Saturn 1B/Centaur* configuration or an *Atlas/Centaur* combination. The earlier Earth-entry test flights will probably be launched by an *Atlas*.

B. Propulsion

1. Liquid-Regulated Monopropellant Hydrazine System

Initial design studies which were conducted for the *Mariner* 1966 spacecraft pointed to the desirability of considering a postinjection propulsion system based on the technology and design of the advanced liquid propulsion system (ALPS) pressurization circuit. This circuit was designed to utilize the gases produced by the decomposition of hydrazine in a gas generator to accomplish propellant tank pressurization. The chief components of the generated gas pressurization circuit are a generant tank and bladder, a generant controller (liquid regulator), a generant valve, and a gas generator (SPS 37-32, Vol. IV, pp. 151-153). The unique features of this circuit are the storage of hydrazine and its pressurant in a common tank and the use of a liquid regulator to sense main propellant tank pressure and control flow to the gas generator.

Experimental tests have been made which integrated the necessary ALPS components with a *Ranger-Mariner*

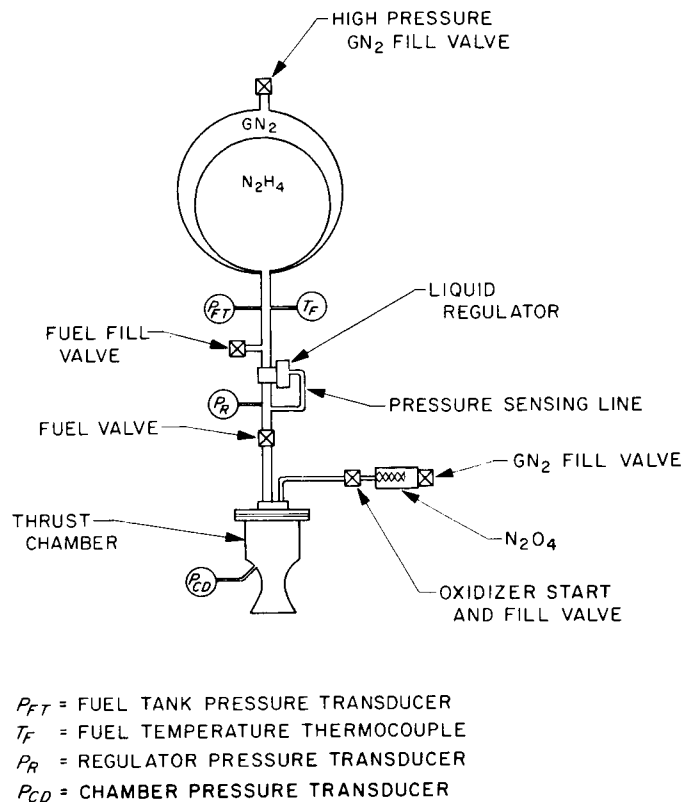


Fig. 1. Liquid-regulated system schematic

type monopropellant hydrazine engine. A schematic diagram of the prototype postinjection propulsion system is shown in Fig. 1. The system is functionally a liquid-regulated, pressure-fed, constant thrust rocket. Principle components are an ALPS propellant tank and balloon bladder (SPS 37-30, Vol. IV, p. 122), an ALPS liquid regulator (SPS 37-32, Vol. IV, pp. 157-160), a propellant valve, and a *Mariner-C* engine that employs an oxidizer start cartridge for hypergolic ignition.

A photograph of the assembled prototype system is shown in Fig. 2. The AISI 4130 heavyweight fuel tank has an inside diameter of 17.25 in. and a wall thickness of 0.218 in. The volume of the tank is 2711 in.³ The spherical bladder inside the tank contains a maximum volume of 1227 in.³ of hydrazine. This corresponds to 44.8 lb_m at 65°F. The initial nitrogen gas ullage volume is 1444 in.³ with a full load of fuel. The ullage volume is equal to the tank volume minus the volume of fuel and bladder material. The engine contains a quantity of JPL type H-7 catalyst. The nominal flow rate is 0.231 lb_m/sec with a corresponding nominal vacuum thrust of 53 lb_f. The oxidizer start cartridge contains 15 cc of nitrogen tetroxide (N₂O₄) for hypergolic ignition.

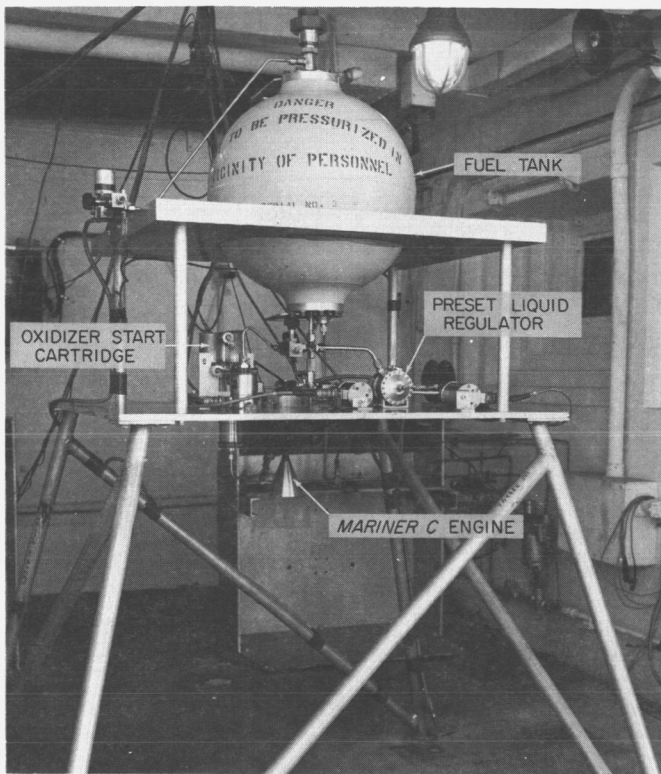


Fig. 2. Liquid-regulated system test configuration

Early tests were conducted with a *Mariner-C* engine which was filled with spontaneous catalyst.¹ This simplified the system still further by eliminating the need for the oxidizer start cartridge. During testing, however, the

¹Type 405, Shell Development Co., Emeryville, California.

engine chamber pressure was quite rough. Since it was felt that a separate development program was needed to solve the problem of rough combustion, it was decided to continue the system testing with the *Mariner-C* engine and oxidizer start cartridge.

A series of long duration firings (180 to 190 sec) were conducted with the system shown in Fig. 2 to determine the liquid regulator outlet pressure characteristics over a wide range of inlet pressures as well as the outlet pressure reproducibility between runs. The results are summarized in Table 1. During any single test, it was found that within the accuracy limitations of the instrumentation, no noticeable deviation occurred in the regulated outlet pressure value over the range of inlet pressures from about 1235 to 615 psia. In other words, $dp_{reg}/dt = 0$ for all the tests, with the exception, of course, of the start and stop transients. Reproducibility among tests was also quite satisfactory. However, only the tests which are grouped into pairs should be compared with each other since minor modifications and adjustments were made on the system between the groupings shown in Table 1. Tests 5 and 6 utilized explosive valves for the fuel and oxidizer to see if any unusual pressure disturbances would occur in the system because of the rapid opening and closing actions. No unusual disturbances were detected.

It should be mentioned that prior to running, the fuel valve is subjected to full tank pressure (~ 1215 psia) until flow occurs. During steady state flow, the fuel line downstream of the regulator is subjected to only regulated pressure (~ 345 psia). The reason that full tank pressure is seen at the fuel valve during the no-flow condition is that

Table 1. Liquid-regulated system test data

Test	Length of run, sec	Initial fuel tank pressure, psia P_{ti}	Final fuel tank pressure, psia P_{tf}	Regulated fuel pressure, psia P_{reg}	Chamber pressure, psia P_{cd}	Fuel temp °F T_f	System response time ^a , msec	Propellant valve type	Polytropic exponent ^b γ	Notes
1	73	1190	850	343	201	58	192	Solenoid	1.23	Test terminated early because of fuel line leak
2	190	1234	624	340	200	52	187	Solenoid	1.13	
3	186	1211	614	347	208	52	170	Solenoid	1.12	
4	180	1214	626	346	206	54	162	Solenoid	1.12	
5	180	1208	617	344	204	—	98	Explosive	1.13	
6	180	1219	617	343	204	64	90	Explosive	1.15	

^b γ is the experimental value of the polytropic exponent for the expansion process of the nitrogen gas in the fuel tank.
^aSystem response time is defined as the time interval between the electrical start signal to open the propellant valves and the time when the chamber pressure reaches 5% of the steady state value.

the regulator was not designed to lock up or form a leak-proof seal in the closed position. No extremely large pressure waves or spikes were detected in the fuel line as a result of this momentarily high pressure during start-up, although a pressure surge, typical of the *Mariner-C* engine during the starting transient, occurred in the fuel line between the fuel valve and injector.

No effort was made to reduce system response times by shortening line lengths nor was any effort made to reduce the system weights, since the main objective of the tests was to demonstrate the feasibility of a working model employing the liquid-regulator principle. Based upon this program, it is felt that a flight system could be designed and fabricated. The system would be simpler and inherently more reliable than the current *Mariner-C* propulsion unit since one set of valves and the nitrogen tank would be eliminated. Further, liquid regulation is considerably simpler than gas regulation; the range of upstream pressure variation is less, and the necessity of utilizing extremely close tolerances for the regulator seat is eliminated. Analyses have indicated that there is a slight weight disadvantage, however. If an injector development program were undertaken for the spontaneous catalyst, the necessity for an oxidizer start cartridge would be eliminated, and a multiple start system could be designed which would employ only one functional valve — a solenoid fuel valve.

C. Telecommunications

1. Low-Loss Spacecraft Coaxial Cable System

a. Introduction. Coaxial cable systems provide the important link between a spacecraft's radio subsystem and antenna. Therefore, they warrant a great deal of design consideration. In the past, spacecraft communication designs have been seriously handicapped by the limitations of existing cable designs and techniques. However, new developments are overcoming these handicaps.

The communications engineer must consider three major factors when designing a cable system for space-flight operations; i.e., high reliability, low electrical loss, and minimum total system weight. Cable systems which offer characteristics that approach these three major design requirements are limited to three basic cable types: flexible, semirigid, and rigid.

Flexible cable is very heavy and lossy at S-band frequencies compared to semirigid cable. However, flexible cable is more easily routed than semirigid cable. Easy routing, however, is not a sufficient reason for warranting its use on a spacecraft.

Rigid coaxial cables offer outstanding electrical characteristics but nothing else. They are very difficult to route and very heavy compared to flexible and semirigid cables. The electrical performance of rigid cable, per pound of weight, is not outstanding enough to incorporate its use in a spacecraft design.

It was concluded that semirigid cable offers the most outstanding overall performance per pound of weight. With this first application of semirigid coaxial cables to the *Mariner IV* program, many new problems arose. It was felt that a more detailed study should be undertaken to investigate further the capabilities of semirigid cables, and to develop a system consisting of semirigid cable and a new series of special RF connectors. The study was broken down into two phases: a semirigid cable study and a semirigid cable connector study.

The main objective of the cable study was to determine the cable's mechanical capabilities such as axial strength, endurance under shock, and weight potential that the cable will offer. The connector study is being carried out because of the serious shortcomings of the present state-of-the-art connectors for spacecraft use. Present connectors are quite bulky and extremely heavy for the type of electrical performance that they offer. The method of attaching these connectors on semirigid cables deforms, galls, and literally destroys the cable ends. However, the most undesirable malfunction is the loosening of the connector attachment under shock. Development of a new semirigid coaxial cable connector is, therefore, being undertaken with the following goals in mind: the connector should be as small as possible, it should be extremely lightweight (approximately 1.0 oz) and, most important of all, it should be sexless. The requirement of being sexless is a unique feature, since the connector program includes the development of a standard line of spacecraft transmission line components which do not restrict their use because of the gender of their connectors.

b. Cabling problem. Cabling systems, such as would be required on a *Voyager* type spacecraft, must make very long runs (approximately 10 ft of cable) between the radio subsystem and antennas. Therefore, the system undergoes a great deal of stress during the craft's launch period. This is the reason why the coaxial cable study's main objective is to determine and predict the limiting

mechanical characteristics which alter the loss parameters and reliability of semirigid coaxial cable. Two mechanical evaluations have been made to date: a static axial strength evaluation, and a weight evaluation. The results of these tests have been tabulated in Table 2. With the knowledge of these initial mechanical conditions, it was possible to make calculated predictions of the cable's mechanical behavior after being subjected to a chemical milling process.

Table 2. Mechanical characteristics of spiroline cable

Outer conductor 1080 aluminum	Permanent strain point	576 lb
0.530 in. OD 0.456 in. ID	Yield strength	708 lb
Inner conductor Copper tubing	Weight per foot	0.1555 lb
0.165 in. OD 0.125 in. ID		
Dielectric Teflon tubes		

The main objective for chemically milling the cable is to reduce its weight. True, this cable is lighter in weight than flexible cables and rigid cables; however, its outer conductor is thicker than is really necessary. Commercially purchased special cable predrawn with a reduced outer conductor thickness solves the weight problem, but it also introduces a new problem. When the outer conductor thickness is small, it is very difficult to bend the cable without fracturing it; therefore, all cable is bent before it is subjected to the chemical milling process, allowing satisfactory-type bends to be made.

Analysis of weight and strength characteristics. Using the results in Table 2 as initial conditions, an analytical study was performed to determine the three major mechanical features of the cable. An expression was obtained for predicting the weight of the cable as a function of the outer conductor material removed. This expression has been plotted in Fig. 3. The maximum yield strength point was also determined as a function of the outer conductor material removed, and has also been plotted in Fig. 3, along with the permanent strain point. Knowledge of these three important mechanical factors, makes it possible to predict the mechanical performance of the cable system.

So that the analytical results could be physically compared, cable specimens were chemically milled and then mechanically evaluated. The maximum yield strength, permanent strain point and weight were measured. The

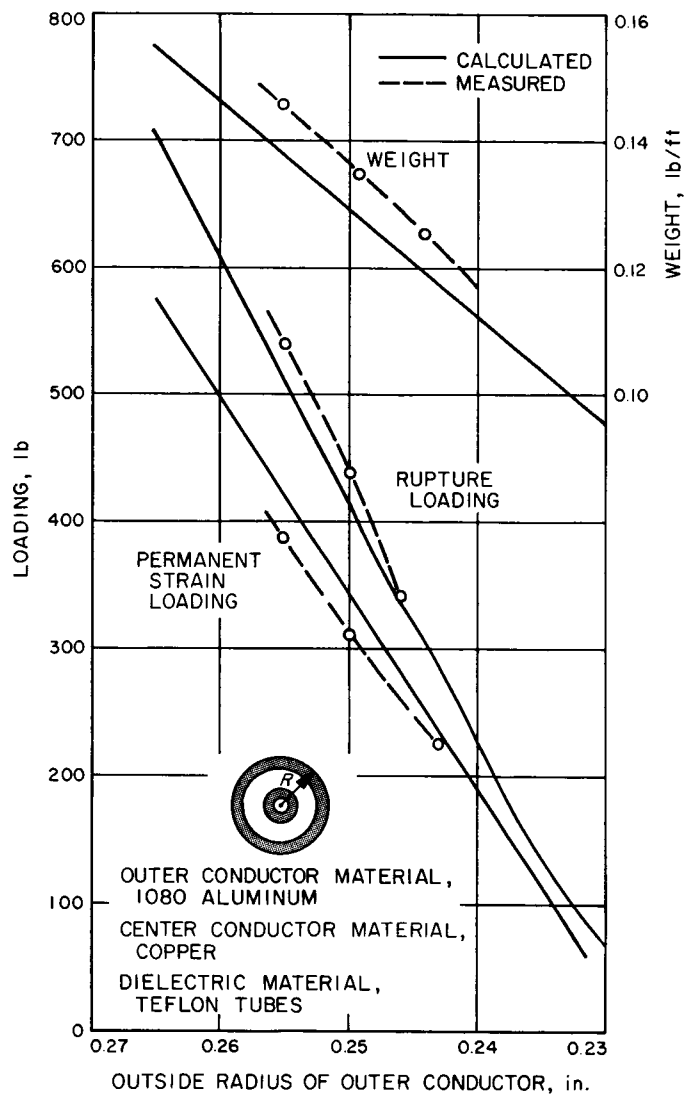


Fig. 3. Spiroline weight, rupture loading, and permanent strain loading as a function of the outside radius of the outside conductor

results of these tests have been plotted with the analytical results and are indicated by dashed lines in Fig. 3. It can be seen from these figures that the analytical results are well within a 10% accuracy of the physical results. This shows that the mechanical features of the cable can be mathematically predicted with fairly good accuracy.

Analysis of factors influencing the characteristic impedance. A second analytical study was performed to determine the cable's electrical characteristics as a function of mechanical tolerances and temperature (Ref. 1). Knowledge of the cable's electrical variations due to tolerance build-up and temperature change will make possible accurate cable specifications.

The relative change of the cable's characteristic impedance as a function of inner and outer conductor diameters was found to be

$$\frac{\Delta Z}{Z} = \frac{\frac{\Delta D}{D} - \frac{\Delta d}{d}}{\text{Log}_e 2.764}$$

where

ΔD = outer conductor diameter tolerance

Δd = inner conductor diameter tolerance

D = outer conductor diameter

d = inner conductor diameter

This function has been plotted in Fig. 4 for two different cases. In one case D is held constant. In the other case d is held constant. It can be seen from the figure that changes in the outer conductor diameter are less critical than changes in the inner conductor diameter. As an example to show how useful the information in Fig. 4 is, let us take the specifications of spiroline cable and determine its varying factors.

The manufacturer guarantees a characteristic impedance of $50 \pm 2\Omega$, which is a 4% change in the characteristic impedance. If the outer conductor tolerance is held constant, it is seen from Fig. 4 that the inner conductor diameter must be held within a tolerance of ± 0.007 in. If the inner conductor tolerance is held constant, the outer conductor tolerance may vary as much as ± 0.0185 in. These two values are the maximum boundary conditions that the conductors may have to maintain the $50 \pm 2\Omega$ impedance tolerance.

An analytical study was carried out to determine how critical the change in the cable's characteristic impedance is over various temperature ranges. The result of the calculation was

$$\frac{\Delta Z_r}{Z} = \left\{ 1 - \log_e \frac{[1 + (13.3 \times 10^{-6}) \Delta T]}{[1 + (9.2 \times 10^{-6}) \Delta T]} \right\}$$

where

ΔT = the deviation in temperature from 70°F .

The calculations were performed assuming that the relative dielectric constant of the cable did not vary with temperature. This is a reasonable assumption because teflon is a high temperature material. However, since

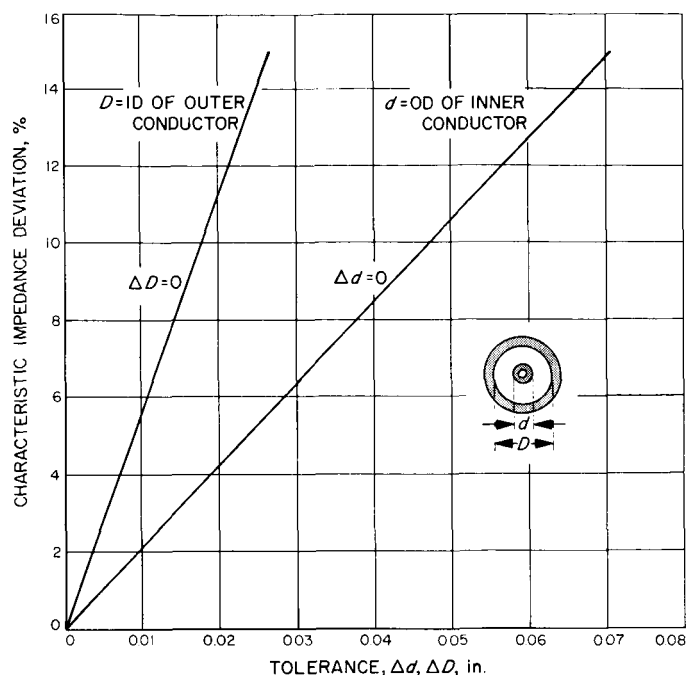


Fig. 4. Characteristic impedance of spiroline high-temp coaxial cable as a function of mechanical tolerances on the outer and inner conductors

the outer conductor and inner conductor are made of two different types of materials, aluminum and copper, respectively, each of the two metals has different expansion coefficients. Therefore, the ratio of the outer and inner conductor diameters will vary as a function of temperature.

The above function has been plotted in Fig. 5, and it can be seen that the relative change in the characteristic

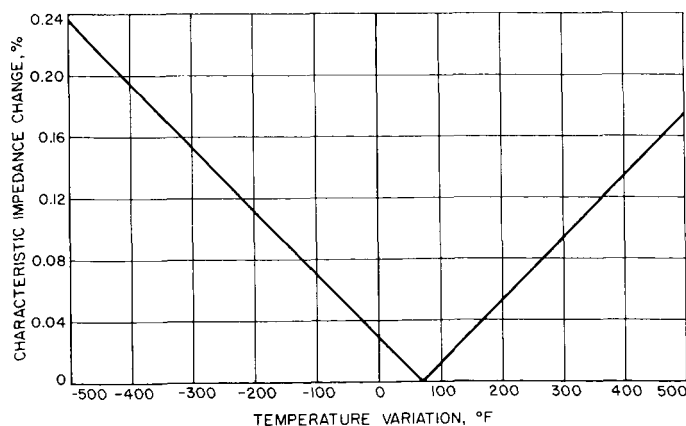


Fig. 5. Percentage change in characteristic impedance of spiroline cable due to temperature variations

impedance is very small. Therefore, electrical changes due to temperature variations are a very minute consideration in the cable study.

c. Connector design problem. Connector attachment to semirigid coaxial cable is a difficult problem. In the present commercially available connectors, a skive ring method is employed for attaching the connector to the cable. Fig. 6 illustrates a typical semirigid coaxial cable connector. It is bulky and heavy and also has a high voltage standing wave ratio and insertion loss. Its voltage standing wave ratio at S-band is approximately 1.2.

Fig. 6 shows the connector disassembled into its individual parts. The connector is made up of an N-type transition, into which the cable is inserted, and a skive ring, which is retained in a locking nut to serve as a gripping clamp. However, this skive ring has inherent weaknesses in its design. If it is necessary to assemble and disassemble the connector more than once, galling and deformation of the cable results. The skive ring's teeth

dig and bite into the cable and after many assemblings deforms the cable, changing its characteristic impedance. However, the most undesirable weakness of the skive ring connector is that it loosens from the cable under vibration. An attempt was made to solve this problem by glueing the skive ring with an epoxy. Upon cutting the glued specimens apart, it was discovered that only some rings were glued satisfactorily. In some cases, the epoxy actually prevented the skive ring's teeth from engaging the cable. It was determined that it is impossible to properly inspect and control the glueing process; therefore, a connector of this type, mounted in this manner, is unacceptable from a reliability standpoint.

The new connector design. The initial problem which had to be solved was a method for attaching the connector to the cable. The developed design utilizes a connector threaded onto the cable. Since the outer diameter of the outer conductor is a nominal 0.500 in., it was necessary to employ a 9/16 thread series, because a smaller thread would cut through the outer conductor. The 9/16 thread has a class three fit so that good concentricity is maintained between the connector and the cable.

A study was undertaken to determine which series of threads in the 9/16 class would yield the desired strength characteristics. Axial strength tests were performed on cable specimens with threads varying from 18 to 32 threads per inch. The threads were modified to offer maximum strength characteristics by "filling in" the V-groove with a 0.010-in. radius. The specimens were then submitted to an axial pull test until fracture occurred. All of the failures occurred in the final thread of the cable. The results of this test have been plotted in Fig. 7, and show the yield strength of the final thread as a function of the threads per inch.

It was observed during the test that the 32-threads-per-inch specimens began to strip instead of fracture; therefore, a series was selected which was less than 32 threads per inch. Before making the selection, however, it was necessary to evaluate what function the threads must serve. First, it was desired that the connector engage at least 3 threads, and, second, that the threads be shallow enough to offer an optimum axial yield strength. Since it was determined that a thread length of 3/16 in. would serve the purpose of the proposed connector design, a thread size of 9/16-24 UNEF-3 was selected.

The next design problem was to determine how to lock these threads so that they would not disengage under shock. This locking feature was accomplished with an epoxy resin. The connector shell overlaps the final thread

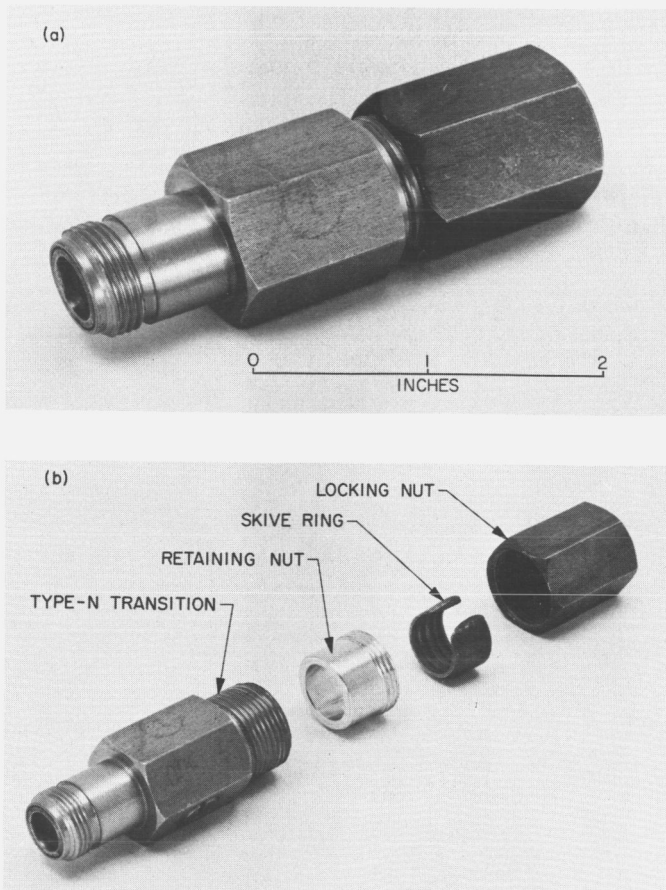


Fig. 6. Typical semirigid coaxial cable connector, assembled and disassembled

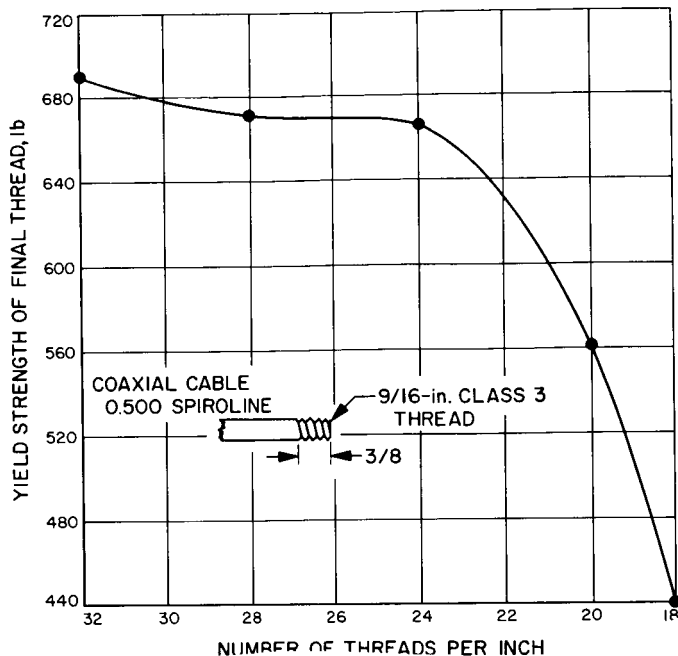


Fig. 7. Rupture of final thread as a function of the number of threads per inch

by 1/8 in., allowing an epoxy collar to build up between the cable and the connector. The function of this collar is to relieve the stresses encountered by the final thread, and also, to serve as a back-up attachment feature to the threads. If the threads should fail, the strength of the epoxy collar is such that connector-cable attachment will be maintained.

A definite epoxy type has not yet been selected for the connector design. However, for test purposes, Scotchweld EC-1614 was used. The selection of this epoxy was made on the basis that its characteristics were acceptable for the cable system of the *Mariner IV* spacecraft.

Since the cable system will go through a severe shock treatment, it is necessary that the epoxy be as flexible as possible in its set condition; for if the epoxy is brittle, its shock strength is decreased. EC-1614 has this flexible feature, and it was felt that a study should be made to determine its capabilities for use on future spacecrafts.

The study consisted of three separate phases. The first phase determined how sensitive the epoxy mixing procedure is to human error. This was the most important phase of the study, since the quality of an epoxy bond is not capable of inspection. The second phase of the study was a volatile condensable materials (VCM) test. This test determined how much contamination the epoxy offers

to surrounding spacecraft components. The third phase determined a strength and reliable bonding surface preparation. This phase of the study was conducted independently of the type of epoxy, since the test is a relative comparison of the surfaces.

The epoxy mixing test was conducted using the American Standard of Testing Materials procedure (ASTM Designation: D1002-53T) for testing epoxy shear strengths. The results of the test are shown in Fig. 8. This figure shows the shear stress of the epoxy in pounds per square inch as a function of percent errors in mixing with lines of constant temperature values. It can be seen, that at 75°F, the error in mixing is not very critical as far as the connector strength requirements go. However, as the temperature approaches 200°F and over, mixing of the epoxy becomes more and more critical. An error of about $\pm 15\%$ would be tolerable for temperatures up to 200°F. However, an analysis has yet to be made to determine the magnitude of the stresses the system will undergo at such high temperatures. If the stress magnitudes are low enough, it is possible that the allowable mixing tolerance will increase.

The results of the volatile condensable materials test were not very encouraging. These results have been tabulated in Table 3. The maximum acceptable VCM at 300°F, as set by the Materials Section, is 1.0×10^{-4} . It can be seen from Table 3 that EC-1614 is 25 times higher than the acceptable VCM value, which means it is quite volatile.

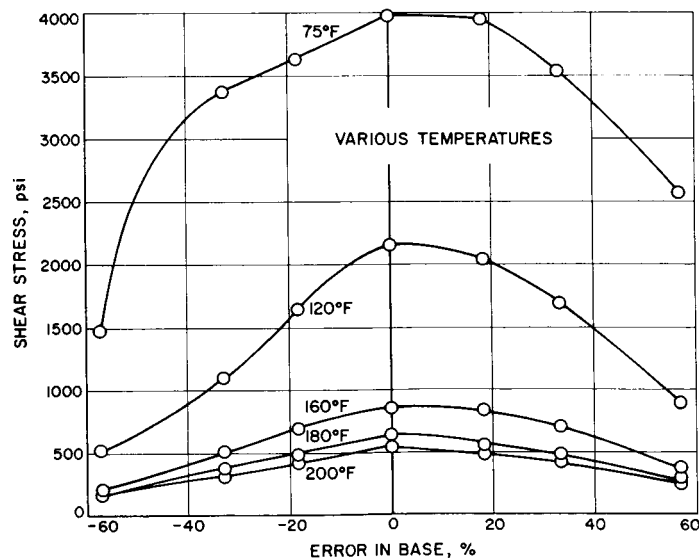


Fig. 8. Shear stress versus percent error in mixing for various temperature ranges of EC-1614 epoxy

Table 3. Volatile characteristics of EC-1614

Temperature, °F	Weight loss after test, %	Grams/in. ² of surface
200	0.5	0.0×10^{-4}
300	2.6	25.7×10^{-4}

It has been concluded that under a heat sterilization process, EC-1614 could contaminate surrounding spacecraft components. Therefore, a search for a different epoxy with the same mechanical characteristics as EC-1614 but with a very low VCM (less than or equal to 10^{-4}) will be made when systems testing begins.

The surface preparation tests yielded very interesting results. Two surface preparations were studied: one was a standard acid-edging preparation suggested by the Shell Chemical Company (Epon Adhesives Manual); the other was a 0.003-in. deep machine-finish. The test was performed with a 50% base and 50% accelerator epoxy mixture. All the specimens were cleaned with M-50 cleaning solution, and then placed in an ultrasonic cleaner to insure that every piece was thoroughly cleaned. A rigorous cleaning process was needed so that there would be no doubt that the small grooves of the machine-finished specimens were completely free from oil and dirt. The results of the test are given in Table 4.

Table 4. Gripping characteristics of epoxy

Mixing by parts		Temperature, °F	Shear strength	
Base, %	Accelerator, %		Etched, psi	Machine finish, psi
50	50	75	4200	4170
50	50	250	558	330
50	50	300	492	284

At room temperature, both surface preparations offered about the same adhesion, but when the temperature was elevated, the adhesion properties of the two surfaces differed remarkably. At 250 and 300°F the epoxy broke away from the machine-finished specimens, indicating a true shear had not taken place. It was first thought that the machine-finished surfaces would offer a better gripping area, but the results of the test showed that the machine-finish was inferior. Upon investigation of the machined specimens, it was observed that they had been properly cleaned, and also, that the epoxy had properly wetted into the grooves of the machine-finish. Therefore, improper cleaning was not responsible for the breaking away of the epoxy. Upon analyzing the problem further, it was strongly believed that milling an epoxy gripping surface was inferior because of the geometry involved.

Theoretically, a metal surface that has not been machined is essentially flat. Therefore, when a force is applied parallel to the metal plate surface, the plate is strictly in shear. However, when a V-groove machine-finish is put into the surface of the plate and a force is applied parallel to this surface, a single true shear is not obtained. This is realized by resolving the direction of the force into two components. One component is in the shear direction, and the other component is perpendicular to the shear direction. Epoxy resin has a very low tensile strength; therefore, it breaks away from the surface before a true shear strength value is obtained. From these test results, the acid-edging preparation was selected for the connector design.

With the knowledge obtained from all of the above preliminary tests, it was possible to begin the definition of various connector designs. To date, there have been four connector coupling designs proposed for evaluation. They are named for reference purposes: the flanged connector; the dog-leg connector; the four channel-track connector; and the threaded flanged connector. The major difference between all of the designs lies in the connector coupling techniques. The following is a brief description of the four different designs.

Fig. 9 shows the flanged connector fully assembled. It can be seen that the connector is relatively small. The maximum diameter, which is the diameter of the flanges, is 0.95 in. A coin has been placed in the picture to show the connector's relative size which is quite small compared to the present commercially available connector, as shown in Fig. 6. Fig. 9 shows the individual parts that make up the total connector: two inner shells, which are attached to the cable with threads and epoxy; two outer flanges, which secure a butt joint interface; a precision alignment ring, which aligns the concentricity of the butt joint; and four No. 0-80 screws and nuts, which draw the flanges together making a secure connection. At the interface of the connection, there is an air gap in the dielectric 0.060 in. in length. The dimension of this air gap has been analytically determined for matching the impedance of the connector interface to the impedance of the cable. A center conductor bullet, which aligns and connects the center conductors together, is not shown in the figure. It will be discussed later, since it is a major design problem in itself.

An assembly of the dog-leg connector is shown in Fig. 10. A scale has been placed in the figure to indicate the relative size of the connector. A three-section circular V-band with an adjusting screw is employed as the coupling mechanism. The adjusting screw opens and

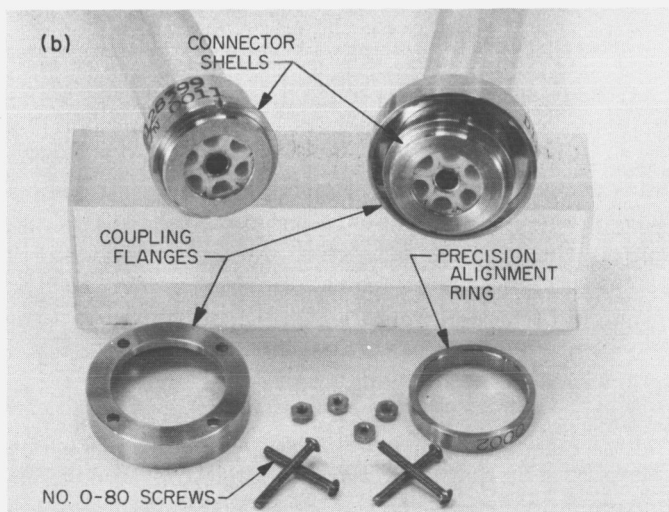
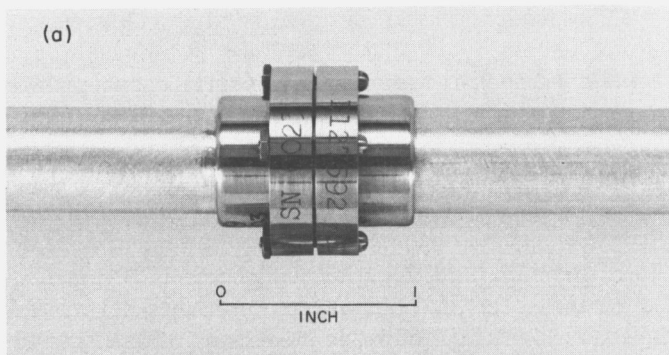


Fig. 9. Flanged connector, assembled and disassembled

closes the diameter of the V-band which in turn regulates the amount of axial pressure applied at the interface surface of the connector. Fig. 10 shows the connector disassembled. Like the flanged connector, the two inner shells are attached to the cable by threads and epoxy. Alignment of the total system is accomplished by a precision alignment ring, and secure interface coupling is accomplished with the V-band ring. The inner shells have raised surfaces angled at 20 deg; likewise, the V-band has three dog-legs with walls at an angle of 20 deg. As the V-band is drawn tighter onto the shell's ridges, the axial pressure at the connector interface is increased. Like the flanged connector, the interface air gap in the dielectric is 0.060 in. in length, and the dimensions of the gap have been calculated in order to make an impedance match between the connector and the cable. The V-band bolt has been made to swing out which makes assembling and disassembling a little easier, since the spring band around the three dog-legs is somewhat ridged. The band joining the three dog-legs is made of beryllium-copper, and the individual dog-legs are made

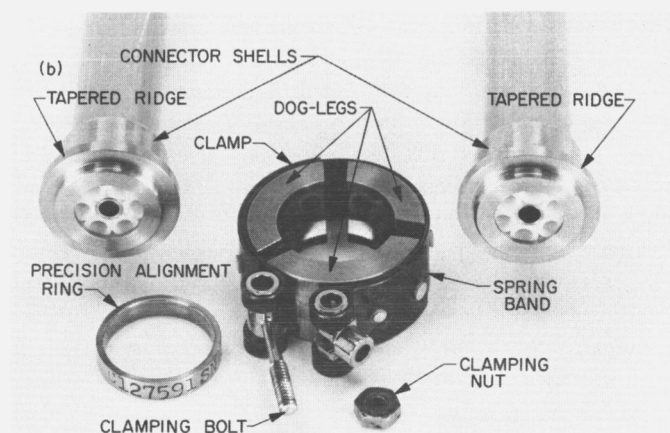
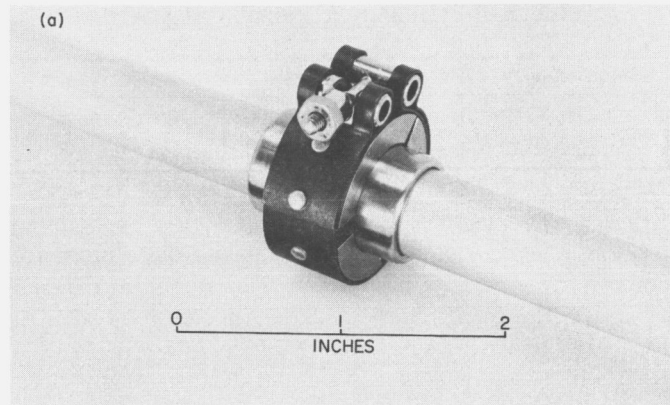


Fig. 10. Dog-leg connector, assembled and disassembled

of stainless steel. The use of these materials was necessary since it was desired that the connector should not be made from any type of magnetic materials.

The mechanical coupling of the four channel-track connector is very similar to the external coupling of a type-N connector (Fig. 11). However, the system as a whole remains sexless. It can be seen from the figure that the inner shells are threaded onto the cable and locked with an epoxy sealant. The interface butting surface, like the flanged connector, has an air gap 0.060 in. long. The dimensions of the air gap have been calculated to make possible a proper impedance match between the cable and the connector interface. Fig. 11 depicts more clearly the assembly pieces of the four channel-track connector. There are two identical inner shells which have four L-shaped channels diametrically opposite one another. The two outer shells, one with male threads, the other with female threads, each have four tracks that are also diametrically opposite. The connector is assembled by guiding the outer shell's tracks through the inner shell's

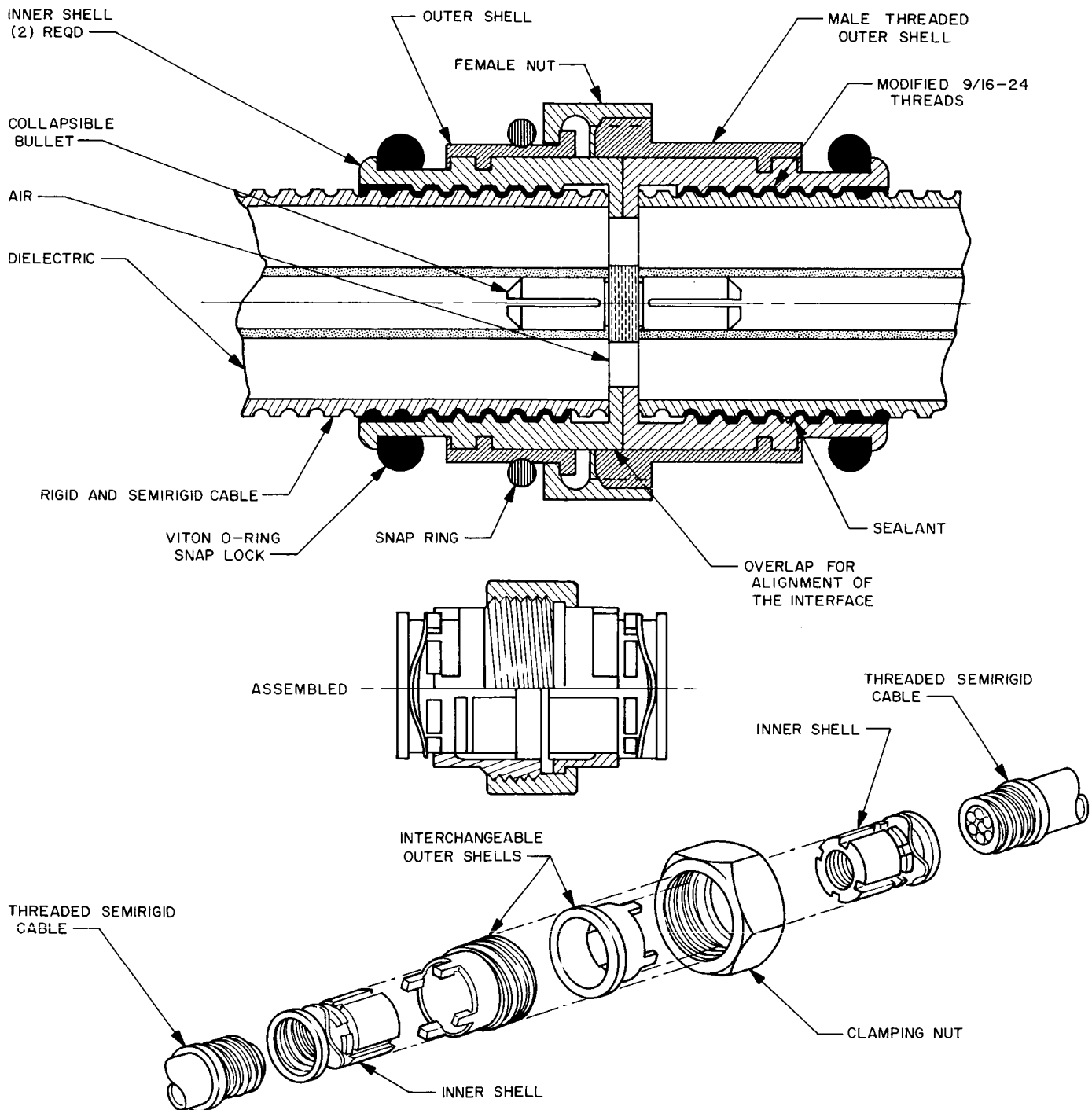


Fig. 11. Four-channel track connector, assembled and disassembled

channels, and then rotating them 45 deg. A Viton O-ring snaps the outer shell's tracks in place, locking the system. The male outer shell overlaps the connector's interface mating surface. Proper interface alignment is accomplished by this overlapping feature, which eliminates the precision alignment ring that is used in the flanged and dog-leg connector designs. The system is sexless in that the male and female outer shell positions can be interchanged at will.

The final design will have small grooves cut into the connector interface at each channel location. These grooves will serve as venting holes for trapped air. When the connector is completely assembled, air will be vented through the groove in the interface, through the unoccupied channel and out into space.

The threaded-flanged connector is basically the same as the flanged connector. The only difference lies in the coupling technique. Instead of using four screws and four nuts to join the flanges together, they are threaded, and captivated screws are engaged directly into the opposite flange, eliminating the four nuts.

All of the connector designs utilize a center conductor aligning bullet, which is a major design in itself. The design of the bullet will be such that it can be interchanged with any of the above four connector designs. Fig. 12 shows a layout diagram of the proposed bullet design. There are two alignment cylinders with a three-wave, collapsible beryllium-copper washer, retained by two retaining rings. The two alignment cylinders are $1\frac{1}{2}$ diameters in length to prevent any cocking-type action when the center conductors of the cable are misaligned. The cylinders also have four slots which divide each cylinder into four spring-type fingers which compress when placed into the center conductor. This insures a snug fit

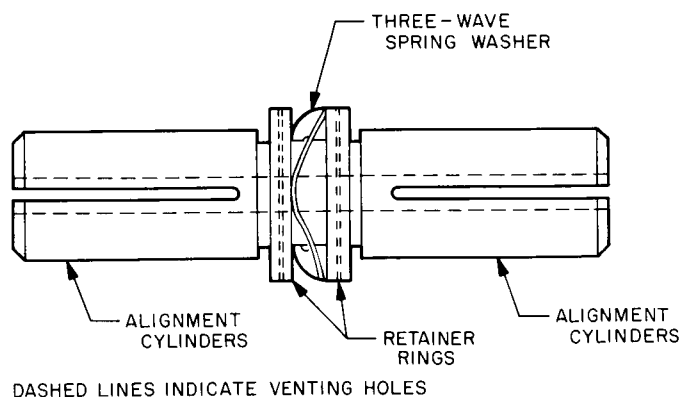


Fig. 12. Collapsible bullet design

to prevent rattling. The inner conductor of the cable butts against the retainer rings, which are free to move axially up and down on the center cylinder to allow the distance between the retaining rings to be varied as interface pressure is applied.

It is hoped that this type of bullet configuration will make proper center conductor butting possible by taking up any tolerance build-up in the connector's coupling innerface. If this type of bullet were not used, it is possible that the faces of the center conductors would not properly butt up against the bullet because of the shell tolerance build-up. Fig. 12 also indicates the proposed trapped air venting technique.

At the present time, none of the above connectors have gone through any type of sophisticated testing. However, rigorous type approval tests are being planned for evaluation. The results of the tests will be analyzed for outstanding features, and the connector design showing the most desirable characteristics will then be selected as a JPL standard spacecraft connector.

A method for evaluating the voltage standing wave ratio of a connector under static conditions was required and is shown in Fig. 13. The distance between the load and the slotted line remains constant throughout the test. However, with appropriate cable length combinations (L_1, L_2, \dots, L_6) the connector position was shifted down the line. The VSWR and phase shift for each cable set is measured and recorded on a Smith Chart. The locus of these measured points is a circle with a radius equal in magnitude to the VSWR of the connector under test. A more thorough treatment of this type of measuring technique can be found in Ref. 2. If the measurements are carried out with great care, it is possible to measure a VSWR as low as 1.01.

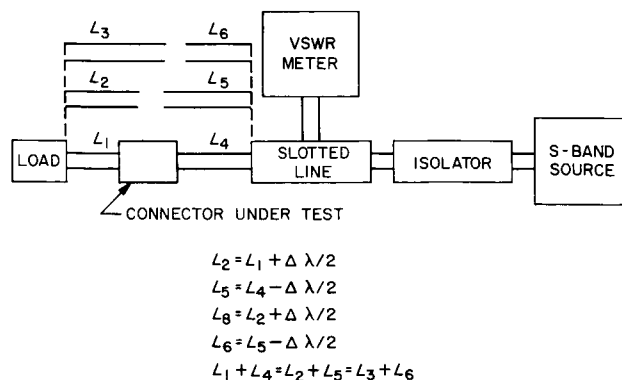


Fig. 13. VSWR test setup

At present the only connector submitted to this type of VSWR test has been the flanged connector. The results of the tests were quite desirable. The test showed that the connector had a maximum VSWR of 1.03 at 2116 Mc.

The flanged connector was also subjected to a static insertion loss measurement; however, it was felt that before the measurements were made, it would be worthwhile to make an analytical calculation to predict what the connector's insertion loss should be. Ignoring the mathematical details, it was determined that the connector's insertion loss could be expressed as:

$$\text{Insertion loss} = 8.686\alpha L$$

where

$$\alpha = \frac{R_T}{2Z_0}, \quad R_T = \frac{1}{2} \left(\frac{1}{a} \frac{(P_c f M_c)^{1/2}}{\pi} + \frac{1}{b} \frac{(P_{ss} f M_{ss})^{1/2}}{\pi} \right)$$

L = gap length

f = frequency

P_c = resistivity of copper

$$M_c = 4\pi \times 10^{-7}$$

P_{ss} = resistivity of stainless steel

$$M_{ss} = 4\pi \times 10^{-7}$$

a = inner conductor diameter

b = outer conductor diameter

The calculations were made with the following assumptions:

- (1) The connector shell interface is stainless steel.
- (2) The center conductor alignment bullet is beryllium-copper.
- (3) All conductance losses due to dielectric materials are negligible compared to the losses of beryllium-copper and stainless steel.

The above expression has been plotted in Fig. 14, and shows the insertion loss as a function of the connector's

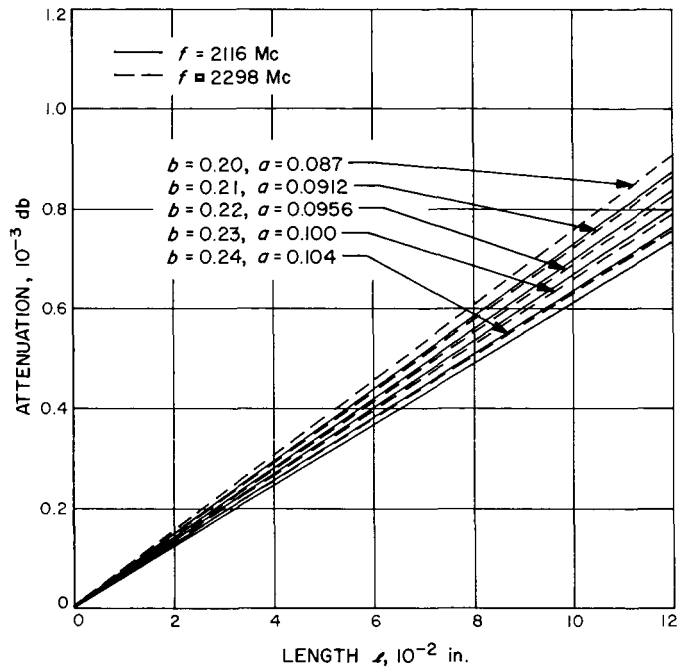


Fig. 14. Attenuation of a stainless steel butt joint as a function of the butting surface length

innerface length with constant lines of b and a . It is seen that the insertion loss of the flanged connector is practically negligible.

Insertion loss measurements were performed on the flanged connector to observe how the results would compare with the calculated predictions. The measurement accuracy of the insertion loss equipment is about 0.01 db. The insertion loss of the connectors was so small that it was lost in the measuring accuracy of the system. Therefore, it can only be concluded that the insertion loss of the flanged connector is less than 0.01 db at 2116 Mc. The results of the test confirmed the calculated predictions; that is, the insertion loss of the connector was so small that it is almost negligible.

The other three connector designs have not as yet been tested for VSWR and insertion loss. However, information on these connectors will be sought in the near future.

References

1. Neubauer, H., and Huber, F. R., *Coaxial Precision Connectors*, Reprint No. 65/1E from Rolde and Schwartz, Mitteilungen No. 19/1965, Druck: R. Oldenbourg, Graphische Betriebe GMBH, München 8, 1965.
2. Baker, L. R., "How To Determine Connector VSWR Precisely," *Microwaves*, September 1964.